EFFECTS OF ENGINE PLACEMENT AND MORPHING ON NONLINEAR AEROELASTIC BEHAVIOR OF FLYING WING AIRCRAFT

A Thesis
Presented to
The Academic Faculty

by

Pezhman Mardanpour

In Partial Fulfillment
of the Requirements for the Degree
Doctor of Philosophy in the
School of Aerospace Engineering

Georgia Institute of Technology
December 2013

EFFECTS OF ENGINE PLACEMENT AND MORPHING ON NONLINEAR AEROELASTIC BEHAVIOR OF FLYING WING AIRCRAFT

Approved by:

Professor Dewey H. Hodges, Advisor
School of Aerospace Engineering
Georgia Institute of Technology

Professor George Kardomateas
School of Aerospace Engineering
Georgia Institute of Technology

Professor Arash Yavari
School of Civil and Environmental Engineering
Georgia Institute of Technology

Dr. Fritz Kiessling
Former Head, Department of Aeroelastic Simulation
Institute of Aeroelasticity, DLR Göttingen

Professor Julian J. Rimoli
School of Aerospace Engineering
Georgia Institute of Technology

Date Approved: August 2013

To my wife Fatemeh,

To my parents,

Love you all

ACKNOWLEDGEMENTS

I express my deep appreciation to Prof. Dewey H. Hodges, my MS and PhD advisor. He has inspired me with methodology in research and teaching to the extent that I could not imagine or hope for a better academic advisor. His remarkable personal conduct and professional ethic will serve as a great example in my life.

I am specially in debt to thank Dr. Fritz Kiessling, my former MS co-advisor at the German Aerospace Center (DLR Göttingen) who introduced me to Prof. Hodges when I was at DLR. His friendship and patience were always there for me.

I would also like to thank Prof. J. Jagoda for his valuable suggestions about aircraft's engine problem. I am grateful to Prof. Oliver Bauchau for his fluent method of teaching in structural courses.

I would like to acknowledge the efforts of my thesis committee, Dr. Frtiz Kiessling, Prof. George Kardomateas, Prof. Arash Yavari and Prof. J. Rimoli in taking the time and reviewing my work.

I would like to thank my colleagues, Mr. Anurag Rajagopal, Mr. Seundo Heo, Mr. Ravi Kovali, Mr. Hanif Hosseini and Mr. Phillip Richards; all of whose company I enjoyed during these years.

I would like to thank my parents for their unconditional support throughout my life. And lastly but most importantly, I would like to thank my wife, Fatemeh, for without her dedication this work would have never been possible.

This work was sponsored by NASA Dryden, US Air Force Research Laboratory contract FA8650-06-D-3624/000708 through Bihrle Applied Research, Inc., and award ECCS-1101431 from the National Science Foundation.

August of 2013, Atlanta

Contents

List of Tables

List of Figures

Nomenclature

a	Deformed beam aerodynamic frame of reference
b	Undeformed beam cross-sectional frame of reference
B	Deformed beam cross-sectional frame of reference
$\mathbf{b}_i$	Unit vectors in undeformed beam cross-sectional frame of reference ($i = 1, 2, 3$)
$\mathbf{B}_i$	Unit vectors of deformed beam cross-sectional frame of reference ($i = 1, 2, 3$)
c	Chord
c_{m_β}	Pitch moment coefficient with respect to flap deflection (β)
c_{l_o}	Lift coefficient at zero angle of attack
c_{l_α}	Lift coefficient with respect to angle of attack (α)
c_{l_δ}	Lift coefficient with respect to flap deflection (β)
e_1	Column matrix $\lfloor 1 \;\; 0 \;\; 0 \rfloor^T$
EI_i	Bending stiffness for isotropic beam in i direction, ($i = 2, 3$)
e	Offset of aerodynamic center from the origin of frame of reference along $\mathbf{b}_2$
f	Column matrix of distributed applied force measures in $\mathbf{B}_i$ basis
F	Column matrix of internal force measures in $\mathbf{B}_i$ basis
$\mathbf{g}$	Gravitational vector in $\mathbf{B}_i$ basis
$\hat{\mathbf{g}}$	Unit vector in the direction of gravitational vector
GJ	Torsional stiffness for isotropic beam
h	Hypothetical hinge vector along each hinge
H	Column matrix of cross-sectional angular momentum measures in $\mathbf{B}_i$ basis
i	Inertial frame of reference
$\mathbf{i_i}$	Unit vectors for inertial frame of reference ($i = 1, 2, 3$)
I	Cross-sectional inertia matrix
k	Column matrix of undeformed beam initial curvature and twist measures in $\mathbf{b}_i$ basis
K	Column matrix of deformed beam curvature and twist measures in $\mathbf{B}_i$ basis
m	Column matrix of distributed applied moment measures in $\mathbf{B}_i$ basis
M	Column matrix of internal moment measures in $\mathbf{B}_i$ basis
P	Column matrix of cross-sectional linear momentum measures in $\mathbf{B}_i$ basis
r	Column matrix of position vector measures in $\mathbf{b}_i$ basis
R	3×3 partitions of the cross-sectional flexibility matrix
S	3×3 partitions of the cross-sectional flexibility matrix

T	3×3 partitions of the cross-sectional flexibility matrix
u	Column matrix of displacement vector measures in $\mathbf{b}_i$ basis
V	Column matrix of velocity measures in $\mathbf{B}_i$ basis
x_1	Axial coordinate of beam
β	Trailing edge flap angle
Δ	Identity matrix
γ	Column matrix of 1D "force strain" measures
θ_i	Fold angle at the i^{th} hinge ($i = 1,\ldots,$ number of hinges)
κ	Column matrix of elastic twist and curvature measures (1D "moment strain" measures)
λ_0	Induced flow velocity
μ	Mass per unit length
ϕ	Aircraft's bank angle
ξ	Column matrix of center of mass offset from the frame of reference origin in $\mathbf{b}_i$ basis
ψ	Polar angle for engine placement
Ω	Column matrix of cross-sectional angular velocity measures in $\mathbf{B}_i$ basis
$(\,)'$	Partial derivative of ( ) with respect to x_1
$\dot{(\,)}$	Partial derivative of ( ) with respect to time
$\hat{(\,)}$	Nodal variable

SUMMARY

Effects of engine placement on flutter characteristics of a very flexible high-aspect-ratio wing are investigated using the code NATASHA (Nonlinear Aeroelastic Trim And Stability of HALE Aircraft). The analysis was validated against published results for divergence and flutter of swept wings and found to be in excellent agreement with the experimental results of the classical wing of Goland. Moreover, modal frequencies and damping obtained for the Goland wing were found in excellent agreement with published results based on a new continuum-based unsteady aerodynamic formulation. Gravity for this class of wings plays an important role in flutter characteristics. In the absence of aerodynamic and gravitational forces and without an engine, the kinetic energy of the first two modes are calculated. Maximum and minimum flutter speed locations coincide with the area of minimum and maximum kinetic energy of the second bending and torsion modes. Time-dependent dynamic behavior of a turboshaft engine (JetCat SP5) is simulated with a transient engine model and the nonlinear aeroelastic response of the wing to the engine's time-dependent thrust and dynamic excitation is presented. Below the flutter speed, at the wing tip and behind the elastic axis, the impulse engine excitation leads to a stable limit cycle oscillation; and for the ramp kind of excitation, beyond the flutter speed, at 75% span, behind the elastic axis, it produces chaotic oscillation of the wing. Both the excitations above the flutter speed are stabilized, on the inboard portion of the wing.

Effects of engine placement and sweep on flutter characteristics of a backswept flying wing resembling the Horten IV are explored using NATASHA. This aircraft exhibits a non-oscillatory yawing instability, expected in aircraft with neither a vertical tail nor yaw control. More important, however, is the presence of a low frequency body-freedom flutter mode. The aircraft center of gravity was held fixed during the study, which allowed aircraft controls to trim similarly for each engine location, and minimized flutter speed variations along the inboard span. Maximum flutter speed occurred for engine placement just outboard of 60% span with engine center of gravity forward of the elastic axis. The body-freedom flutter mode was largely unaffected by the engine placement except for cases in which the engine is placed at the wing tip and near the elastic axis. In the absence of engines, aerodynamics, and gravity, a region of minimum kinetic energy density for the

first symmetric free-free bending mode is also near the 60% span. A possible relationship between the favorable flutter characteristics obtained by placing the engines at that point and the region of minimum kinetic energy is briefly explored.

Effects of multiple engine placement on a similar type of aircraft are studied. The results showed that multiple engine placement increases flutter speed particularly when the engines are placed in the outboard portion of the wing (60% to 70% span), forward of the elastic axis, while the lift to drag ratio is affected negligibly. The behavior of the sub- and supercritical eigenvalues is studied for two cases of engine placement. NATASHA captures a hump body-freedom flutter with low frequency for the clean wing case, which disappears as the engines are placed on the wings. In neither case is there any apparent coalescence between the unstable modes. NATASHA captures other non-oscillatory unstable roots with very small amplitude, apparently originating with flight dynamics. For the clean-wing case, in the absence of aerodynamic and gravitational forces, the regions of minimum kinetic energy density for the first and third bending modes are located around 60% span. For the second mode, this kinetic energy density has local minima around the 20% and 80% span. The regions of minimum kinetic energy of these modes are in agreement with calculations that show a noticeable increase in flutter speed at these regions if engines are placed forward of the elastic axis.

High Altitude, Long Endurance (HALE) aircraft can achieve sustained, uninterrupted flight time if they use solar power. Wing morphing of solar powered HALE aircraft can significantly increase solar energy absorbency. An example of the kind of morphing considered in this thesis requires the wings to fold so as to orient a solar panel to be hit more directly by the sun's rays at specific times of the day. In this study solar powered HALE flying wing aircraft are modeled with three beams with lockable hinge connections. Such aircraft are shown to be capable of morphing passively, following the sun by means of aerodynamic forces and engine thrusts. The analysis underlying NATASHA was extended to include the ability to simulate morphing of the aircraft into a "Z" configuration. Because of the "long endurance" feature of HALE aircraft, such morphing needs to be done without relying on actuators and at as near zero energy cost as possible. The emphasis of this study is to substantially demonstrate the processes required to passively morph a flying wing into a Z-shaped configuration and back again.

Chapter I

INTRODUCTION

1.1 Flying wing aircraft

A flying wing is a tailless fixed-wing aircraft with no definite fuselage, with most of the crew, payload and equipment being housed inside the main wing structure [23]. They may have various small protuberances such as pods, nacelles, blisters, booms, vertical stabilizers (tail fins), or undercarriage. Flying wings may achieve significant drag reduction due to a smooth outer surface. Consequently, the performance of such aircraft may increase significantly relative to conventional configurations of the same size. The flying wing configuration was studied extensively in the 1930s and 1940s, notably by Jack Northrop and Cheston L. Eshelman in the United States, and Alexander Lippisch and the Horten brothers in Germany [82]. They may exhibit body-freedom flutter when the short-period mode of the aircraft couples with the first symmetric elastic bending-torsion mode [20, 38, 51, 59, 7, 6, 69]. Due to the lack of vertical tail, a static flight dynamic instability, which involves the yawing motion of the aircraft in the horizontal plane, is usually captured in stability analyses and suppressed by control systems of the aircraft [20, 51, 57, 74, 59]. Although the lack of a vertical tail and instability of the kind mentioned above is rarely experienced in conventional aircraft [20], the potential increase of performance for this class of aircraft has inspired aeroelasticians to design a new generation of aircraft based on a flying wing configuration.

1.2 Aeroelasticity of flying wing aircraft

Aeroelasticity is the science that studies the interactions among inertial, elastic, and aerodynamic forces [12, 42, 21, 31]. It was defined by Arthur Roderick Collar in 1947 as "the study of the mutual interaction that takes place within the triangle of the inertial, elastic, and aerodynamic forces acting on structural members exposed to an airstream, and the influence of this study on design" [21]. Classical aerodynamic theories provide a prediction of aerodynamic forces for a given

shape, theories of elasticity provide a prediction of the shape of an elastic body under a given load and finally dynamics predicts the effect of inertial load on the body. Interaction of all three of them is called is called dynamic aeroelasticity [42]. Other terminologies are involved in the occurrence of the interaction of the two of them such as static aeroelasticity when there is no inertial load involved, flight dynamics when elastic deformation is not considered and structural dynamics when aerodynamic forces are not considered [12, 31]. Flexible high-aspect-ratio flying wings typically undergo large deflections and aeroelastic analysis of this class of aircraft requires geometrically nonlinear theories [63].

1.3 Engines and follower force

Follower forces are forces that will adjust their orientation so that it is always acting in the same direction relative to the geometry as shown in Fig. 1. Since the work done by this class of forces are path dependent, they are classified as non-conservative forces. As pointed out by Bolotin [14, 15], the study of the stability of structures under follower forces apparently started with work by Nikolai in late 1920s [70]. In order to ascertain whether systems subjected to follower force are stable requires a kinetic analysis of stability [70]. Engines of aircraft, rockets, and missiles behave similarly to follower forces and thus require a similar stability analysis as systems subjected to follower forces.

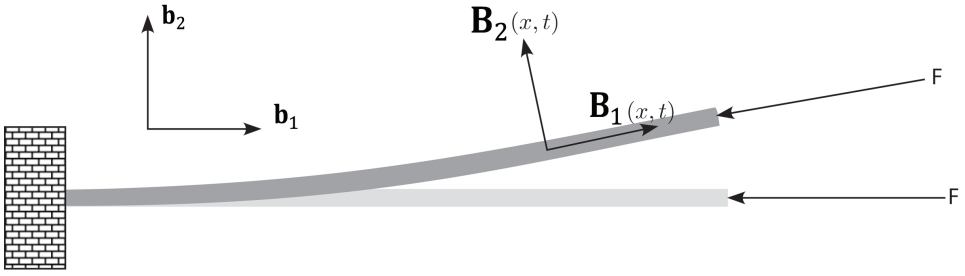

Figure 1: Schematic of beam undergoing compressive axial follower force

1.4 Morphing of flying wing aircraft

Morphing aircraft are multi-role aircraft that change their external shape substantially to adapt to a changing mission environment during flight [78, 76]. For example, a solar-powered morphing flying wing can maximize the energy absorption of solar panels on the wing surfaces by changing its

configuration such that the panels have highest exposure to the sun. This change in the geometry of the flying wing is highly effective in energy absorption during times just before sunset and just after sunrise, and consequently the aircraft can endure longer flight. The energy efficiency and aerodynamic performance of High Altitude Long Endurance (HALE) flying wing usually accompany each other. In addition, limitations on the weight of the aircraft and the sources of energy make the aeroelastic design very challenging. Use of solar energy is a novel method that eliminates one of the design constraints to a considerable extent by removing the limitation on the source of energy.

Chapter II

LITERATURE REVIEW

2.1 Aeroelastic analysis of flying wing aircraft

High-aspect-ratio flying wings may undergo large deflections, which leads to geometrically nonlinear behavior [63]. Previous studies by Hodges and Patil [63, 66, 64] showed the inaccuracy of linear aeroelastic analysis and the importance of nonlinear aeroelastic analysis. NATASHA (Nonlinear Aeroelastic Trim And Stability of HALE Aircraft) is a computer program [64, 19] used for this study. It is based on nonlinear composite beam theory [39] that accommodates the modeling of high-aspect-ratio wings. NATASHA uses the aerodynamic theory of Peters et al. [67] and assesses aeroelastic stability using the p method.

Previous comparisons by [73] showed that results from NATASHA are in excellent agreement with well-known beam stability solutions [77, 70], the flutter problem of [35], experimental data presented by [24], and results from well-established computer codes such as DYMORE [9, 10], and RCAS [68]. Sotoudeh, Hodges and Chang [73] presented additional parametric studies using NATASHA primarily for the purpose of validation. However, neither the effects of sweep nor of engine placement were included in these studies.

Present contribution in chapter 4 [1], uses the classical cantilever wing model of Goland [36] and compares the first four modes with results obtained from the continuum model of Balakrishnan [5]. In this approach the modal damping and frequency of those modes are compared, and excellent agreement is obtained for all modes, both stable and unstable, and both above and below the flutter speed. In section 4.2.2, the suitability of modeling sweep with NATASHA using the same Goland model is investigated. For the effect of sweep on divergence NATASHA's results are compared with an approximate closed-form formula presented in the book by Hodges and Pierce [43]. In case of flutter, results are compared with work done by Lottati [50], and in both cases results were in

[1] Based on a journal article accepted for publication by *Journal of Aircraft, [52].*

excellent agreement.

2.2 Effect of follower force in aeroelastic problem

Effects of follower forces on dynamic instability of beams were studied formerly [11, 13, 22, 81, 29]. Despite engine thrust being a follower force, few studies included this effect along with aeroelastic effects until the work of Hodges et al. [41] that presented a case in which the effects of thrust were maximized because the thrust vectors (from massless engines) were placed on the outboard portion of the wings of an aircraft with high aspect ratio. They concluded that increasing the thrust of the engines can have either a stabilizing or destabilizing effect and flutter speed and frequency were highly dependent on the ratio of bending stiffness and torsional stiffness of the wing. Fazelzadeh et al. [28] studied the effect of a follower force and mass arbitrarily placed along a long, straight, homogeneous wing. Their results emphasize the effect of follower forces along with the external mass magnitude and location on the flutter characteristics. Lottati [27], Karpouzian and Librescu [45], and Mazidi et al. [28] studied the effect of sweep on flutter boundaries, but none of them studied this effect using the geometrically exact equations for beams.

The dynamic response of cantilevered thin-walled beams carrying externally mounted stores and exposed to time-dependent external excitations was investigated by Na and Librescu [60]. They showed how the oscillation due to the external excitation can be suppressed by a control system. Young et al. [83] studied the dynamic response of a cantilevered beam subject to a random follower force at the tip of the beam using Gaussian white noise. Marzocca et al. [53], studied the effect of elasticity in the aeroelastic response of a two-dimensional lifting surface in incompressible flow subject to time-dependent external excitations and later he studied the aeroelastic response of a two-dimensional airfoil in a compressible flow field and exposed to blast loading [54]. Librescu et al. [48] investigated flutter suppression system of a two-dimensional wing excited by external pulses in incompressible flow by means of active flap control and in later works [49] they studied the dynamic aeroelastic response of a swept wing aircraft swept exposed to gust and explosive loads. Na et al. [61] studied the aeroelastic response of a composite beam exposed to explosive loading and gusts.

So far in the literature, many studies have shown that linear analysis are incapable to simulate

the response of the structure [62, 63, 66, 64, 65] and nonlinear analysis are required to comport with experimental evidence [62, 25]. Beams, in particular flexible high-aspect-ratio wings with gravity are statically nonlinear due to sufficiently large static deformation [25]. Patil, Hodges and Cesnik [65] studied the limit cycle oscillation in high-aspect-ratio wings but they neither consider the effect of gravity nor modeled the engine with mass, angular momentum. The effect of gravity is negligible for conventional wings, but for HALE wings it becomes important because it affects the trim solution in a non-neglible way. Consequently, with highly flexible wings such as those of HALE aircraft, one should expect load factor to have an influence on flutter, unlike the case of conventional aircraft. The present work in chapter 5 [2], studies the effects of engine placement on flutter characteristics of a very flexible high-aspect-ratio wing using the code NATASHA. This approach shows that gravity for this class of wings plays an important role in flutter characteristics. In the absence of aerodynamic and gravitational forces and without an engine, the kinetic energy of the first two modes are calculated. Maximum and minimum flutter speed locations coincide with the area of minimum and maximum kinetic energy of the second bending and torsion modes. Time-dependent dynamic behavior of a turboshaft engine (JetCat SP5) is simulated with a transient engine model and the nonlinear aeroelastic response of the wing to the engine's time-dependent thrust and dynamic excitation is presented. Below the flutter speed, at the wing tip and behind the elastic axis, the impulse engine excitation leads to a stable limit cycle oscillation; and for the ramp kind of excitation, beyond the flutter speed, at 75% span, behind the elastic axis, it produces chaotic oscillation in the wing. Both the excitations above the flutter speed are stabilized, on the inboard portion of the wing.

The present work in chapter 6 [3] studies the effect of two-engine placement on nonlinear aeroelastic trim and stability of a flying wing the geometry of which was similar to that of the Horten IV. The engines are modeled as a rigid body with a mass, an inertia matrix, a thrust vector, and a value of angular momentum. The result of this study shows that the maximum flutter speed occurs when the engines are just outboard of 60% span; also the minimum flutter speed occurs for engine placement at the wing tips. Both minima and maxima occurred when the c.g. of the engine was forward of

[2]Based on a journal article currently under review by *Journal of Nonlinear Dynamics.*
[3]Based on a journal article accepted for publication by *Journal of Aircraft[52].*

the wing elastic axis. In this approach, in the absence of aerodynamic and gravitational forces and before mounting the engines, NATASHA found that the minimum kinetic energy region is very near 60% span for the first symmetric elastic free-free bending mode. This location coincides with the region where the maximum flutter speed was observed.

In chapter 7 [4], the analysis is extended for the effect of multiple engine placement for flying wing configuration and the results show that engine placement does not have any significant effect on the lift to drag ratio. However, a noticeable increase in flutter speed is observed when engines are placed forward of the elastic axis. For these cases, as one of the engines is placed at the outboard portion of the span, flutter speed increases. For engine placement behind the elastic axis, flutter speed increases when both engines are close to the root. The area of minimum kinetic energy for the first and third bending modes is located approximately at 60% span. For the second bending mode, this area has local minima around 20% and 80% span. The areas of minimum kinetic energy for these modes are in agreement with flutter calculations, which show noticeable increases in flutter speed when engines are placed in these regions forward of the elastic axis.

2.3 Morphing of the aircraft

A morphing flying wing can maximize the energy absorption of solar panels on the wing surfaces by changing its configuration such that the panels have highest exposure to the sun. The morphing flying wing concept could be either based on wing morphing systems or airfoil morphing systems, or a combination of both [33]. So far in the literature, several morphing concepts and systems have been developed based on altering various geometric parameters of the wing (such as span, chord, camber, sweep, twist and even airfoil thickness distribution) to make the aircraft suitable for different missions and flight conditions [33, 37].

There are many examples in airfoil morphing, such as inflatable wings with new materials for roll control using nastic structures, bump flattening, or trailing-edge deflection [17, 71, 33]; hyper-elliptic wings with variable camber/span that use a quaternary-binary link configuration mechanism

[4] Based on journal article currently accepted for publication with minor revisions by *Journal of Fluids and Structures.*

for actuation [75, 33]; wing morphing similar to the folding wing concept of Lockheed Martin with efficient loiter and fast dash configurations [47, 72, 16, 51, 44]; the bat wing design of NextGen with high lift and efficient loiter configurations [30, 3, 34, 33]; and many other examples using smart structures and shape memory alloys [33]. In all these examples the weight of actuators and the actuation power that the morphing mechanisms require to perform their task are the problematic parts of the design [33], in particular when it comes to morphing of flying wing and/or HALE aircraft.

The folding wing configuration has been analyzed using linear aeroelastic models [80, 79, 26] and nonlinear aeroelastic models [4].So far in the literature neither a geometrically exact beam formulation has been used in morphing analysis nor a area of passive morphing has been touched.

In this study, in chapter 8 [5], a solar powered High Altitude, Long Endurance (HALE) flying wing aircraft is considered to morph into a "Z" configuration to allow for sustained uninterrupted flight. Energy absorption of this aircraft is maximized if the sun exposure of the solar panels distributed on the wings is maximized; see Fig. 2. For this purpose a three-wing HALE flying wing follows the sun and morphs passively (without actuators at the hinges and only making use of aerodynamic force and thrust) into a Z shaped configuration, while the bending moments about hinge lines at the beam connections are zero. To capture these phenomena, NATASHA has been augmented with new equations to analyze aeroelastic trim, stability and time marching of such aircraft. Local bending moments are zeroed out at the beam connection points while the hinges are locked and are kept at zero while the aircraft morphs. The morphing motion is brought to a stop before the hinges are again locked. The aim of this study is to detail the various processes pertaining to the passive morphing of a flying wing with Z configuration.

2.4 Motivations behind this study

The fully intrinsic nonlinear composite beam theory [39] presents exact and rigorous beam equations which accommodate large deflections. The importance of using nonlinear composite beam theory

[5] Based on a journal article currently accepted for publication with minor revisions by *Journal of Fluids and Structures.*

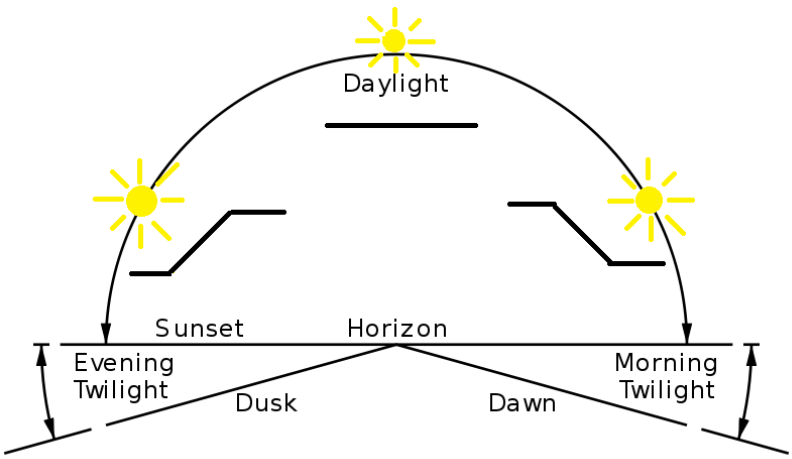

Figure 2: Schematic view of the flying wing morphing and the sun position

in aeroelastic analysis of high-aspect-ratio wings is accentuated in sections 1.2 and 2.1. Traditional aeroelastic analysis of high-aspect ratio wings do not consider effect of gravity and while this effect plays an important role in flutter characteristics. Effects of follower force on dynamic behavior of beam-like structure have been studied in former literature listed in section 2.2. However it is noteworthy that none of them considered this effect either using a geometrically exact nonlinear composite beam theory or for the flying wing configuration. One aspect of this research explores various effects of follower force on nonlinear aeroelastic behavior of the flying wing aircraft using the geometrically exact beam theory of Hodges [39] along with finite-state induced flow aerodynamic model of Peters et al. [67]. Section 2.3 reviews the former works on morphing aircraft. As of the up to date knowledge of the author, in all of the former morphing aircraft, actuators of different kinds were used to make the change in the shape of the structure, i.e. morphing the structure; which naturally increases the mass and uses a considerable amount of electric power. However, optimization and conservation of energy is crucially important in solar-powered HALE aircraft and particularly in flying wing aircraft that are designed for long endurance and uninterrupted flight. Another aspect of this research demonstrates the possibility to morph a folding wing configuration without relying on actuators and using only the flight-control flaps and the aerodynamic forces. An example of the kind of morphing studied in this research requires the wings to fold so as to orient a solar panel to be hit more directly by the suns rays at specific times of the day. Because of the long

endurance feature of HALE aircraft, such morphing needs to be done with as near zero energy cost as possible.

Chapter III

THEORY

3.1 Nonlinear composite beam theory

The fully intrinsic nonlinear composite beam theory [39] is based on first-order partial differential equations of the motion. These equations have neither displacement nor rotation variables, and they avoid singularities caused by to finite rotations. They contain variables that are expressed in the bases of the undeformed beam reference frame, $b(x_1)$, and the deformed beam frame, $B(x_1,t)$; see Fig. 3. These geometrically exact equations use force, moment, angular velocity and velocity variables, with maximum degree nonlinearity of order two. The equations of motion are

$$\begin{aligned} F_B' + \widetilde{K}_B F_B + f_B &= \dot{P}_B + \widetilde{\Omega}_B P_B \\ M_B' + \widetilde{K}_B M_B + (\widetilde{e}_1 + \widetilde{\gamma}) F_B + m_B &= \dot{H}_B + \widetilde{\Omega}_B H_B + \widetilde{V}_B P_B \end{aligned} \tag{1}$$

where the generalized strains and velocities are related to stress resultants and moments by the structural constitutive equations

$$\begin{Bmatrix} \gamma \\ \kappa \end{Bmatrix} = \begin{bmatrix} R & S \\ S^T & T \end{bmatrix} \begin{Bmatrix} F_B \\ M_B \end{Bmatrix} \tag{2}$$

and the inertial constitutive equations

$$\begin{Bmatrix} P_B \\ H_B \end{Bmatrix} = \begin{bmatrix} \mu\Delta & -\mu\widetilde{\xi} \\ \mu\widetilde{\xi} & I \end{bmatrix} \begin{Bmatrix} V_B \\ \Omega_B \end{Bmatrix}. \tag{3}$$

Finally, the strain- and velocity-displacement equations are used to derive the intrinsic kinematical partial differential equations [39], which are given as

$$\begin{aligned} V_B' + \widetilde{K}_B V_B + (\widetilde{e}_1 + \widetilde{\gamma}) \Omega_B &= \dot{\gamma} \\ \Omega_B' + \widetilde{K}_B \Omega_B &= \dot{\kappa} \end{aligned} \tag{4}$$

In this set of equations, F_B and M_B are column matrices of cross-sectional stress and moment resultant measures in the B frame, respectively; V_B and Ω_B are column matrices of cross-sectional

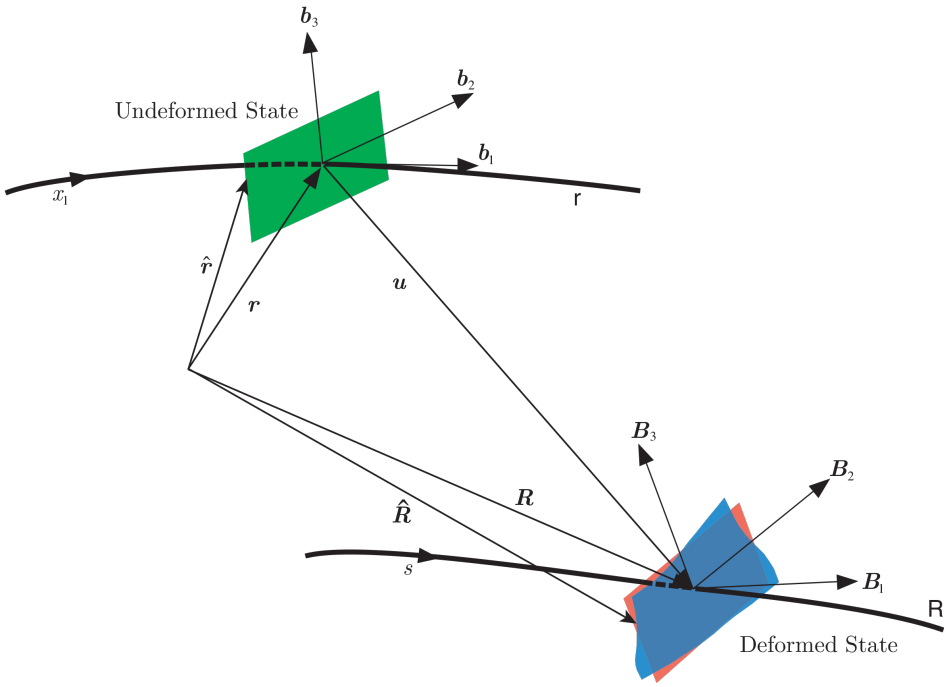

Figure 3: Sketch of beam kinematics

frame velocity and angular velocity measures in the B frame, respectively; P_B and H_B are column matrices of cross-sectional linear and angular momentum measures in the B frame, respectively; R, S, and T are 3×3 partitions of the cross-sectional flexibility matrix; Δ is the 3×3 identity matrix; I is the 3×3 cross-sectional inertia matrix; ξ is $\lfloor 0 \;\; \xi_2 \;\; \xi_3 \rfloor^T$ with ξ_2 and ξ_3 the position coordinates of the cross-sectional mass center with respect to the reference line; μ is the mass per unit length; the tilde $\widetilde{(\,)}$ denotes the antisymmetric 3×3 matrix associated with the column matrix over which the tilde is placed; $\dot{(\,)}$ denotes the partial derivative with respect to time; and $(\,)'$ denotes the partial derivative with respect to the axial coordinate, x_1. More details about these equations can be found in *Nonlinear Composite Beam Theory* [40]. This is a complete set of first-order, partial differential equations. To solve this complete set of equations, one may eliminate γ and κ using Eq. (2) and P_B and H_B using Eq. (3). Then, 12 boundary conditions are needed, in terms of force (F_B), moment (M_B), velocity (V_B) and angular velocity (Ω_B). The maximum degree of nonlinearities is only two, and because displacement and rotation variables do not appear, singularities caused by finite rotations are avoided. If needed, the position and the orientation can be calculated as

post-processing operations by integrating

$$\begin{aligned} r_i' &= C^{ib} e_1 \\ r_i + u_i' &= C^{iB}(e_1 + \gamma) \end{aligned} \tag{5}$$

and

$$\begin{aligned} (C^{bi})' &= -\widetilde{k} C^{bi} \\ (C^{Bi})' &= -(\widetilde{k} + \widetilde{\kappa}) C^{Bi} \end{aligned} \tag{6}$$

3.2 Finite-state induced flow model of Peters et al.

Two-dimensional finite state aerodynamic model of Peters et al. [67] is an state-space, thin-airfoil, inviscid, incompressible approximation of infinite state actual aerodynamic loads that accounts for wake (induced flow) effects and apparent mass effects using known airfoil parameters. It accommodates large frame (airfoil) motion as well as small deformation of the airfoil in this frame, e.g., trailing edge deflection. Although the two-dimensional version of this theory does not count for the wing tip effect but former studies[73, 67, 52] and new research explained in section 4.2 show this theory is an excellent choice for approximation of aerodynamic loads acting on high-aspect ratio wings. The lift, drag and pitching moment at the quarter-chord are given by:

$$L_{\text{aero}} = \rho b \left((C_{l_0} + C_{l_\beta}\beta) V_T V_{a_2} - C_{l_\alpha} \dot{V}_{a_3} b/2 - C_{l_\alpha} V_{a_2} (V_{a_3} + \lambda_0 - \Omega_{a_1} b/2) - C_{d_0} V_T V_{a_3} \right) \tag{7}$$

$$D_{\text{aero}} = \rho b \left(-(C_{l_0} + C_{l_\beta}\beta) V_T V_{a_3} + C_{l_\alpha} (V_{a_3} + \lambda_0)^2 - C_{d_0} V_T V_{a_2} \right) \tag{8}$$

$$M_{\text{aero}} = 2\rho b \left((C_{m_0} + C_{m_\beta}\beta) V_T - C_{m_\alpha} V_T V_{a_3} - b C_{l_\alpha}/8 V_{a_2} \Omega_{a_1} - b^2 C_{l_\alpha} \dot{\Omega}_{a_1}/32 + b C_{l_\alpha} \dot{V}_{a_3}/8 \right) \tag{9}$$

where

$$V_T = \sqrt{V_{a_2} + V_{a_3}}. \tag{10}$$

$$\sin\alpha = \frac{-V_{a_3}}{V_T} \tag{11}$$

$$\alpha_{\text{rot}} = \frac{\Omega_{a_1} b/2}{V_T} \tag{12}$$

and V_{a_2}, V_{a_3} are the measure numbers of V_a and β is the angel of flap deflection.

The effect of unsteady wake (inflow) and apparent mass appear as λ_0 and acceleration terms in the force and moment equation. The finite-state induced flow model of Peters et al. [67] is included to calculate λ_0 as:

$$[A_{\text{inflow}}]\{\dot{\lambda}\} + \left(\frac{V_T}{b}\right)\{\lambda\} = \left(-\dot{V}_{a_3} + \frac{b}{2}\dot{\Omega}_{a_1}\right)\{c_{\text{inflow}}\} \tag{13}$$

$$\lambda_0 = \frac{1}{2}\{b_{\text{inflow}}\}^T\{\lambda\} \tag{14}$$

where λ is a vector of inflow states, and $[A_{\text{inflow}}]$, $\{c_{\text{inflow}}\}$, $\{b_{\text{inflow}}\}$ are constant matrices derived in [67].

Chapter IV

NATASHA AND VALIDATIONS

[1]

4.1 Nonlinear Aeroelastic Trim and Stability of HALE Aircraft (NATASHA)

Nonlinear Aeroelastic Trim and Stability of HALE Aircraft (NATASHA) is a computer program developed in our group at Georgia Tech. NATASHA is based on a geometrically exact composite beam formulation [40] and finite-state induced flow aerodynamic model of Peters et al. [67]. The governing equations for structural model are geometrically exact, fully intrinsic and capable of analyzing the dynamical behavior of a general, nonuniform, twisted, curved, anisotropic beam undergoing large deformation. The partial differential equations' dependence on x_1 is approximated by a spatial central differencing presented by the work of [64]. The resulting nonlinear ordinary differential equations are linearized about a static equilibrium state. The equilibrium state is governed by nonlinear algebraic equations, which NATASHA solves in obtaining the steady-state trim solution using the Newton-Raphson procedure; see [64]. This system of nonlinear aeroelastic equations, when linearized about the resulting trim state, leads to a standard eigenvalue problem which NATASHA uses to analyze the stability of the structure. NATASHA is also capable of time marching the nonlinear aeroelastic system of equations using a schedule of the flight controls, which may be obtained from sequential trim solutions.

4.2 Validations

Former comparisons showed that NATASHA's results are in excellent agreement for the onset of instability [73], but behavior of the system eigenvalues below and above the flutter speed and effects of sweep on divergence and flutter speed were never validated.

[1] The content of this chapter is based on a journal article accepted for publication by *Journal of Aircraft*

4.2.1 Validation of NATASHA on the behavior of the eigenvalues

In order to study the behavior of the eigenvalues at pre- and post-stability, the classical cantilever wing model of Goland [36] was used, and the first four modes were compared with the continuum model presented by Balakrishnan [5]. Figures 4 and 5 compare the modal damping and frequency of these modes, and the results show excellent agreement for all stable modes as well as the unstable modes both below and above the flutter speed.

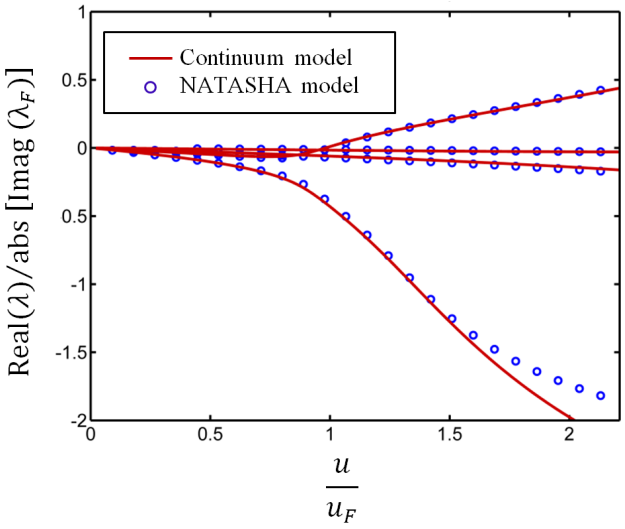

Figure 4: Real part of the roots from NATASHA compared with continuum model

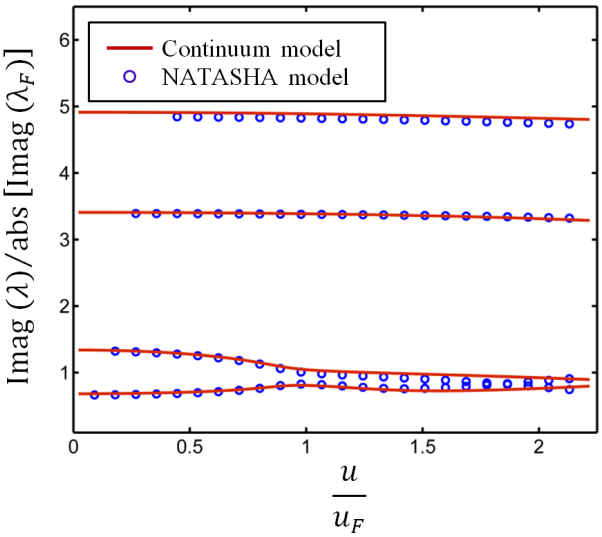

Figure 5: Imaginary part of the roots from NATASHA compared with continuum model

4.2.2 Validation of NATASHA on the effects of sweep

The effect of sweep with NATASHA was studied and the same model of Goland was considered for divergence (a static instability) and flutter [36]. In case of divergence, the results show excellent agreement (see Fig. 6) with the approximate closed-form formula, Eq. (15), given in [42] as

$$\frac{q_D}{q_{D_0}} = \frac{1 + \tan^2 \Lambda}{1 - \frac{3\pi^2}{76} \frac{GJ}{EI_2} \frac{l}{e} \tan \Lambda} \tag{15}$$

where in Eq. (15), divergence dynamic pressure (q_D) is normalized with its value at zero sweep angle (i.e., q_{D_0}), l is the span, e is the distance between elastic axis and aerodynamic center and Λ is the sweep angle. For the case of flutter, results are compared in Fig. 7 with numerical results obtained by Lottati, where U is the component of velocity vector in $\mathbf{B}_2$ direction, normalized with $U_{ref} = 400$ MPH [50].

4.3 Epilogue

NATASHA's results for the pre- and post-instability behavior of the eigenvalues were validated and the results are in excellent agreement. For the case of sweep effects, NATASHA showed an excellent agreement both in divergence and flutter speed for the classical Goland wing.

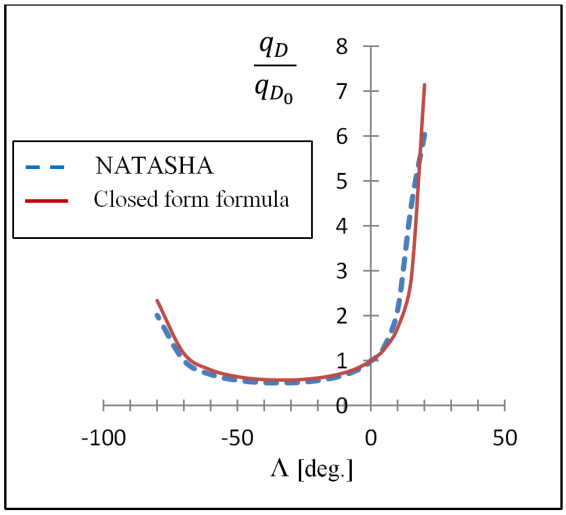

Figure 6: Effect of sweep on divergence speed using Goland model

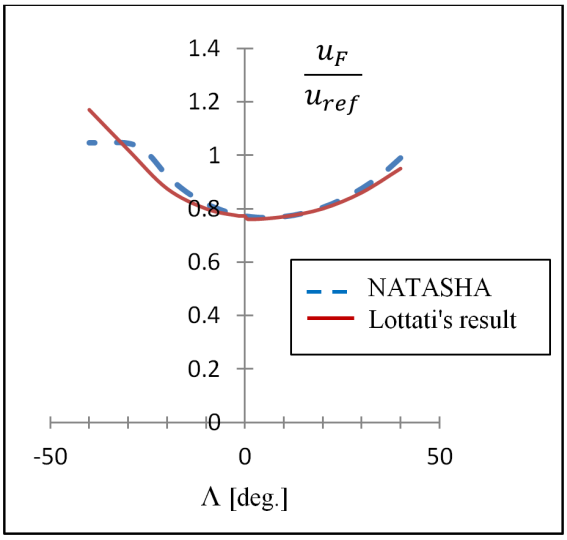

Figure 7: Effect of sweep on flutter speed using Goland model

Chapter V

NONLINEAR AEROELASTICITY OF HIGH-ASPECT-RATIO WINGS EXCITED BY TIME-DEPENDENT THRUST

[1]

5.1 Case study: flexible high-aspect ratio wing

5.1.1 Wing

A very flexible high-aspect-ratio wing (clamped-free) which displays geometrically nonlinear behavior is modeled with 20 elements; see Table 1.

Table 1: Wing and properties (SI units)

Length	16
Torsional stiffness	10^4
Out-of-plane bending stiffness	2×10^4
In-plane bending stiffness	4×10^6
Mass per unit length	0.75
Mass polar moment of inertia per unit length	0.1
Chord, c	1
Offset of aerodynamic center from elastic axis, e	0.25
Lift-curve slope, $c_{l\alpha}$	2π
Drag coefficient, c_{d_0}	0.01
Gravity, g	9.8
Air density, ρ	0.0889

[1] The content of this chapter is based on a journal article currently under review by *Journal of Nonlinear Dynamics.*

5.1.2 Engine

Design of high altitude long endurance aircraft (HALE) requires aircraft's components and equipments to be as light as possible. In this study, a light weight turboshaft engine, JetCat SPT5, appropriate for this class of aircraft is selected; see Table 2. The JetCat SPT5 engine transient model was used for two fuel profile inputs to generate realistic time-dependent thrust and angular momentum of engine.

Table 2: JetCat SPT5 turboshaft engine specifications [1, 2]

Shaft Power	8.2 (kW)
Thrust	245 (N)
Service Life	25 (hrs)
Low Pressure Spool Speed	1500-7000 (RPM)
High Pressure Spool Speed	50-170000 (RPM)
Core Pressure Ratio	2:1
Outer Diameter and Length	83×365 (mm)
High pressure spool inertia	4×10^{-5} (kg-m^2)
Low pressure spool inertia	0.0216 (kg-m^2)
Mass of the engine	3 (kg)

5.2 Flutter characteristics

As explained in section 4.1, linearized perturbation about equilibrium state leads to a standard eigenvalue problem which NATASHA solves to find the flutter characteristics of the wing. In this study, the behavior of the eigenvalues for the clean wing with and without gravity, and the wing with the engine at 75% span forward of the elastic axis is presented. The present work considers the effect of drag.

5.2.1 Clean wing without gravity

In the absence of engine and gravity the wing flutters at 32.1 m/s with a frequency of 22.534 rad/sec. The associated mode is a first bending-torsion mode and divergence occurs at 34.6 m/s. The behavior of the eigenvalues are shown in Figs. 8 and 9. Comparison between the result in present work and previously published work [65] shows that drag does not have a significant effect.

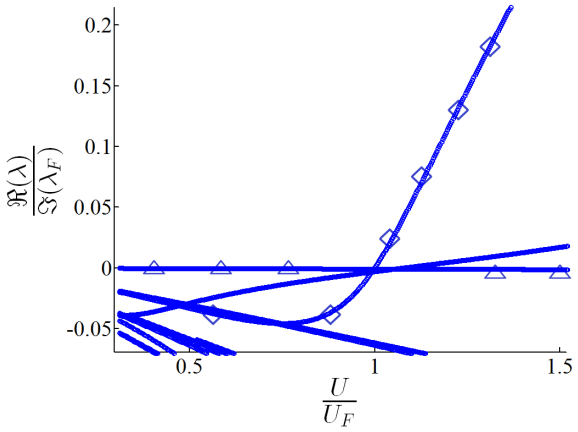

Figure 8: Normalized real part of eigenvalue for clean wing neglecting gravity

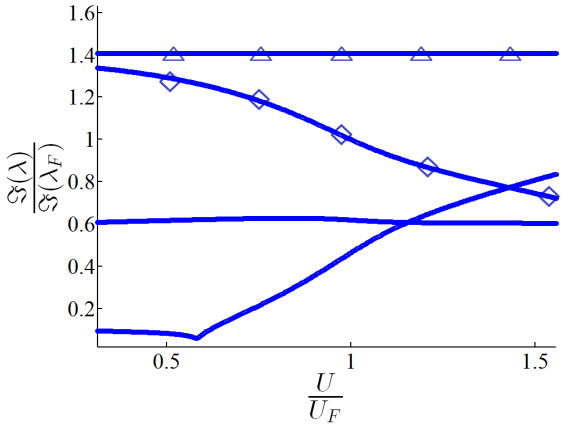

Figure 9: Normalized imaginary part of eigenvalue for clean wing neglecting gravity

5.2.2 Clean wing with gravity

NATASHA captures a hump flutter mode when effect of gravity (g=9.8 m/s^2) is considered. The hump mode contains motion of first bending and torsion mode, and flutters at 22.4 m/s with a

frequency of 12.199 rad/sec. This result is used to normalize flutter characteristics presented in this study. At a higher speed this mode returns to being stable and at 45 m/s second bending-torsion mode with a frequency of of 27.406 becomes unstable; see Figs. 10 and 11.

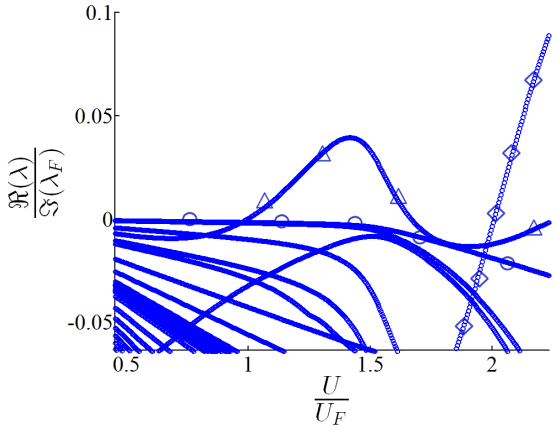

Figure 10: Normalized real part of eigenvalue for clean wing with gravity

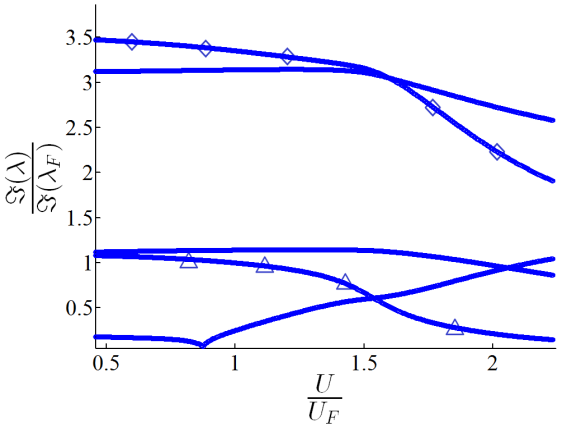

Figure 11: Normalized imaginary part of eigenvalue for clean wing with gravity

5.2.3 Wing with engine

Engine placement at 75% span, one meter forward of the elastic axis, i.e., $r = 1, \psi = 0$, significantly increases flutter speed up to 76.4 m/s. The flutter mode is a combination of first and second bending with a frequency of 1.9637 rad/sec. Slightly above this speed, another mode becomes unstable. The motion of this mode is a combination of first and second edgewise bending, first flatwise bending, and second torsion modesThe behavior of eigenvalues are shown in Figs. 12 and 13.

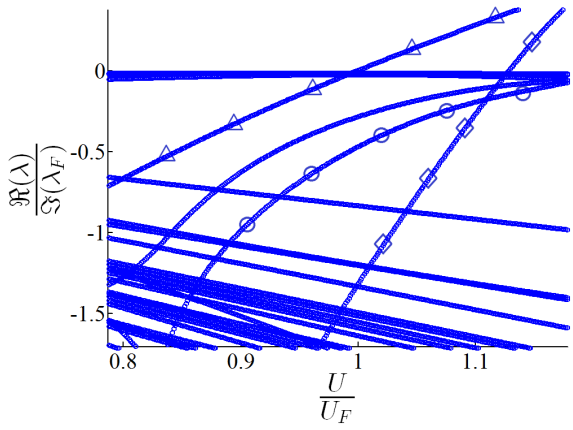

Figure 12: Normalized real part of eigenvalue for clean wing neglecting gravity

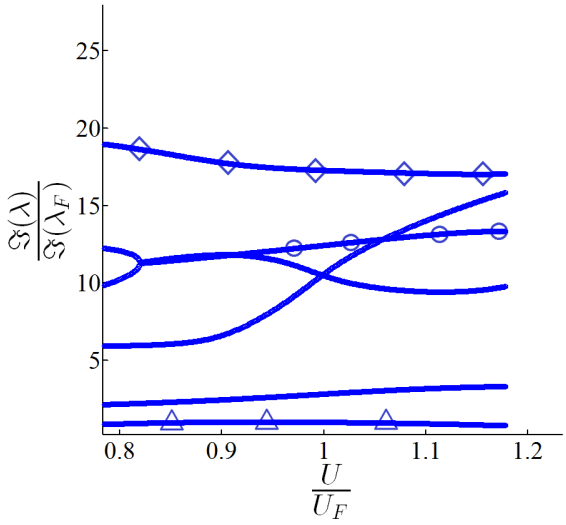

Figure 13: Normalized imaginary part of eigenvalue for clean wing neglecting gravity

5.3 Effect of engine placement on flutter characteristics of the wing

In order to study the effect of engine placement, a turboshaft engine (JetCat SP5) with known thrust, mass, moments of inertia, and angular momentum which operates at cruise condition is placed along the span. The engine mount is offset from the elastic axis in the plane of cross section while the engine orientation is maintained; see Fig. 14. The engine offsets from the elastic axis are presented in polar coordinates with (r, ψ). r is radial offset of the engine from the elastic axis, normalized by chord, ψ is the polar angle and η is the dimensionless length in the $\mathbf{b}_1$ direction, along which

the engine is located. It is to be noted that this study does not take into account the flexibility of engine's mount and nacelle as well as effects of wing and propeller aerodynamic interaction.

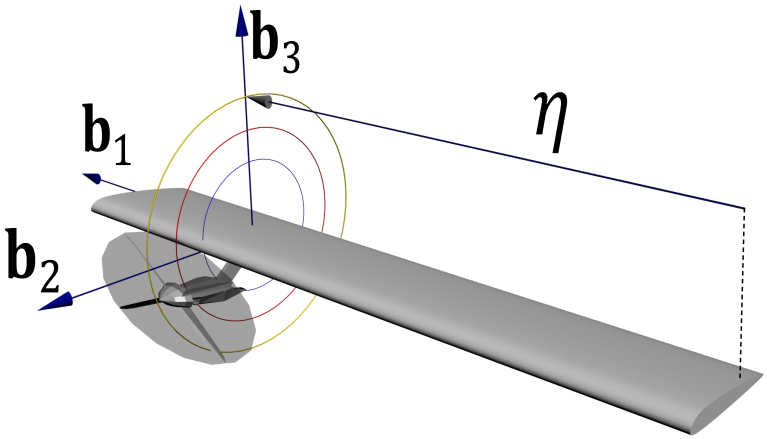

Figure 14: Schematic view of the wing with engine

5.3.1 Neglecting effects of gravity

Some aeroelastic analyses do not consider the effect of gravity [65, 28]. Figures 15 – 18 show the contour of the normalized flutter speed and frequency for engine placement along span in normal and chordwise direction ignoring the gravity effect. Engine placement between 60% to 80% span, offset forward of the elastic axis increases flutter speed; see Fig. 15. For engine placement between 70% to 95% span, offset in normal direction increases the flutter speed by 75% (see Fig. 17) while moving the engine toward the tip decreases the flutter frequency; see Fig. 18. The plane of symmetry in the contour of flutter speed and frequency is due to absence of gravity; see Figs. 17 – 18.

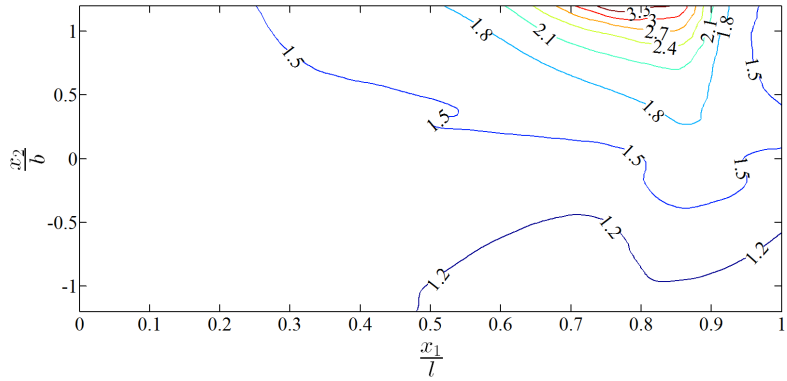

Figure 15: Contour of normalized flutter speed for engine placement in chordwise direction, i.e., $\mathbf{b_2}$; neglecting gravity

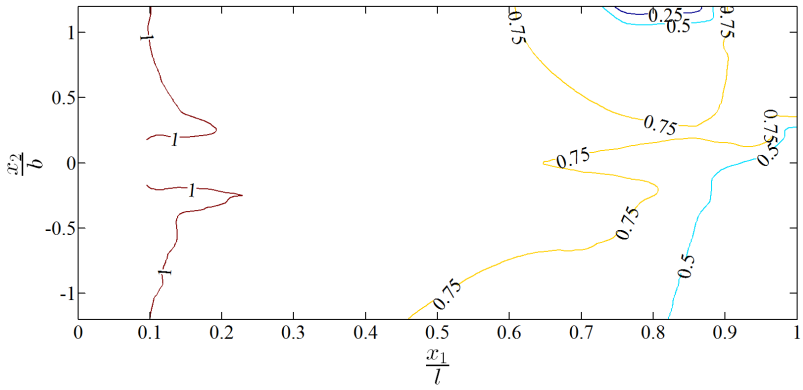

Figure 16: Contour of normalized flutter frequency for engine placement in chordwise direction, i.e., $\mathbf{b_2}$; neglecting gravity

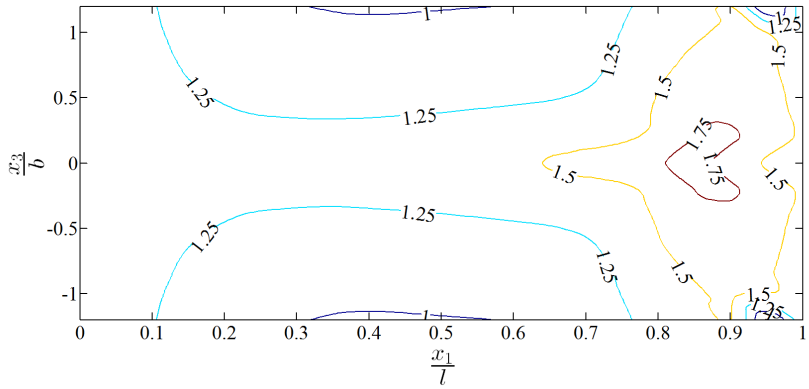

Figure 17: Contour of normalized flutter speed for engine placement in normal direction, i.e., $\mathbf{b_3}$; neglecting gravity

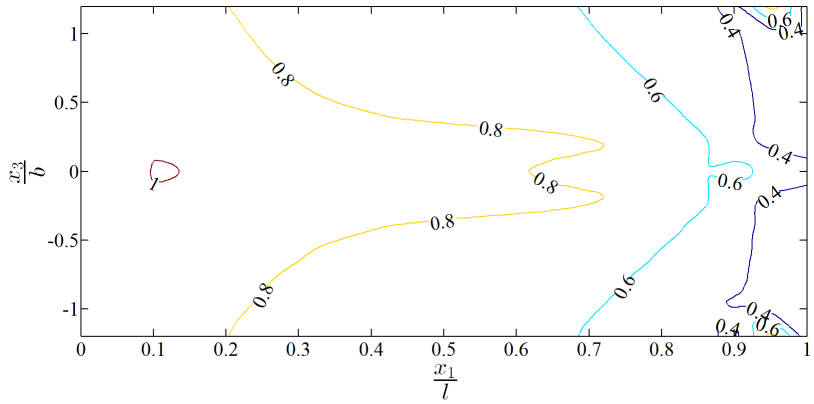

Figure 18: Contour of normalized flutter frequency for engine placement in chordwise direction, i.e., $\mathbf{b_3}$; neglecting gravity

5.3.2 Considering effects of gravity

Gravity ($g = 9.8$ m/s^2) plays an important role in flutter characteristics of flexible high-aspect-ratio wings. The effect of gravity is negligible for conventional wings, but for HALE wings it becomes important because it affects the trim solution in a non-neglible way. Consequently, with highly flexible wings such as those of HALE aircraft, one should expect load factor to have an influence on flutter, unlike the case of conventional aircraft. This effect significantly appears for the cases where the equilibrium states are distinct from those obtained without considering gravity. If they are distinct, stability is affected since the perturbation about the equilibrium state is changed.

For engine placement in the chordwise direction, offset forward of the elastic axis, this effect slightly changes the flutter speed, the trend of the contours of flutter speed is unaffected since the equilibrium state and the perturbation about equilibrium state slightly changes. However, one needs to note that an analysis in which gravity is neglected does not predict drop of flutter speed for engine placement on the inboard portion of the wing, behind elastic axis; compare Figs. 15 and 19. As it is expected, the contours of normalized flutter frequency show that presence of gravity increases flutter frequency; see Figs. 16 and 20. For engine placement along the span in normal direction, i.e., $\mathbf{b_2}$, the trend of flutter speed and frequency changes (see Figs. 18 and 22). These results show that flutter analysis without gravity is not capable to predict the drop of flutter speed at 35% to 55% span; see Figs. 17 and 21. In both cases of engine placement, i.e., in-plane and out-plane, neglecting effect of gravity does not predict the drop of flutter speed at 35% to 55% span but it can capture the area where maximum flutter speed occurs. It is noteworthy that these areas coincide with the area of maximum and minimum kinetic energy density of the second bending and torsion modes of the wing which is presented in section 5.5.

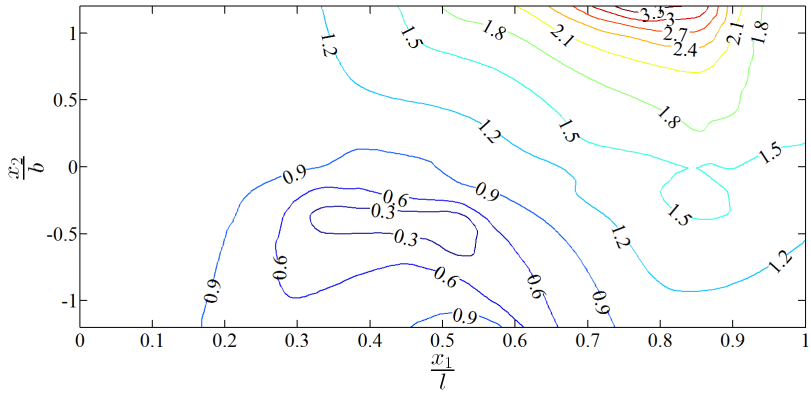

Figure 19: Contour of normalized flutter speed for engine placement in chordwise direction, i.e., $\mathbf{b_2}$; considering gravity, g = 9.8 m/s^2

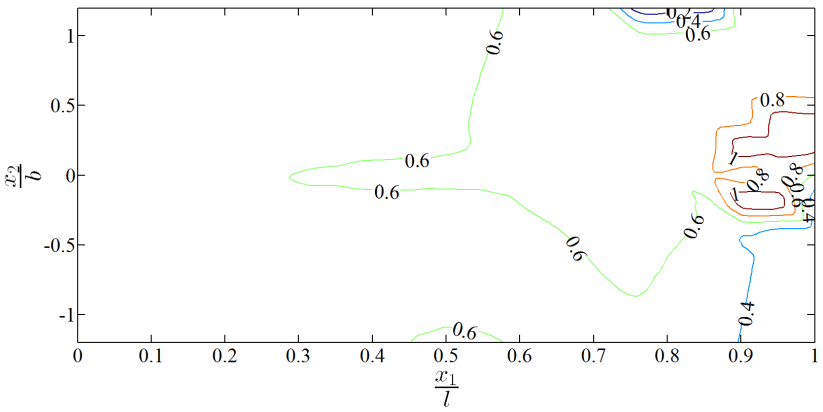

Figure 20: Contour of normalized flutter frequency for engine placement in chordwise direction, i.e., $\mathbf{b_2}$; considering gravity, g = 9.8 m/s^2

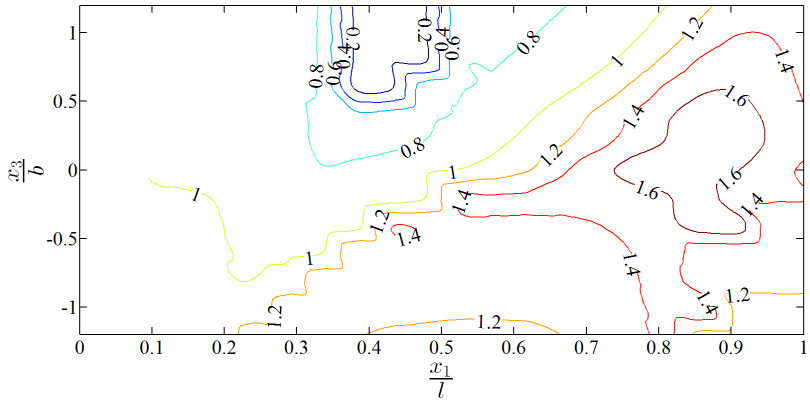

Figure 21: Contour of normalized flutter speed for engine placement in normal direction, i.e., $\mathbf{b_3}$; considering gravity, g = 9.8 m/s^2

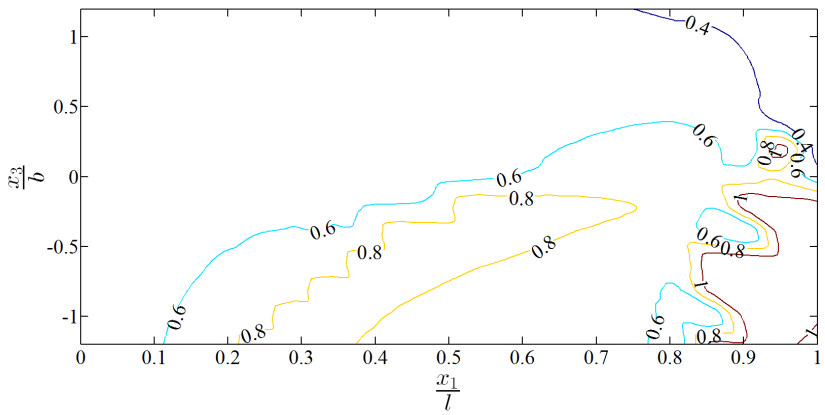

Figure 22: Contour of normalized flutter frequency for engine placement in chordwise direction, i.e., $\mathbf{b_3}$; considering gravity, g = 9.8 m/s^2

Effects of finite variation of engine's inertial and dynamical parameters on flutter characteristics was briefly explored. It was noticed that the flutter characteristics vary nonlinearly with respect to these parameters and the location of the engine. This requires further investigations and parametric studies.

5.4 Effect of load factor and engine placement on flutter characteristics

Aircraft experience different load factors as they maneuver or undergo different flight conditions. For instance, the aircraft's wing will experience a higher load factor when it flies at a different bank angle. At straight level flight, load factor is one and in turning flight the load factor is normally greater than one and follows the following equation:

$$n = \frac{1}{\cos\phi} \tag{16}$$

where ϕ represents the aircraft's bank angle and n is the load factor. In this study, effect of load factor is modeled with change in the magnitude of gravity vector, i.e., $\mathbf{g}$. To investigate this effect, contours of the flutter speed for engine placement in normal and chordwise direction for bank angles equal to 30°, 45° and 60° is presented in Figs. 23 – 34.

For load factors of 1.2 and 1.4 (which correspond to bank angles of approximately 30° and 45°), flutter characteristics still have the same behavior compared to straight level flight, i.e., zero bank

angle. At 60°, load factor increases to two, and the effects become significant in flutter speed and its sensitivity to engine placement; see Fig. 31 and 33. At this load factor, NATASHA's results show that flutter speed decreases (see Figs. see Figs. 24 – 34), and for engine placement between 20% to 60% span, offset forward of the elastic axis, i.e., in the chordwise direction, one can attain a higher flutter speed; see Fig. 31, and for engine placement in normal direction, flutter speed increases on the inboard portion of the wing and flutter characteristics are independent of the offsets from elastic axis at each span-wise location; see Figs. 33 – 34.

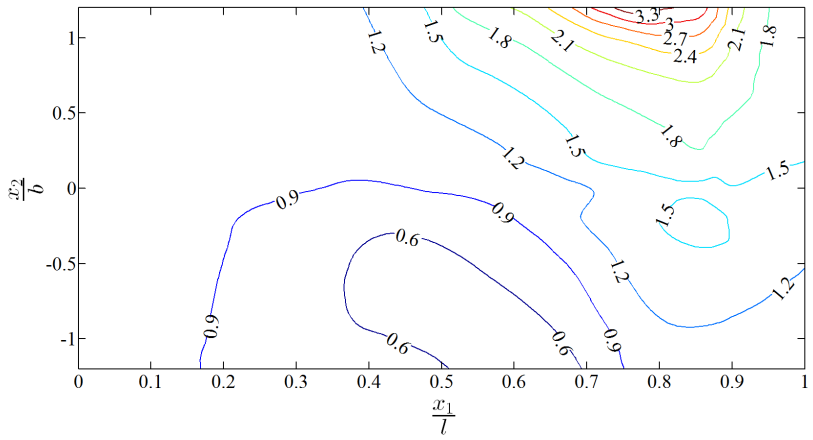

Figure 23: Contour of normalized flutter speed for engine placement in chordwise direction, i.e., $\mathbf{b_2}$, when load factor is 1.2

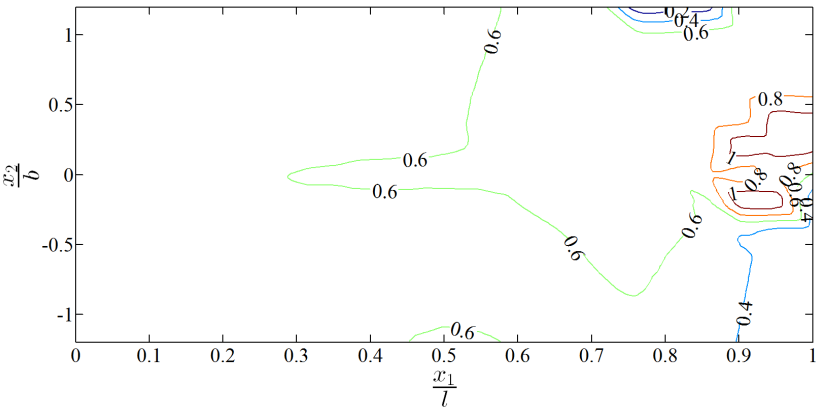

Figure 24: Contour of normalized flutter frequency for engine placement in chordwise direction, i.e., $\mathbf{b_2}$, when load factor is 1.2

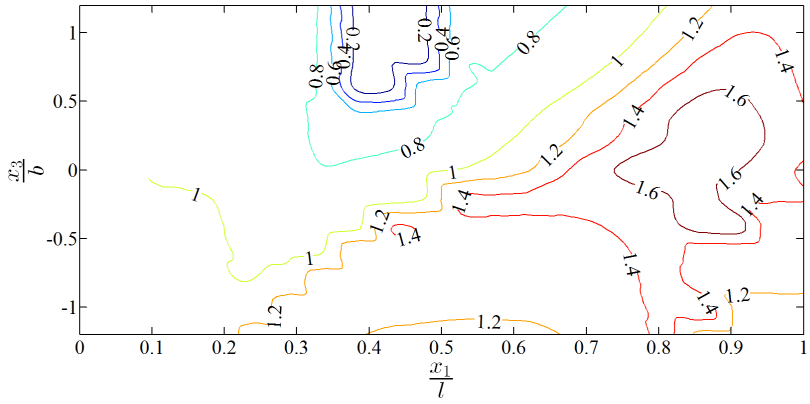

Figure 25: Contour of normalized flutter speed for engine placement in normal direction, i.e., $\mathbf{b_3}$, when load factor is 1.2

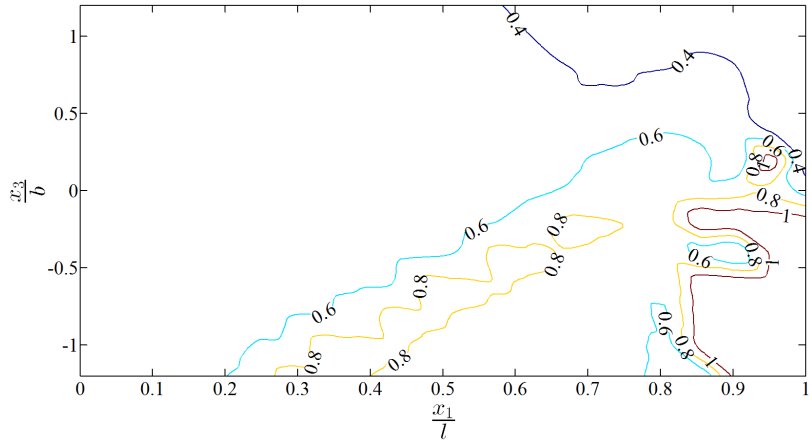

Figure 26: Contour of normalized flutter frequency for engine placement in chordwise direction, i.e., $\mathbf{b_3}$, when load factor is 1.2

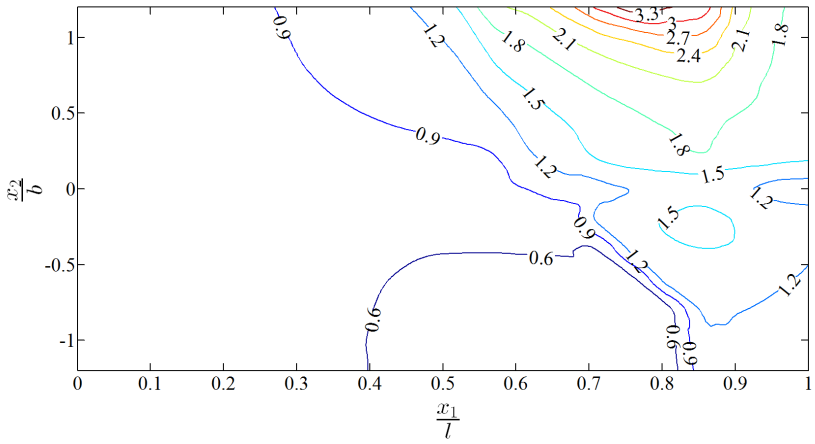

Figure 27: Contour of normalized flutter speed for engine placement in chordwise direction, i.e., $\mathbf{b_2}$, when load factor is 1.4

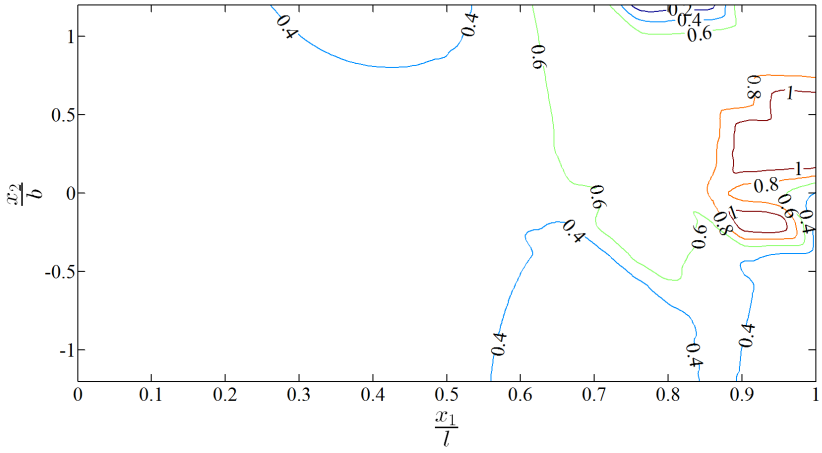

Figure 28: Contour of normalized flutter frequency for engine placement in chordwise direction, i.e., $\mathbf{b_2}$, when load factor is 1.4

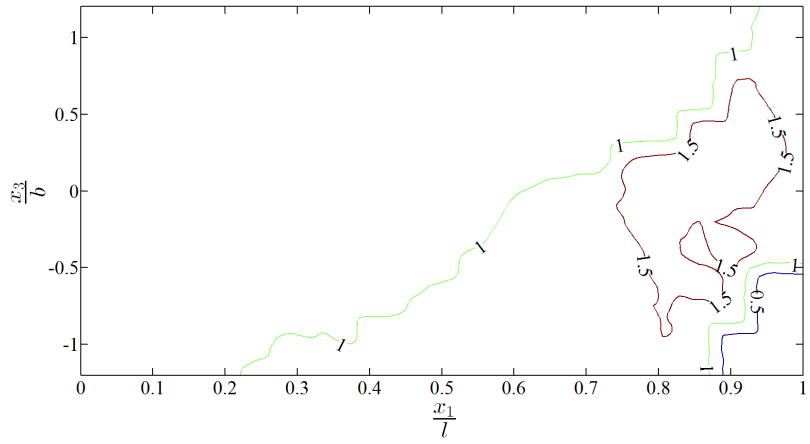

Figure 29: Contour of normalized flutter speed for engine placement in normal direction, i.e., $\mathbf{b_3}$, when load factor is 1.4

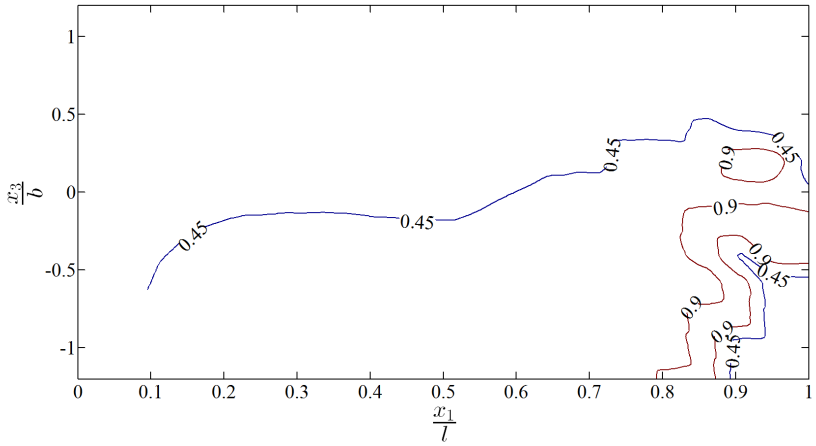

Figure 30: Contour of normalized flutter frequency for engine placement in chordwise direction, i.e., $\mathbf{b_3}$, when load factor is 1.4

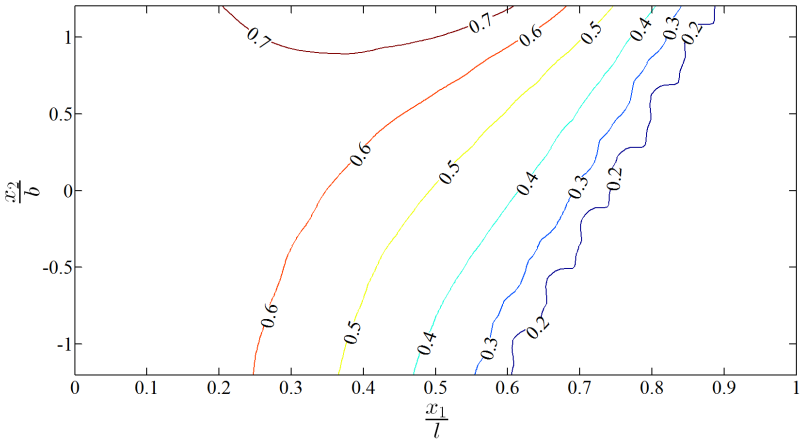

Figure 31: Contour of normalized flutter speed for engine placement in chordwise direction, i.e., $\mathbf{b_2}$, when load factor is 2

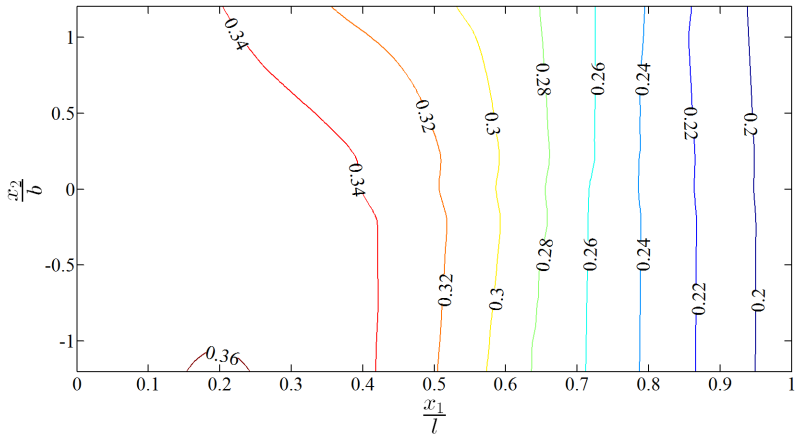

Figure 32: Contour of normalized flutter frequency for engine placement in chordwise direction, i.e., $\mathbf{b_2}$, when load factor is 2

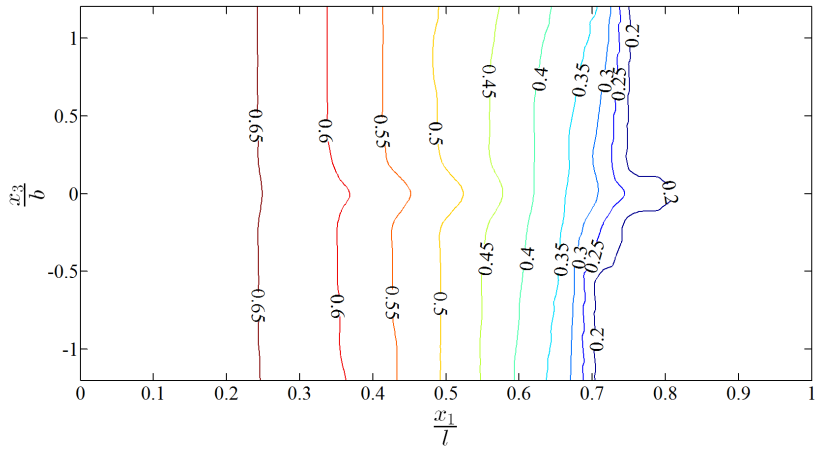

Figure 33: Contour of normalized flutter speed for engine placement in normal direction, i.e., $\mathbf{b_3}$, when load factor is 2

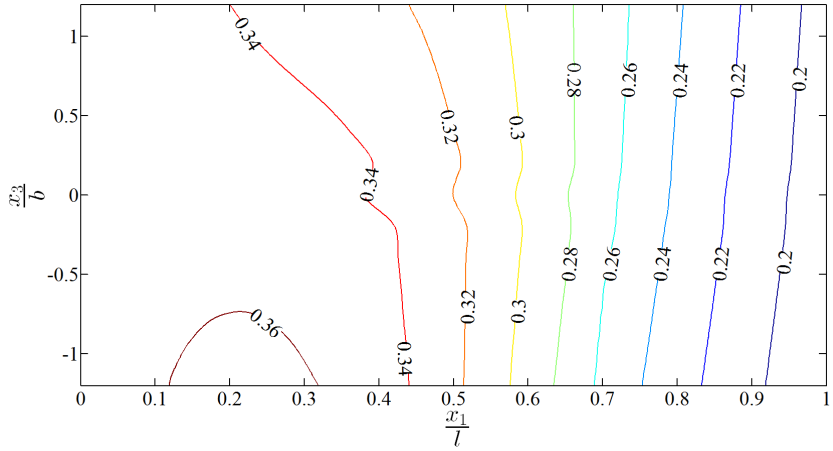

Figure 34: Contour of normalized flutter frequency for engine placement in chordwise direction, i.e., $\mathbf{b_3}$, when load factor is 2

5.5 Area of minimum kinetic energy density of the mode

Engine placement at certain location has the potential to increase the flutter speed in two ways. One is the location where lower frequency flutter mode could be relegated to a higher frequency mode and the other is the location where the fluid structure interaction is decreased. Both criteria could be met at the area of minimum kinetic energy of the mode. In other words, engine placement at the area of minimum kinetic energy of the modes has the potential to decrease fluid structure

interaction and enforce the structure to flutter at a higher mode. To further explore this possibility, the area of minimum kinetic energy density of the first two bending and torsion modes of the wing, in the absence of engine, gravitational and aerodynamic forces is presented in Figs. 35 – 38. For the first bending and torsion this area is minimum at the root of the wing; see Figs. 35 – 37. For the second bending mode the area of minimum kinetic energy density of the mode has a local minima outboard 85% span and for second torsion modes this minimum moves to the region between 70% to 90% span; see Figs. 36 – 38. For engine placement forward of the elastic axis, the unstable mode contains a combination of first and second bending along with second torsion; and when the engines are placed around 50% to 70% span, there is a noticeable increase in flutter speed. This is close to the area of minimum kinetic energy of the second bending and torsion modes; see Figs. 36 – 38.

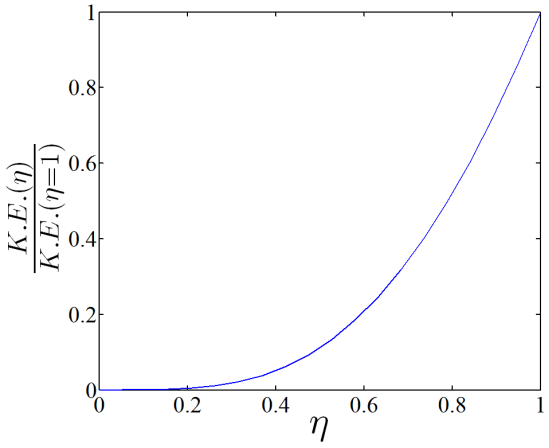

Figure 35: Normalized kinetic energy of the first bending mode of the wing

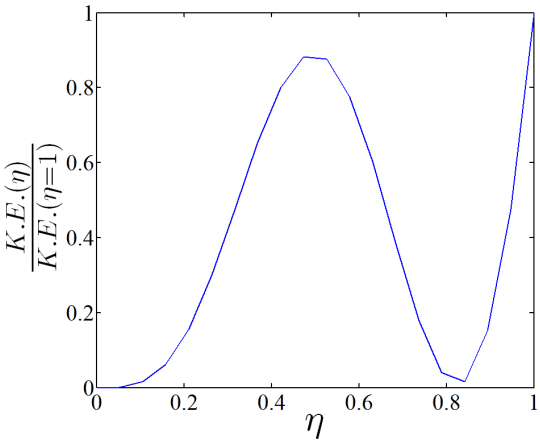

Figure 36: Normalized kinetic energy of the second bending mode of the wing

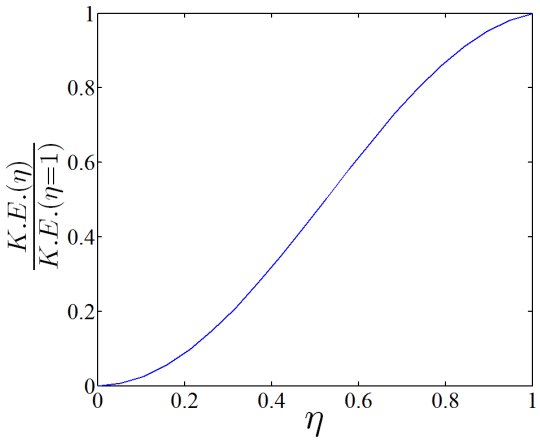

Figure 37: Normalized kinetic energy of the first torsion mode of the wing

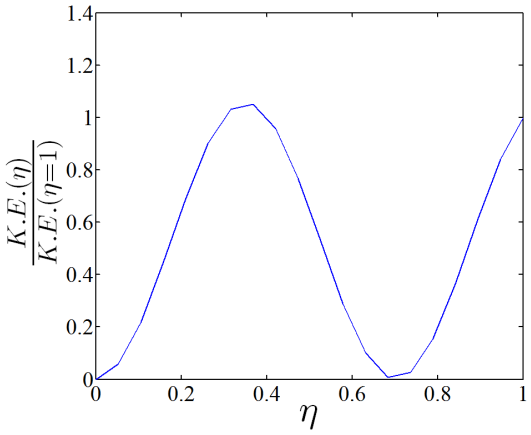

Figure 38: Normalized kinetic energy of the second torsion mode of the wing

5.6 Nonlinear aeroelastic response

Effects of engine placement with time-dependent engine thrust and dynamics on nonlinear aeroelastic response of the high-aspect-ratio wing are studied by the second-order, central-difference, time marching algorithm with high frequency damping in NATASHA [64]. An appropriate time step is 0.05 seconds. The transient behavior of the engine, i.e., thrust and angular momentum of spools, for two fuel input profiles is simulated using JetCat SP5 engine simulator [1, 2]. At an air velocity of 20 m/s, the aeroelastic response of the wing excited by time-dependent thrust, for engine placement along the span (25%, 50%, 75% span and at the tip of the wing) and with offset from the elastic axis of the order of a chord length is studied for two types of excitations.

5.6.1 Response to impulse excitation

A sudden momentarily increase in the fuel flow may be caused by pilot command, an error in the engine control system, or even wear and tear of engine components. Although the fault detection system typically removes these errors, an aeroelastically stable engine placement will increase the safety factor and always protect the wing from the dramatic consequences of these sorts of instabilities.

In this simulation, the fuel flow rate experiences a rectangular pulse type of input from cruise to maximum level during two seconds and returns to cruise throttle condition again; see Fig. 39. This fuel profile leads to realistic sudden increase of thrust which resembles an impulse kind of engine excitation; see Fig. 40. The transient engine model shows that effects of engine dynamics

are significant and one needs to take into account the effect of angular momentum of low and high pressure engine spool in calculation; see Figs. 41 and 42.

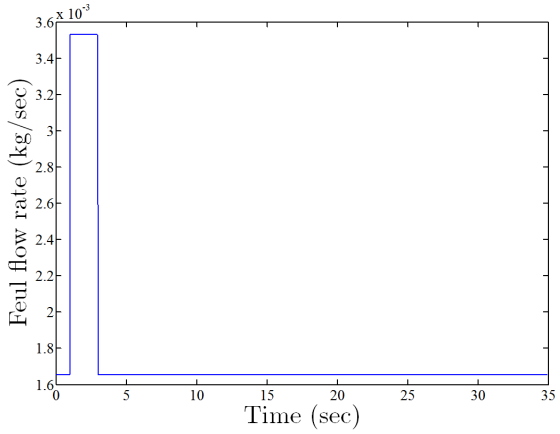

Figure 39: Fuel flow rate profile for impulse excitation

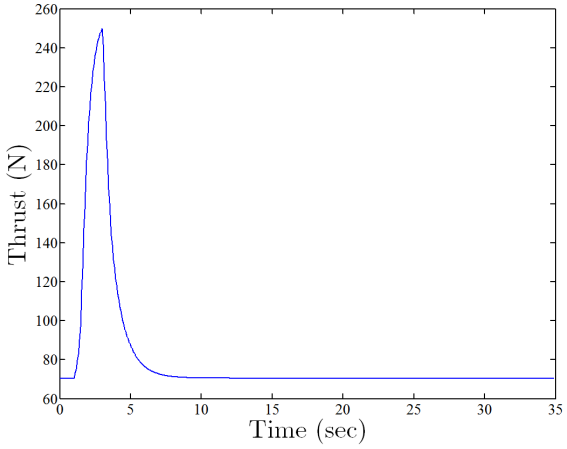

Figure 40: JetCat SP5 engine thrust simulation for impulse fuel profile

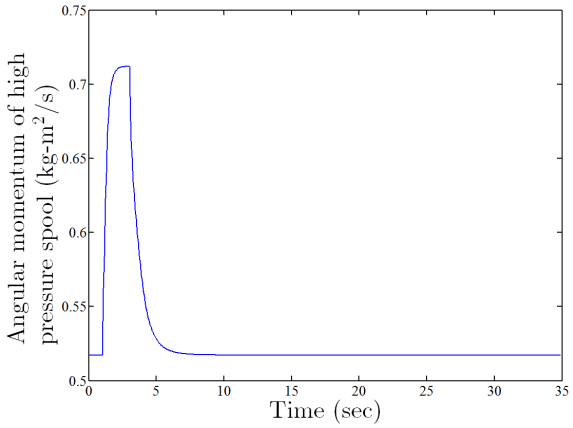

Figure 41: JetCat SP5 engine high pressure angular momentum simulation for impulse fuel profile

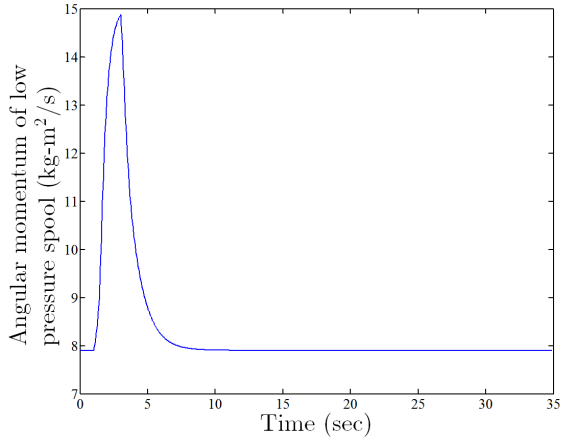

Figure 42: JetCat SP5 engine low pressure angular momentum simulation for impulse fuel profile

– *25% span:* Stability analysis with engine thrust and angular momentum at cruise level show that engine placement with no offset and at $r = 1$ and $\psi = 90°$, $135°$ and $180°$, the above considered air speed is above flutter speed and other locations are aeroelastically stable in a linearized analysis. The time march results show that excitation at this locations attenuate quickly.

– *50% span:* It can be gleaned from the stability analysis that most of engine placements at these locations are sub-critical and the excitation dies out whereas for two cases where the engine placements are supercritical; case(a) engine placement at $r = 1$ and $\psi = 90°$, the excitation

still dies out and case(b) at $r = 1$ and $\psi = 135°$ where the excitation leads to a stable Limit Cycle Oscillation (LCO); see Figs. 43 – 48.

– *75% span:* The results from the linearized stability analysis demonstrate that engine placement at $r = 1$, $\psi = 90°$ and $180°$ is supercritical; in both cases the excitation dies out. Engine placement at $r = 1$, $\psi = 135°$ is supercritical and leads to a stable LCO; see Figs. 49 – 54. Other engine placements at this location are within subcritical regime and the excitations die out.

– *100% span:* For engine placement at the tip of the wing, only engine placement at $r = 1$, $\psi = 180°$ is supercritical and excitation at this location leads to stable LCO. When engine is placed offset forward of the elastic axis, i.e., $r = 1$, $\psi = 0°, 45°, 90°, 270°$ and $315°$, the excitation dies out and when engine is place at $r = 1$, $\psi = 135°$ excitation leads to a stable LCO and after 50 seconds it quickly dies out; see Figs 55 – 57. When the engine is offset at $r = 1$, $\psi = 225°$, excitation below flutter speed leads to stable LCO; see Figs. 58 – 63.

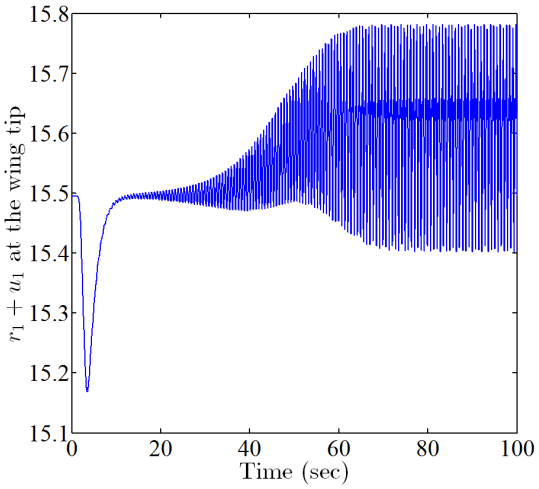

Figure 43: Wing tip position along $\mathbf{b_1}$ vs. time, for engine placement at 50% span with $r = 1$ and ψ= 135°

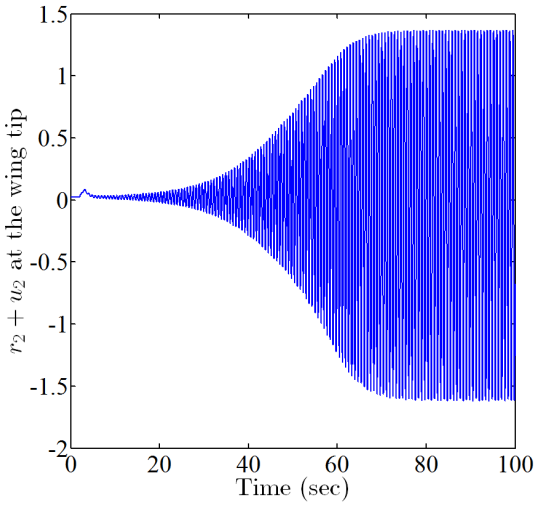

Figure 44: Wing tip position along $\mathbf{b_2}$ vs. time, for engine placement at 50% span with $r = 1$ and ψ= 135°

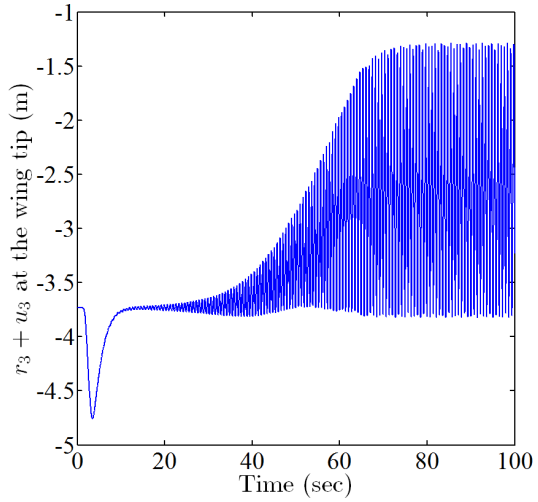

Figure 45: Wing tip position along $\mathbf{b_3}$ vs. time, for engine placement at 50% span with $r = 1$ and ψ= 135°

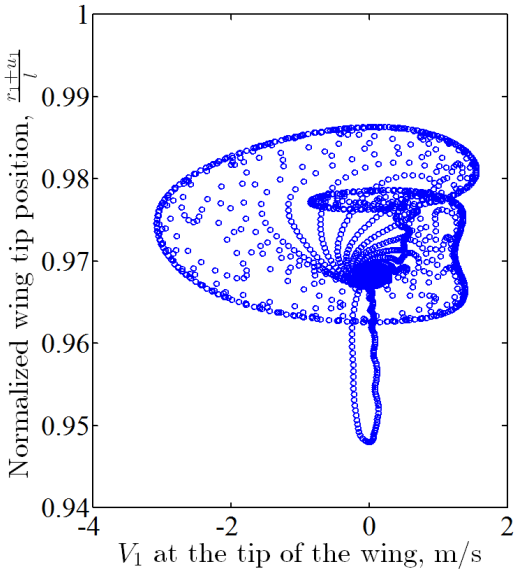

Figure 46: Normalized wing tip position vs. velocity in $\mathbf{b_1}$ direction, for engine placement at 50% span with $r = 1$ and $\psi = 135°$

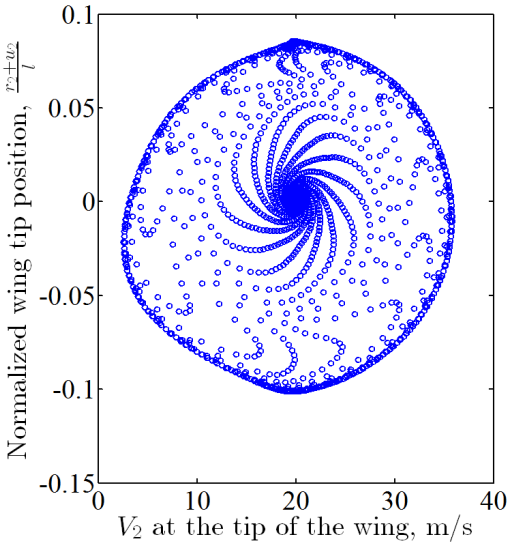

Figure 47: Normalized wing tip position vs. velocity in $\mathbf{b_2}$ direction, for engine placement at 50% span with $r = 1$ and $\psi = 135°$

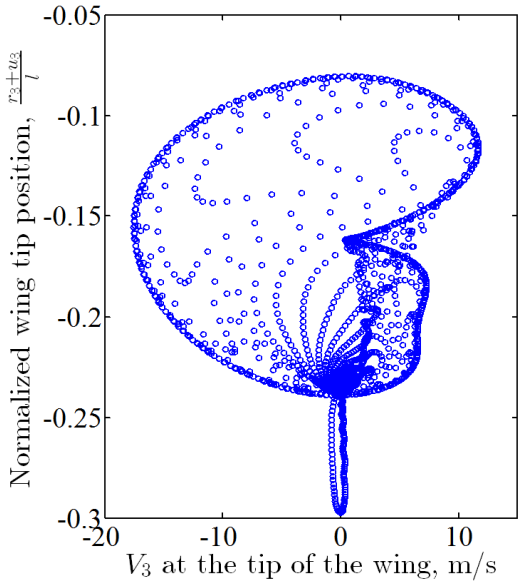

Figure 48: Normalized wing tip position vs. velocity in $\mathbf{b_3}$ direction, for engine placement at 50% span with $r = 1$ and ψ= 135°

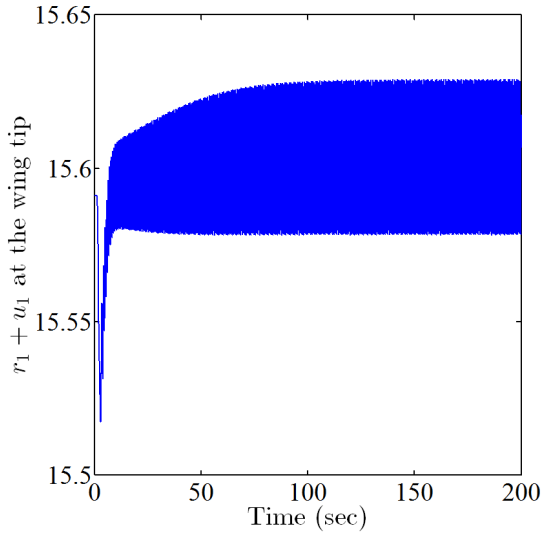

Figure 49: Wing tip position along $\mathbf{b_1}$ vs. time, for engine placement at 75% span with $r = 1$ and ψ= 135°

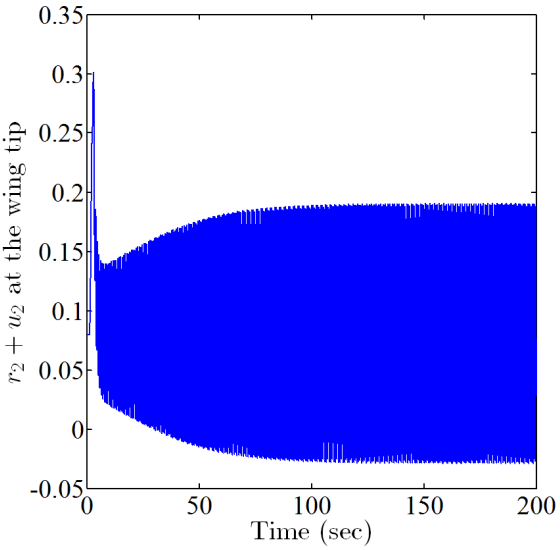

Figure 50: Wing tip position along $\mathbf{b_2}$ vs. time, for engine placement at 75% span with $r = 1$ and $\psi = 135°$

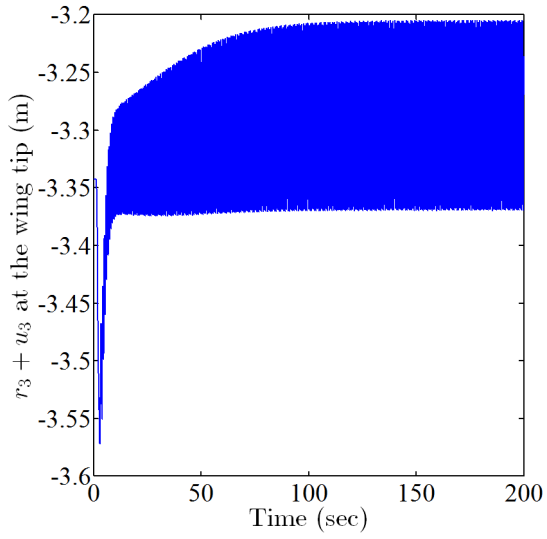

Figure 51: Wing tip position along $\mathbf{b_3}$ vs. time, for engine placement at 75% span with $r = 1$ and $\psi = 135°$

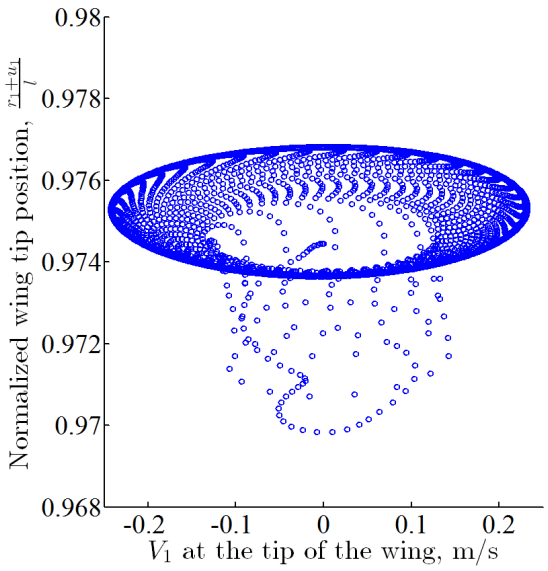

Figure 52: Normalized wing tip position vs. velocity in $\mathbf{b_1}$ direction, for engine placement at 75% span with $r = 1$ and ψ= 135°

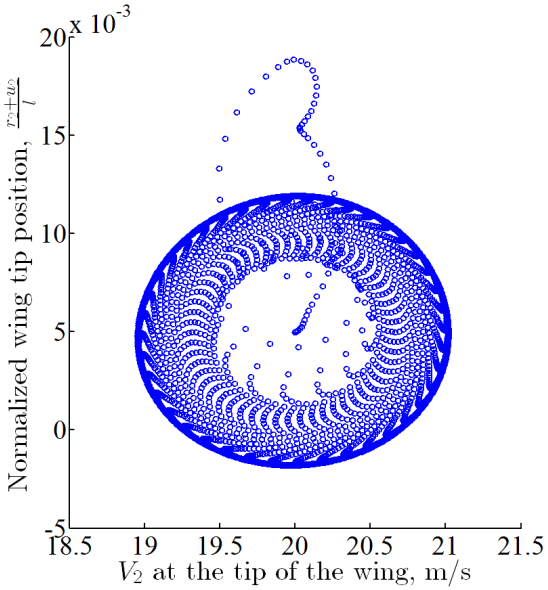

Figure 53: Normalized wing tip position vs. velocity in $\mathbf{b_2}$ direction, for engine placement at 75% span with $r = 1$ and ψ= 135°

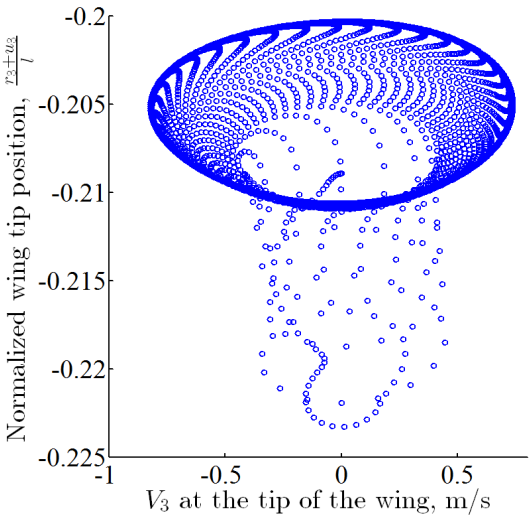

Figure 54: Normalized wing tip position vs. velocity in $\mathbf{b_3}$ direction, for engine placement at 75% span with $r = 1$ and ψ= 135°

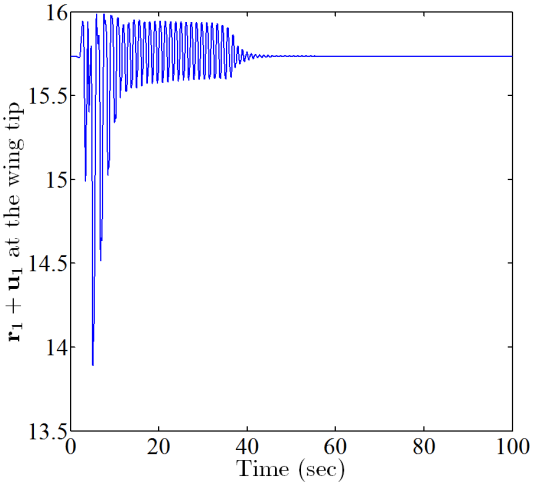

Figure 55: Wing tip position along $\mathbf{b_1}$ vs. time, for engine placement at 100% span with $r = 1$ and ψ= 135°

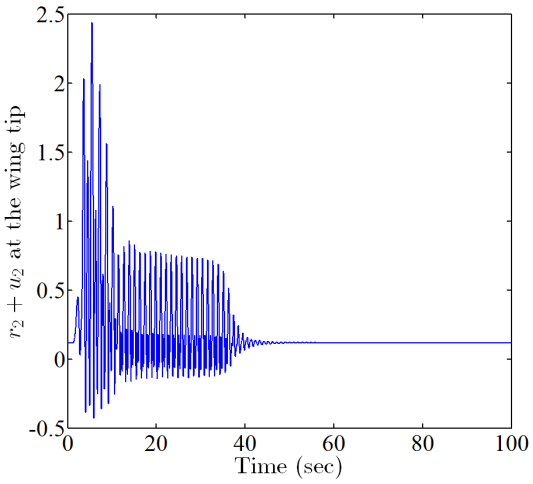

Figure 56: Wing tip position along $\mathbf{b_2}$ vs. time, for engine placement at 100% span with $r = 1$ and $\psi = 135°$

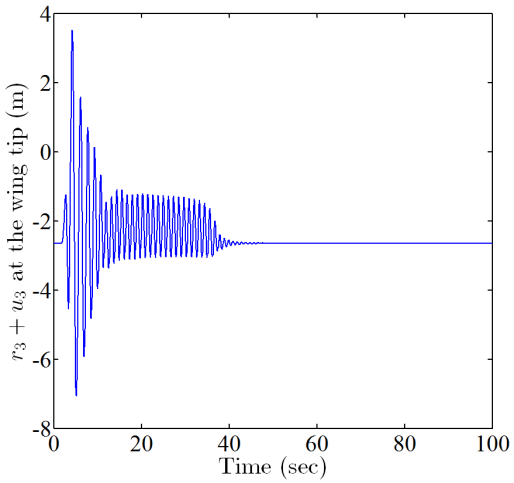

Figure 57: Wing tip position along $\mathbf{b_3}$ vs. time, for engine placement at 100% span with $r = 1$ and $\psi = 135°$

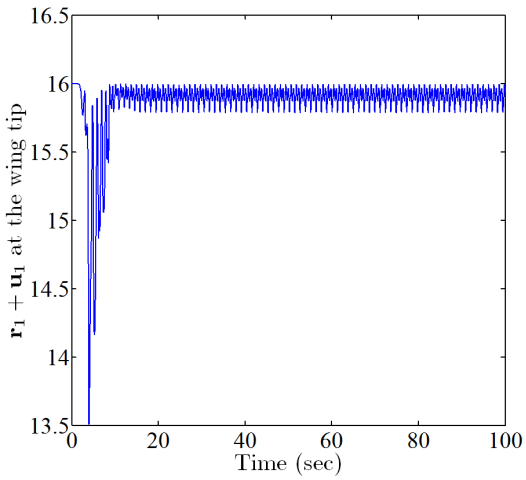

Figure 58: Wing tip position along $\mathbf{b_1}$ vs. time, for engine placement at 100% span with $r = 1$ and $\psi = 225°$

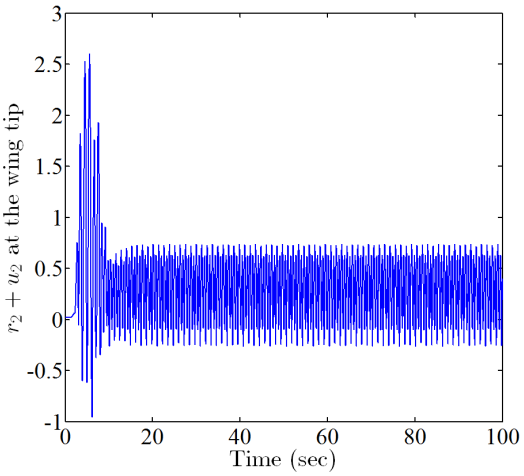

Figure 59: Wing tip position along $\mathbf{b_2}$ vs. time, for engine placement at 100% span with $r = 1$ and $\psi = 225°$

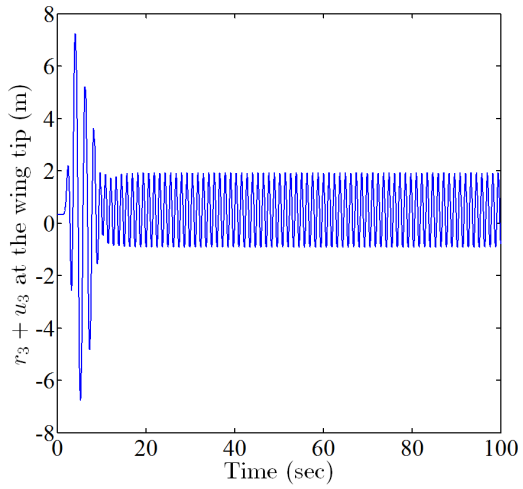

Figure 60: Wing tip position along $\mathbf{b_3}$ vs. time, for engine placement at 100% span with $r = 1$ and $\psi = 225°$

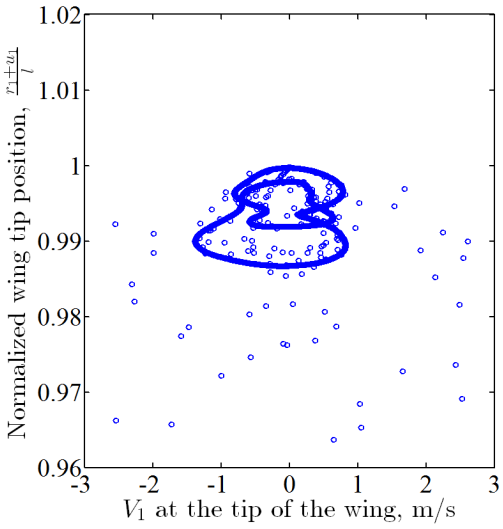

Figure 61: Normalized wing tip position vs. velocity in $\mathbf{b_1}$ direction, for engine placement at 100% span with $r = 1$ and $\psi = 225°$

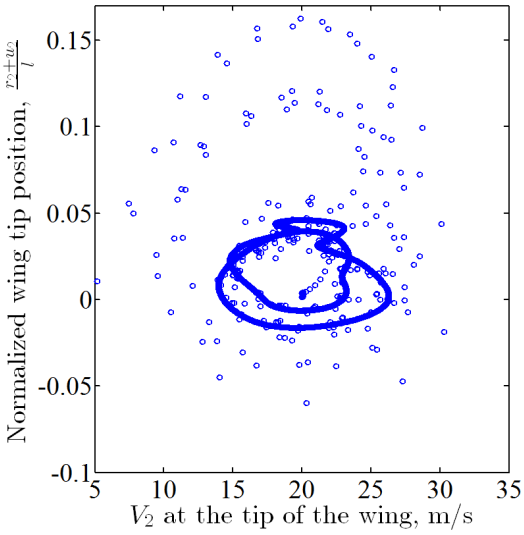

Figure 62: Normalized wing tip position vs. velocity in $\mathbf{b_2}$ direction, for engine placement at 100% span with $r = 1$ and ψ= 225°

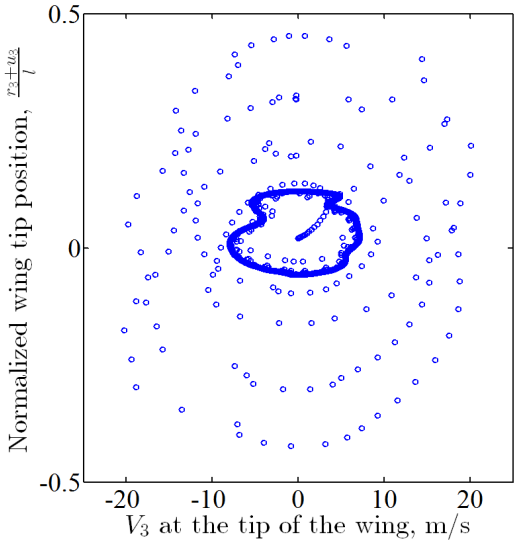

Figure 63: Normalized wing tip position vs. velocity in $\mathbf{b_3}$ direction, for engine placement at 100% span with $r = 1$ and ψ= 225°

5.6.2 Response to ramp excitation

The increase of thrust from cruise to maximum level is typically required to increase the speed or go through different maneuvers. Flutter analysis is incapable of study the effects of large excitation

about the equilibrium state and can only predict the stability of the wing at a given thrust, angular momentum and air speed; it does not convey any information regarding the transition from one trim condition to another. This fact that engine excitation is of the kind of excitation in the large, the aeroelastic stability of such systems requires time domain analysis to convey correct information in that regard. In this simulation, the fuel flow rate profile increases linearly within 5 seconds from cruise to maximum level and remains at that rate for the rest of simulation; see Fig. 64. JetCat SP5 engine model simulates thrust and engine dynamics for this input; see Figs. 65 – 67, and the nonlinear aeroelastic response of the structure to this kind of excitation is studied in the following section.

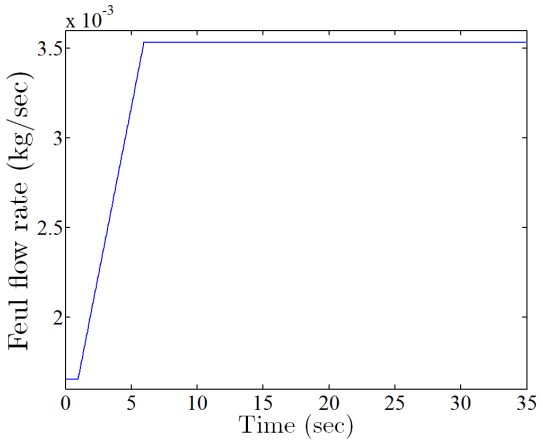

Figure 64: Fuel flow rate profile for ramp excitation

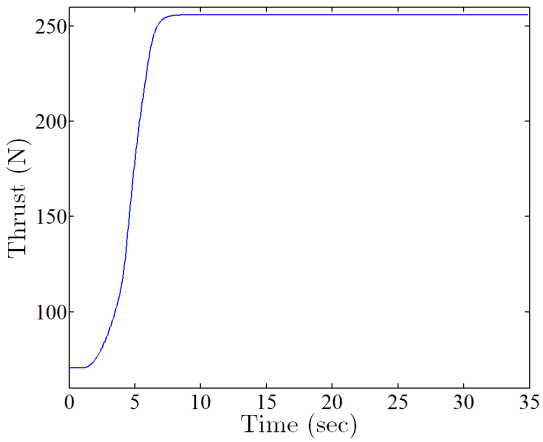

Figure 65: JetCat SP5 engine thrust simulation for ramp fuel profile

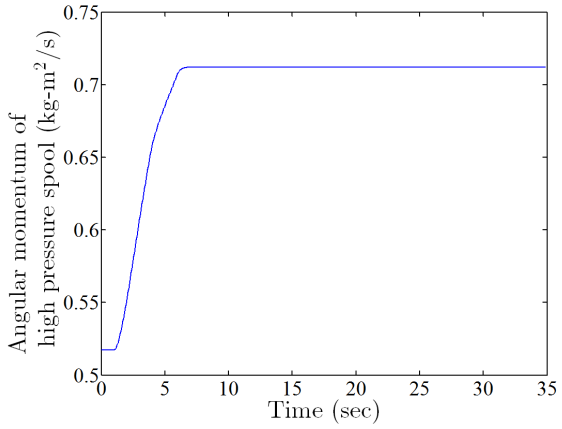

Figure 66: JetCat SP5 engine high pressure angular momentum simulation for ramp fuel profile

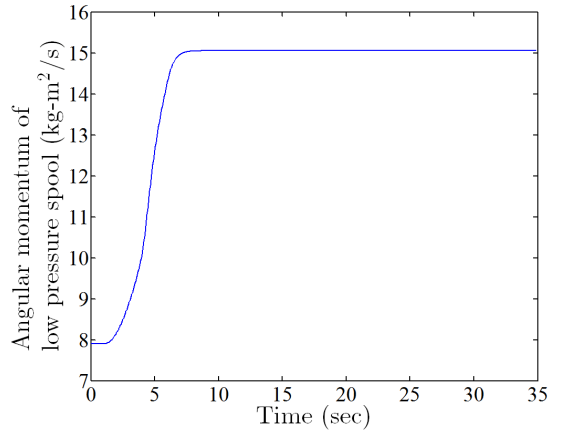

Figure 67: JetCat SP5 engine low pressure angular momentum simulation for ramp fuel profile

Stability analysis while engine operates at cruise condition is explained in section 5.6.1.

– *25% span:* The time march results show that engine placement at this location is stable.

– *50% span:* The time march results show that engine placement at $r = 1$, $\psi = 90°$ and 135 ° lead to stable limit cycle oscillation and excitations for other engine placements at this location do not affect stability of the wing.

– *75% span:* At $r = 1$ and $\psi = 45°$, at subcritical, the excitations lead to oscillations with growing amplitude; see Figs. 68 – 70, and at $\psi = 45°$ and 180°, at supercritical it leads to stable LCO. For engine placement at $r = 1$ and $\psi = 135°$, at supercritical regime, excitation introduces

chaotic oscillations to the structure; see Fig. 71 – 76, and all other engine placements are unaffected by this excitation other than a change in static deflection.

– *100% span:* Effect of this excitation at this location leads to a very large amplitude oscillation and for the case of $r = 1$, $\psi = 180°$ the large amplitude oscillation is a stable LCO.

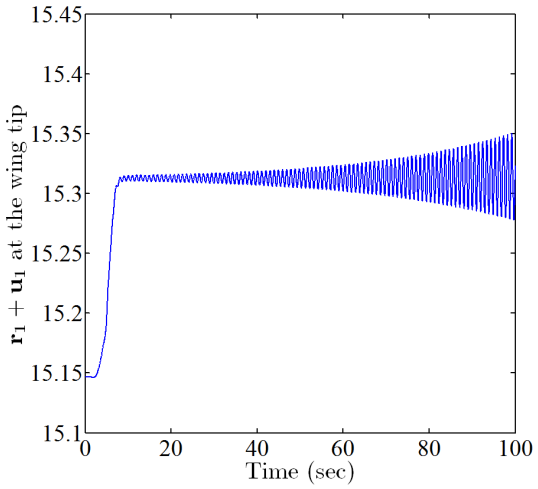

Figure 68: Wing tip position along $\mathbf{b_1}$ vs. time, for engine placement at 100% span with $r = 1$ and ψ= 45°

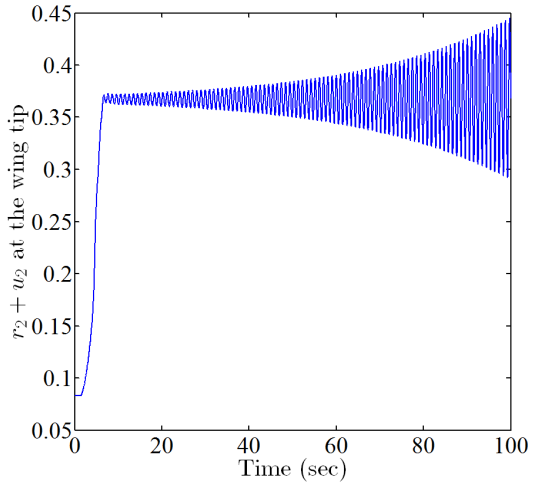

Figure 69: Wing tip position along $\mathbf{b_2}$ vs. time, for engine placement at 100% span with $r = 1$ and ψ= 45°

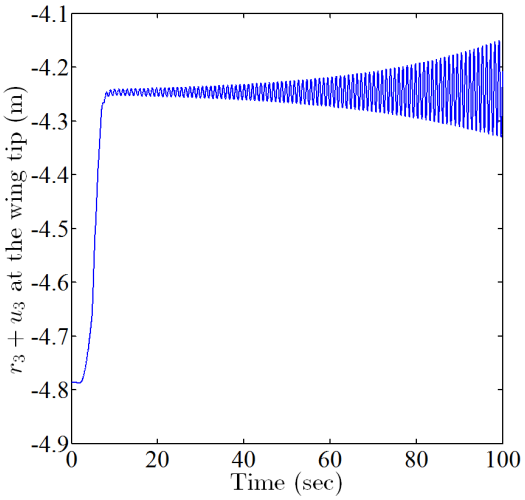

Figure 70: Wing tip position along $\mathbf{b_3}$ vs. time, for engine placement at 100% span with $r = 1$ and $\psi = 45°$

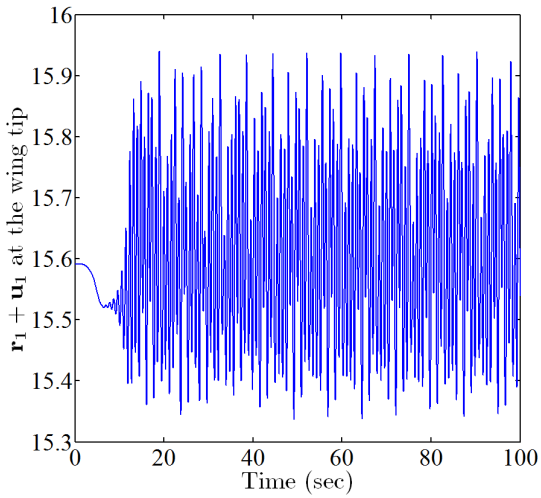

Figure 71: Wing tip position along $\mathbf{b_1}$ vs. time, for engine placement at 100% span with $r = 1$ and $\psi = 135°$

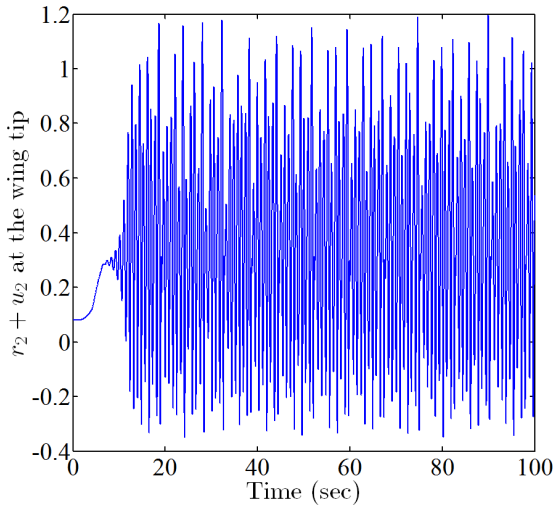

Figure 72: Wing tip position along $\mathbf{b_2}$ vs. time, for engine placement at 100% span with $r = 1$ and $\psi = 135°$

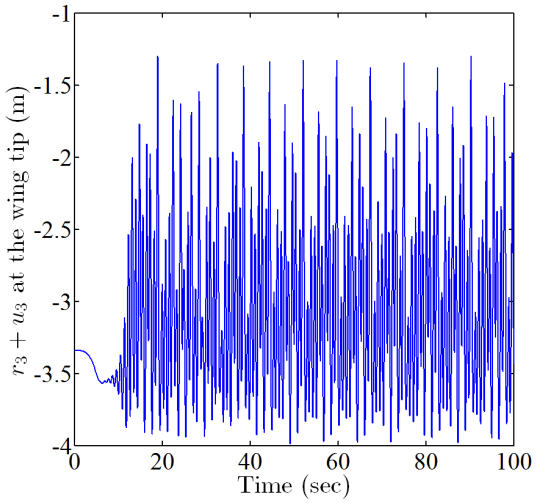

Figure 73: Wing tip position along $\mathbf{b_3}$ vs. time, for engine placement at 100% span with $r = 1$ and $\psi = 135°$

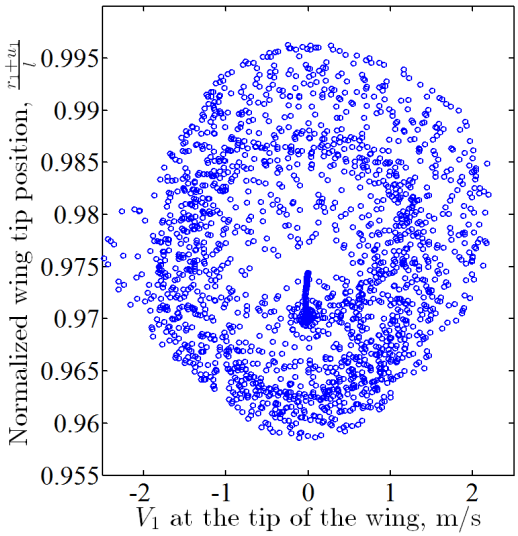

Figure 74: Normalized wing tip position vs. velocity in $\mathbf{b_1}$ direction, for engine placement at 50% span with $r = 1$ and $\psi = 135°$

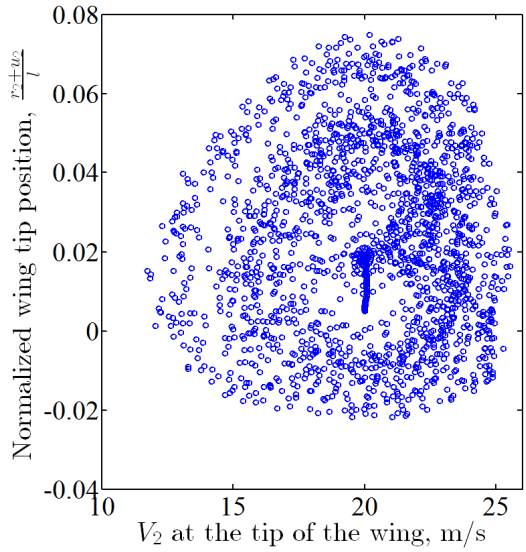

Figure 75: Normalized wing tip position vs. velocity in $\mathbf{b_2}$ direction, for engine placement at 50% span with $r = 1$ and $\psi = 135°$

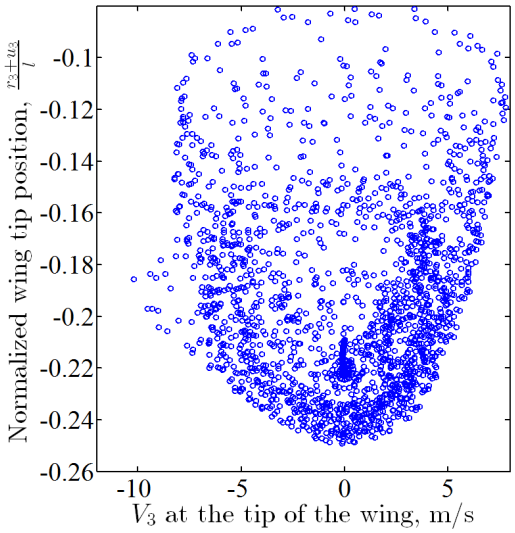

Figure 76: Normalized wing tip position vs. velocity in $\mathbf{b_3}$ direction, for engine placement at 50% span with $r = 1$ and $\psi = 135°$

5.7 Epilogue

Effects of engine placement on flutter characteristics of a very flexible high-aspect-ratio wing are investigated using the code NATASHA. Gravity for this class of wings plays an important role in flutter characteristics. In the absence of aerodynamic and gravitational forces and without an engine, the kinetic energy of the first two modes are calculated. Maximum and minimum flutter speed locations coincide with the area of minimum and maximum kinetic energy of the second bending and torsion modes. Time-dependent dynamic behavior of a turboshaft engine (JetCat SP5) is simulated with a transient engine model and the nonlinear aeroelastic response of the wing to the engine's time-dependent thrust and dynamic excitation is presented. At subcritical regime, at the wing tip and behind the elastic axis, the impulse engine excitation leads to a stable limit cycle oscillation; and for the ramp kind of excitation, in supercritical regime, at 75% span, behind the elastic axis, it produces chaotic oscillation in the wing. Both the excitations at supercritical are stabilized, on the inboard portion of the wing.

Chapter VI

EFFECT OF ENGINE PLACEMENT ON NONLINEAR AEROELASTIC TRIM AND STABILITY OF FLYING WING AIRCRAFT

[1]

6.1 Case study: two-engine flying wing aircraft

The geometry of the flying wing studied in this thesis resembles the HORTEN IV[38, 59]; see Fig. 77. It was modeled using 70 elements. Each wing linearly tapers with 30 elements; and the middle part of the aircraft, which accommodates a hypothetical pilot or cargo, was modeled using 10 elements and a lumped mass whose center lies in the plane of symmetry of the aircraft. Two engines with varying placement along the span, and a set of flaps distributed on the wings comprise the main components of the aircraft control system. As shown in Fig. 77 (and Fig. 78 below), η is the dimensionless length in the $\mathbf{b}_1$ direction, along which the engine is located. The model properties vary linearly from the root to the tip of each wing, and the middle portion of the aircraft is treated as a rigid body with constant aerodynamic and inertia properties equal to those at the wing root. For a flight condition at sea-level, the properties were tuned such that the aircraft experiences body-freedom-flutter with the frequencies close to those of the body-freedom flutter frequency obtained from interviews with HORTEN IV pilots[59]; see Tables 9, 8 and 6 in the appendix.

[1] The content of this chapter is based on a journal article accepted for publication by *Journal of Aircraft.*

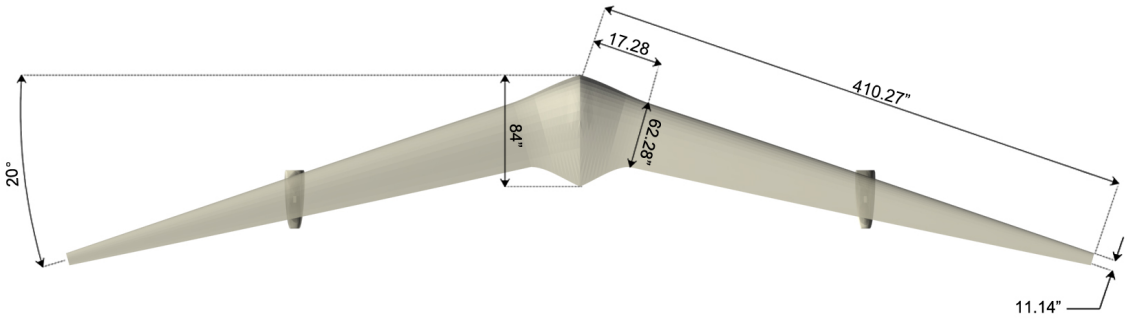

Figure 77: Geometry of the flying wing

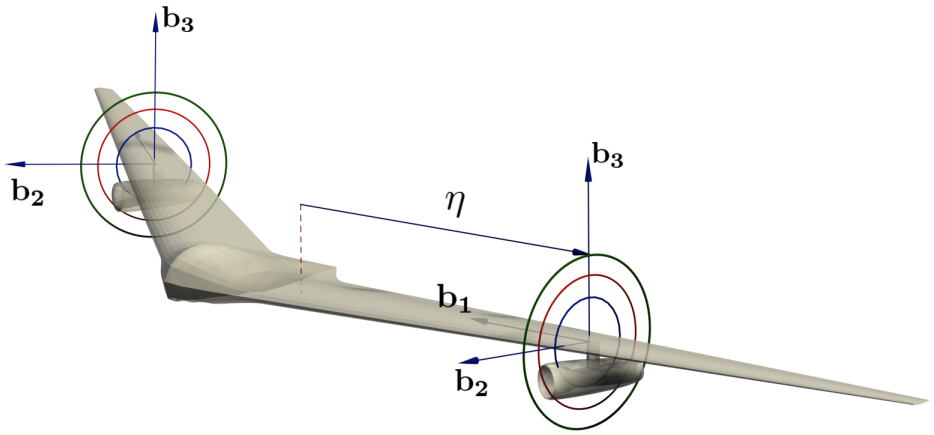

Figure 78: Schematic view of the two-engine flying wing

6.2 Body freedom flutter characteristics

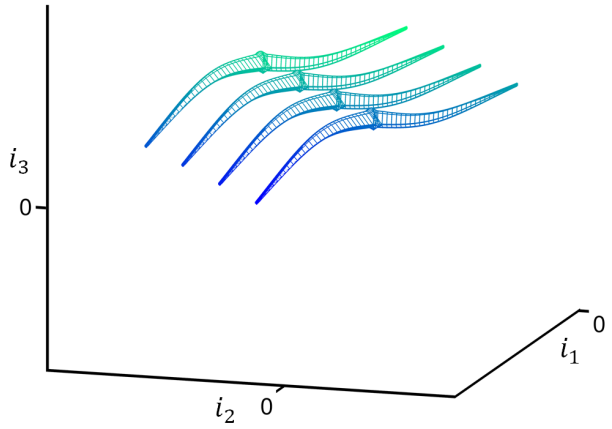

Figure 79: Non-oscillatory yawing mode shape of the flying wing

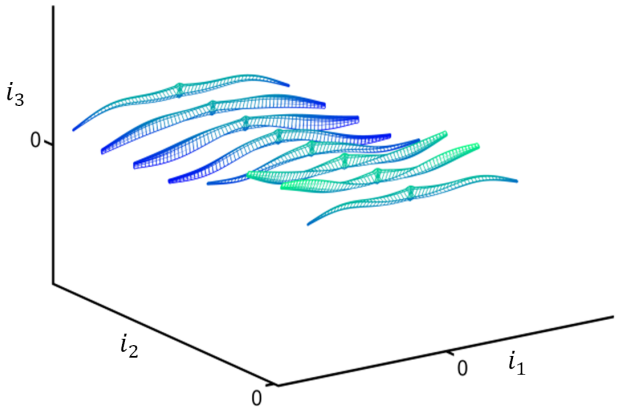

Figure 80: Body freedom flutter mode shape of the flying wing

The Flutter analysis showed that this aircraft experienced body-freedom flutter at 85.5 MPH with 2.9 Hz. The flutter analysis for the aircraft with clean wings (i.e. $\eta = 0$) exhibits a real eigenvalue (indicative of a static instability) of 0.0514 rad/sec at all speeds that involve rotation of aircraft in the horizontal plane, which is associated with flight dynamics and is a non-oscillatory yawing instability; see Fig. 79. There is also an unstable aeroelastic mode that involves the symmetric first elastic bending and torsion modes coupled with the aircraft short-period mode with a frequency of approximately 2.9 Hz, which is a so-called body-freedom flutter mode; see Figs. 80 - 86. This mode becomes unstable at 85.5 MPH, at which speed the flap deflection is -2.15° and the thrust is

10.96 lb. The latter flutter results were normalized using these results and cross-sectional dimension was normalized using the average semi-chord value of 18.36 inches. NATASHA captures another symmetric bending mode with an eigenvalue with a small imaginary part that is right on the stability boundary (-0.0003±0.5i rad/sec). This mode becomes most apparent when the engines are offset farthest from the elastic axis and at the wingtips.

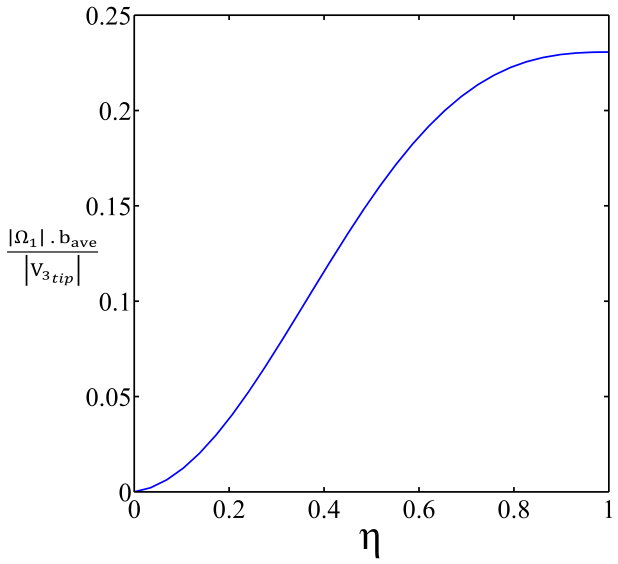

Figure 81: Normalized angular velocity of the body-freedom flutter mode in $\mathbf{B_1}$ direction

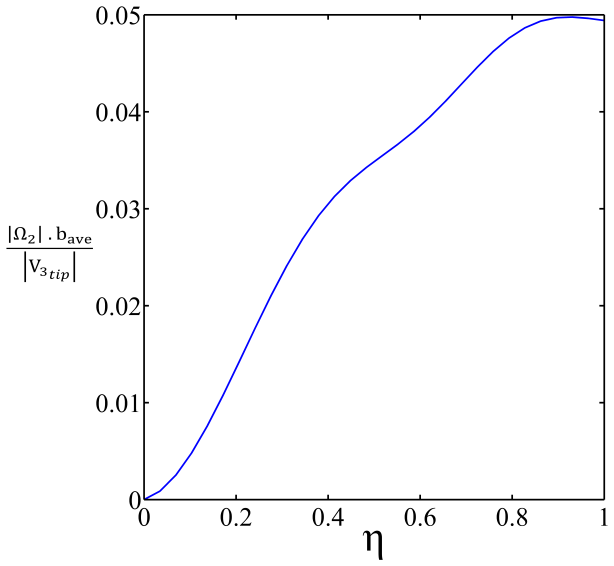

Figure 82: Normalized angular velocity of the body-freedom flutter mode in $\mathbf{B_2}$ direction

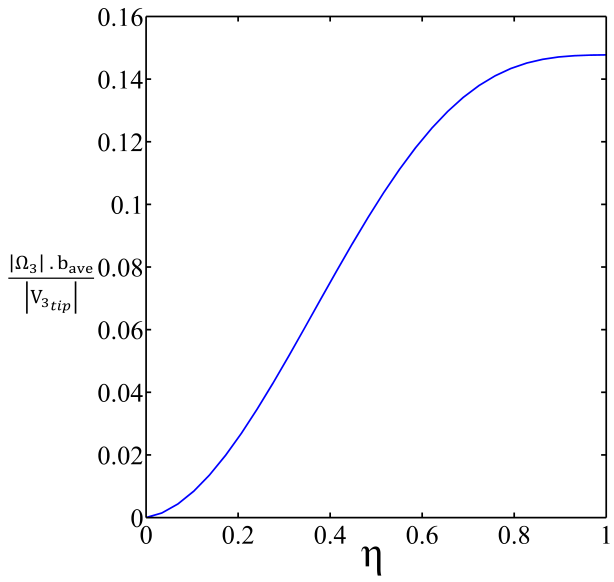

Figure 83: Normalized angular velocity of the body-freedom flutter mode in $\mathbf{B_3}$ direction

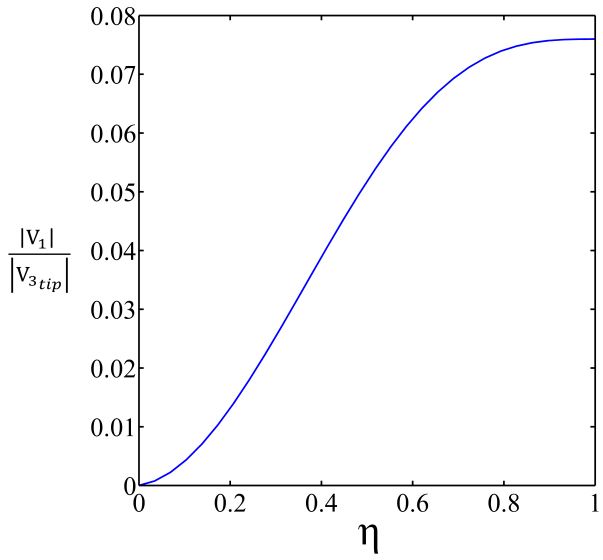

Figure 84: Normalized velocity of the body-freedom flutter mode in $\mathbf{B_1}$ direction

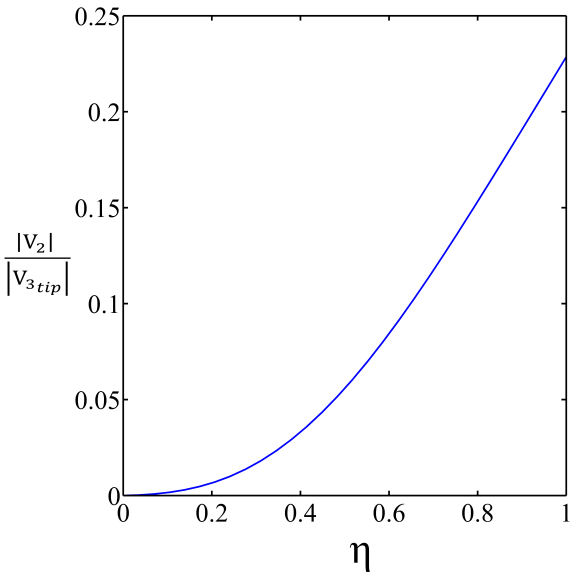

Figure 85: Normalized velocity of the body-freedom flutter mode in $\mathbf{B_2}$ direction

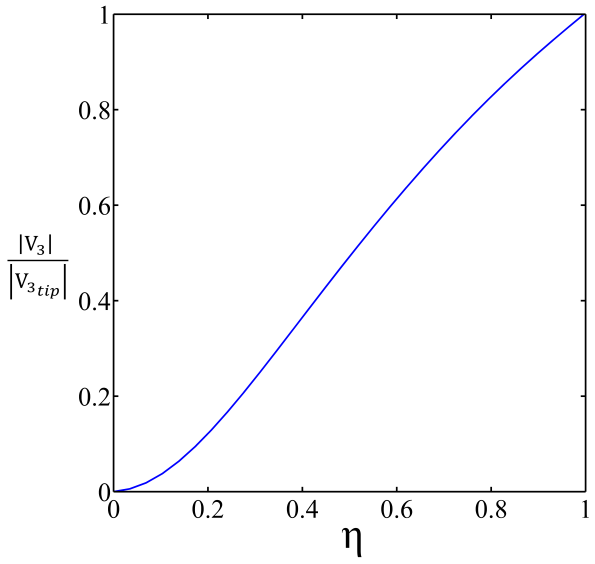

Figure 86: Normalized velocity of the body-freedom flutter mode in $\mathbf{B_3}$ direction

6.3 Minimum kinetic energy region and flutter characteristics

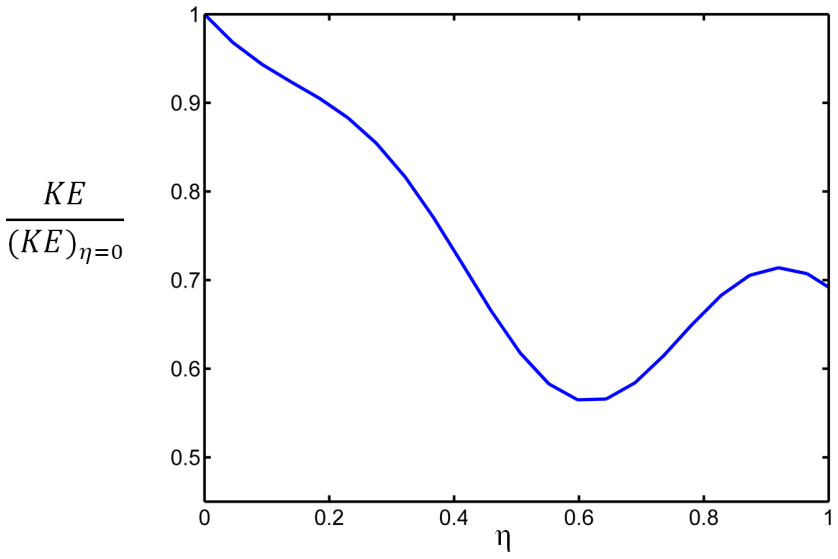

Figure 87: Normalized kinetic energy of the free-free mode of the flying wing

In the absence of engines and aerodynamic and gravitational forces NATASHA is used to analyze the mode shapes and the natural frequencies of the aircraft. The important aspect of this analysis is that one finds the region where the kinetic energy reaches its minimum for the lowest frequency symmetric

elastic free-free bending mode. The nodes in this region are termed as the minimum kinetic energy nodes and, as shown later in this study, may represent ideal locations to place engines. Coupling between bending and torsion modes is a common effect in swept composite wings[42]. Figure 87 depicts the kinetic energy distribution of the symmetric free-free mode of the bare wing for the case study presented in section 6.1. One can see that the point of the minimum kinetic energy is just outboard of 60% span. As expected the absence of engines increases the frequency of that mode.

6.4 Effect of aft sweep on flutter characteristics of the flying wing

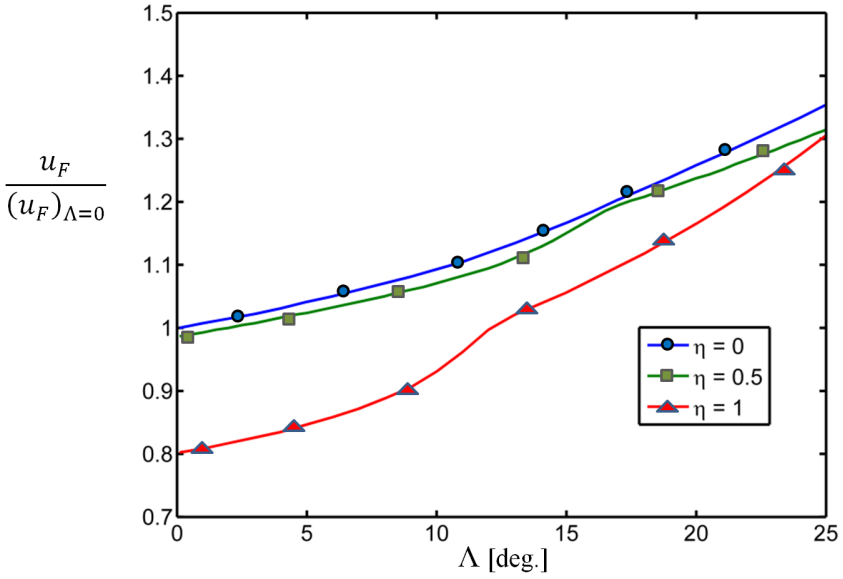

Figure 88: Flutter speed vs. sweep angle for the flying wing

The effect of aft sweep for the flying wing with engines at root, middle and tip of the wing with zero offset from the elastic axis is presented in Fig. 88. Flutter speeds were normalized using the flutter speed of the unswept wing without an engine, which was 67.8 miles/hour. As is known, aft sweep generally increases flutter speed [12, 58, 55, 56, 46, 8].

6.5 Effects of engine placement on nonlinear trim and stability of flying wing aircraft

Two identical engines with known mass, moments of inertia, and angular momentum were symmetrically moved along the span, i.e., in the $\mathbf{b}_1$ direction; and the engine mounts were displaced with

an offset from the elastic axis in the plane of the wing cross section, i.e. $\mathbf{b}_2, \mathbf{b}_3$, while orientations of the engines were maintained; see Fig. 78.

Figure 89, is a representative result of engine placement along the span with two cases of engine offsets from the elastic axis. The first case, when the engines are placed along the span with no offset from the elastic axis, shows a significant increase in flutter speed as the engines are placed between 50% to 70% span. The second case is for engine placement along the span while the offset is forward from the elastic axis up to the order of the mean semi-chord. Similar to the first case, a significant increase in flutter speed is observed when engines are placed between 40% to 80% span. These results are in good agreement with the result presented in the book by Y. C. Fung [32]. In both cases, the flutter speed increase at the area of minimum kinetic energy density and decreases as the engines are placed at the wing tip. Flutter speed experiences small fluctuation when the engines are placed at the inner portion of the wing. To further investigate the area where the flutter speed reaches its maximum and minimum, contour plots of flutter speed for these areas are presented.

Figure 90 is the contour of flutter speed where the maximum flutter speeds occurs, at $\eta = 0.65$. These results show that as the engines are placed forward of the elastic axis the flutter speed increases by a factor of two while the flutter mode is unaffected by this change; see Fig. 91. Examination of the eigenvectors has shown that the flutter mode shape is also unaffected. By further investigations of the flutter results, one sees that flutter speed drops when the engines are placed at the tip of the wings, i.e., where $\eta = 1$. In contrast with the location where the maximum flutter speed is reported ($\eta = 0.65$), a higher flutter speed is attained at this location while the engines are moved aft and above the elastic axis; see Fig. 92. This is caused by a nose-down pitching moment induced by the engines at the tip of the wings. Stability analysis shows that the unstable mode and its frequency are unaffected for the locations at which higher flutter speeds were captured; but for the region where lower flutter speeds are reported, the flutter frequency dramatically increases. This increase is mostly for the engine placements aft and close to the elastic axis; see Fig. 93.

At $\eta = 0.65$, for engine placement forward of the elastic axis, the flap deflection counteracts the nose-up pitching moment induced by the engines thrust; see Fig. 94. NATASHA trims the aircraft

for equality of the lift to the weight and of the drag to the thrust. As flutter speed increases, the aircraft requires more thrust to trim at higher speeds, which leads to higher drag. This effect dramatically increases the thrust; see Fig. 95. It is noteworthy that the thrust follows the same pattern as the flutter speed; see Fig. 90.

Placing the engines at the wing tips one sees that patterns of the control (i.e., flap and thrust) contours at the point where instability occurs have very similar behaviors to those of flutter speed and frequency, respectively; see Figs. 92, 93, 96 and 97. When the engines are at the tip of the wings, forward of and below the elastic axis, flaps play a significant role in trimming the aircraft and counteracting the nose-up moment induced in the wing; see Fig. 96. The trimming moments from the flaps must counteract the moment created by the offset thrust. Figure 96 shows that when the engines are aft and above the elastic axis, flutter speed increases and requires more thrust to trim.

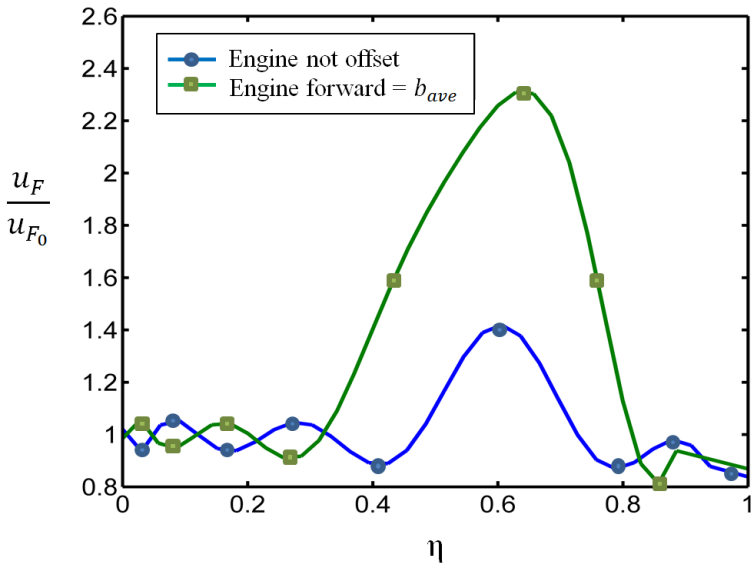

Figure 89: Flutter speed for engine placement along the span for two values of chordwise offset

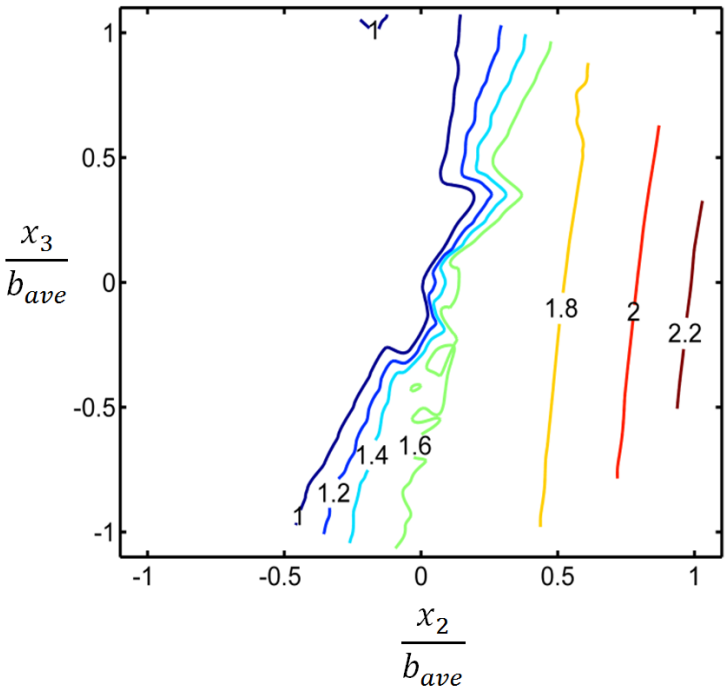

Figure 90: Contour of normalized flutter speed at $\eta = 0.65$

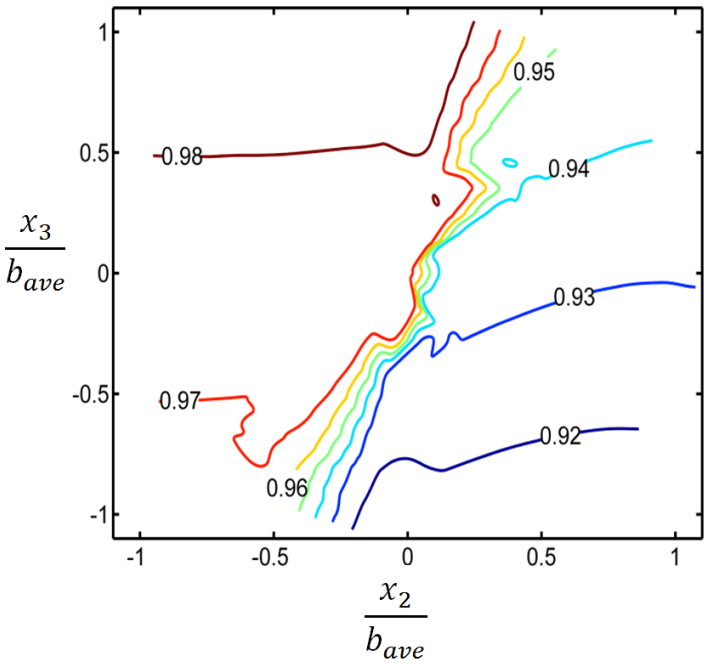

Figure 91: Contour of normalized flutter frequency at $\eta = 0.65$

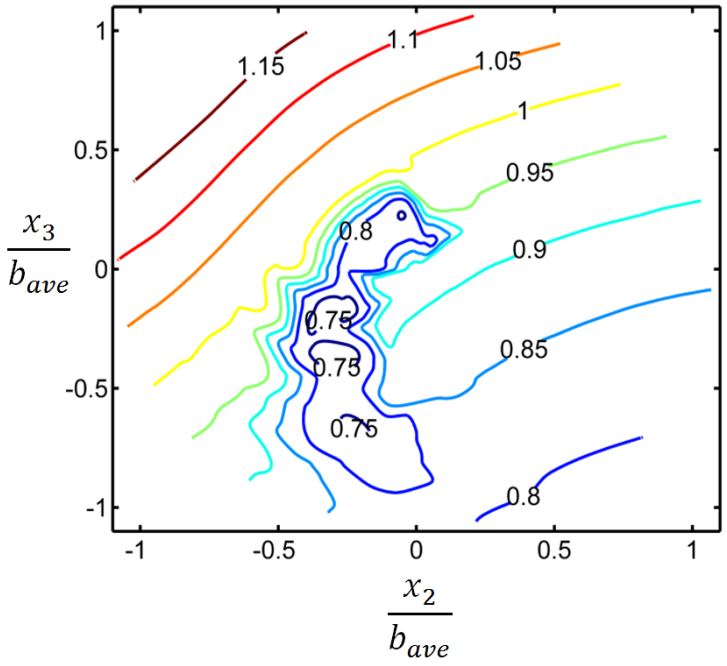

Figure 92: Contour of normalized flutter speed at $\eta = 1$

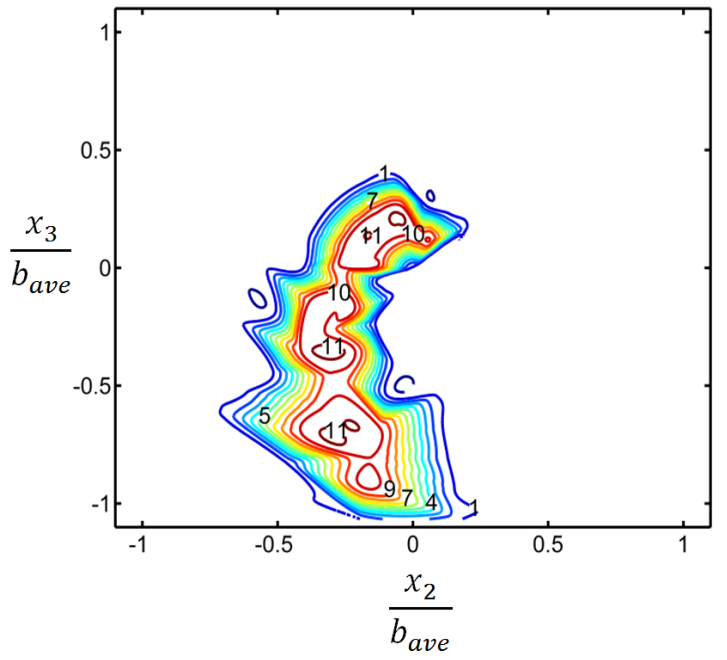

Figure 93: Contour of normalized flutter frequency at $\eta = 1$

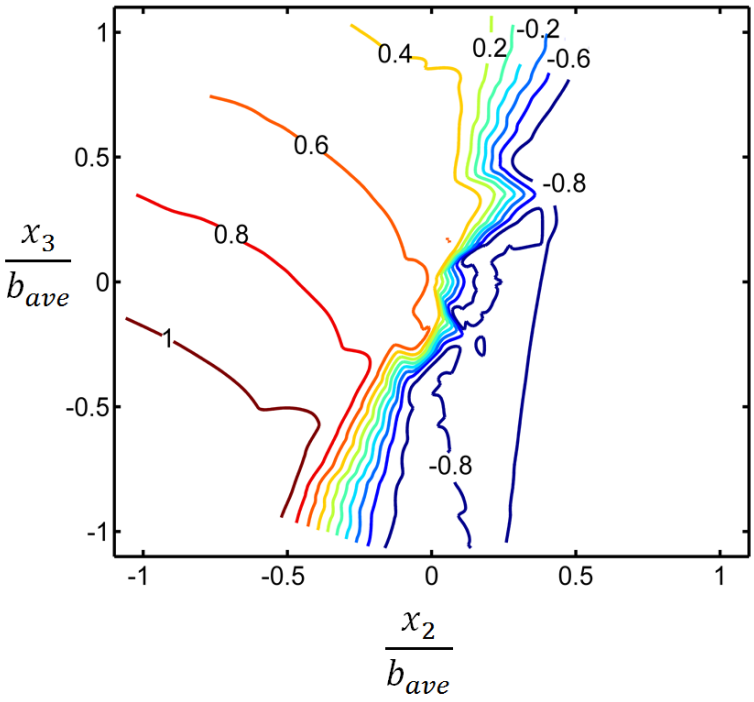

Figure 94: Contour of normalized flap at flutter at $\eta = 0.65$

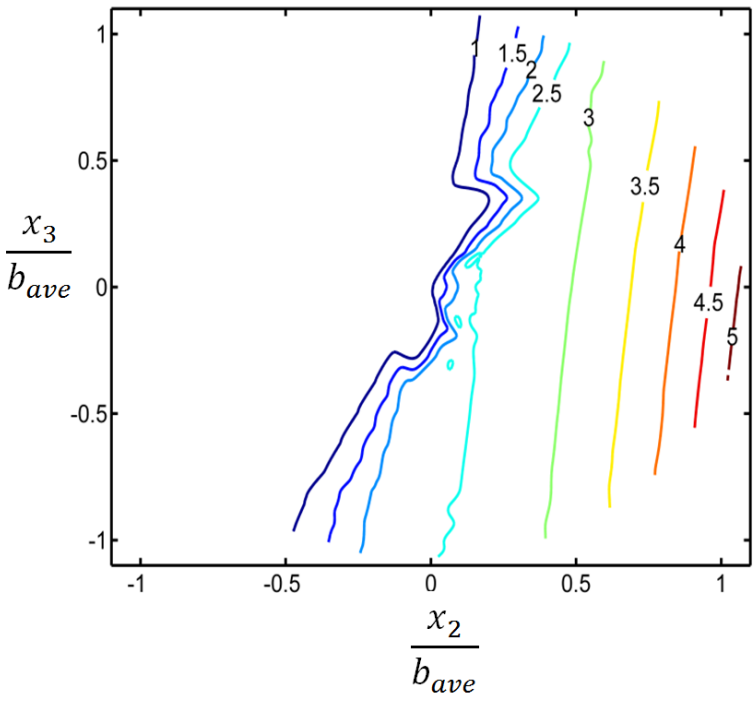

Figure 95: Contour of normalized thrust at flutter at $\eta = 0.65$

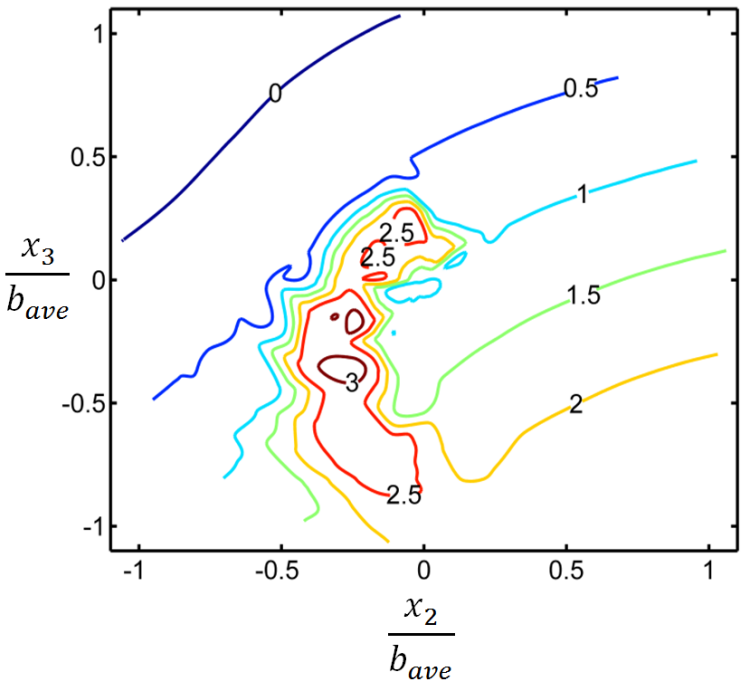

Figure 96: Contour of normalized flap at flutter at $\eta = 1$

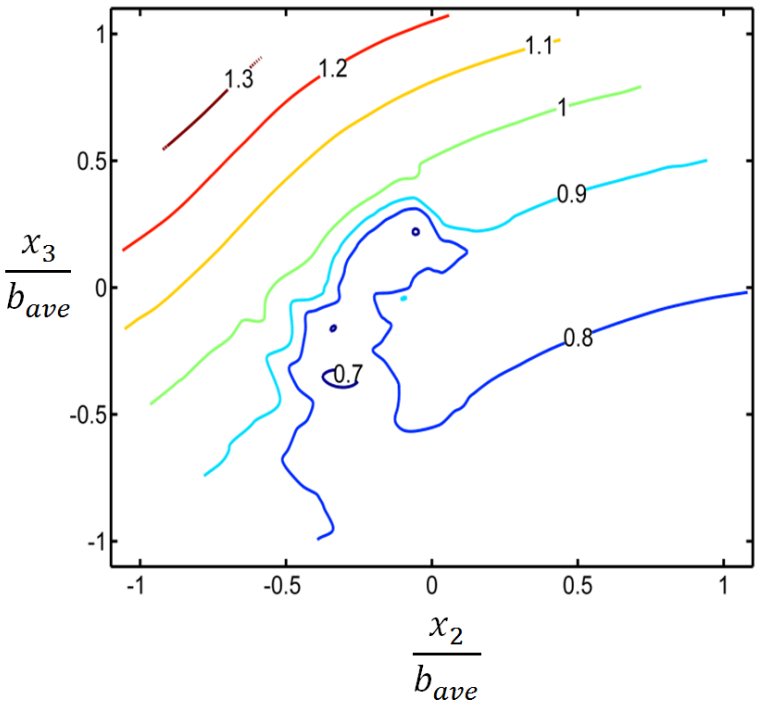

Figure 97: Contour of normalized thrust at flutter at $\eta = 1$

6.6 Effects of engine placement with constant aircraft c.g. location

Placement of engines toward the outboard portion of the wings caused the aircraft center of gravity (c.g.) to migrate aft. This effect was counteracted by the larger response in the aircraft controls (flap and thrust). NATASHA was able to trim the aircraft with larger values of thrust and flap deflections. However, in some cases, especially when the engines were closer to the wing tip, the flap deflections exceeded the range of validity for the aerodynamic model, which requires small flap angles ($\pm 6°$). In order to overcome this problem, a concentrated mass representing the pilot or a piece of equipment was displaced, such that the aircraft center of gravity remained constant at (0, -32.1 , -3.7) inches with respect to the reference point; see Fig. 98. This change not only helped to keep the flap deflections in the linear range, but also smoothed out variations in the flutter speed, increasing it along the span. Figure 99 shows a sample case of this effect where the engines were placed at zero offset from the elastic axis. As shown, this setup is very useful for the case of engines being placed at the tips of the wings. Figure 100 shows the effect of keeping the aircraft c.g. constant on flutter

speed as the engines were displaced in the wings' cross-sectional plane at $\eta = 0.65$. Comparing these results with the ones shown in Fig. 90, one sees that the flutter speed aft and above the elastic axis has increased, while flutter frequencies monotonically decrease as the engines move from aft to forward of the elastic axis; see Fig. 101. Results presented in Fig. 92 showed that flutter speed is at the lowest value with engines at the tips of the wings. Figure 102 shows that keeping the c.g. of the aircraft constant increases the flutter speed in particular for engine placement above the elastic axis. Figure 103 shows that the flutter frequencies stay in the same range, whereas in the previous result flutter frequencies exhibited a large increase; see Fig. 93. Note that keeping the c.g. of a flying wing aircraft fixed can help keep the control settings within linear bounds. This, together with the results presented here, are important factors for placement of the engines in order to achieve good performance and fuel-efficient design.

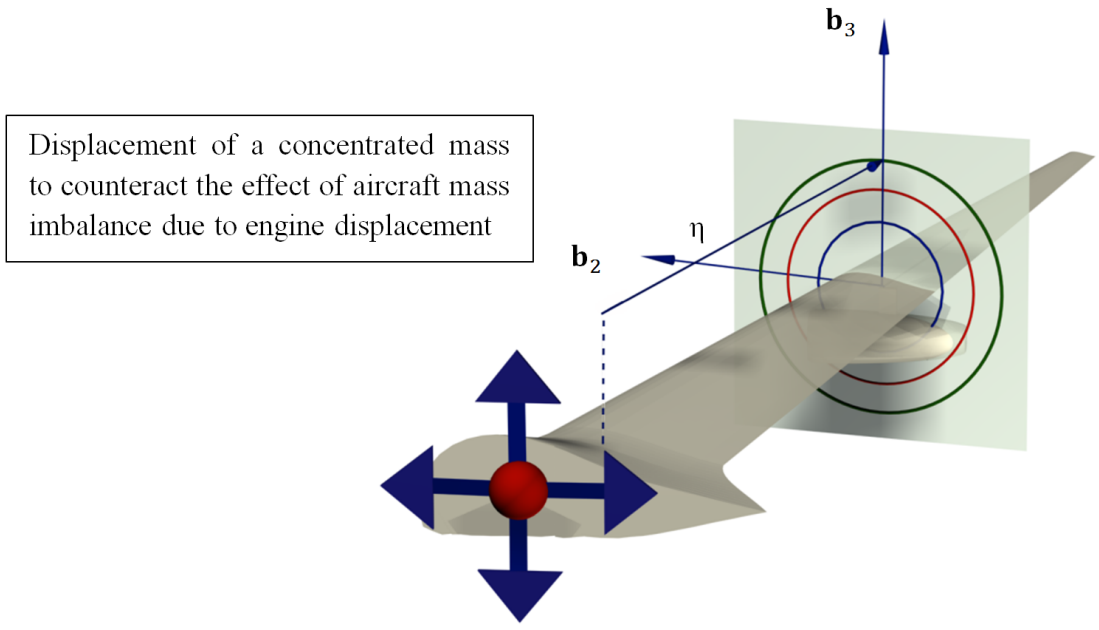

Figure 98: Aircraft mass balance

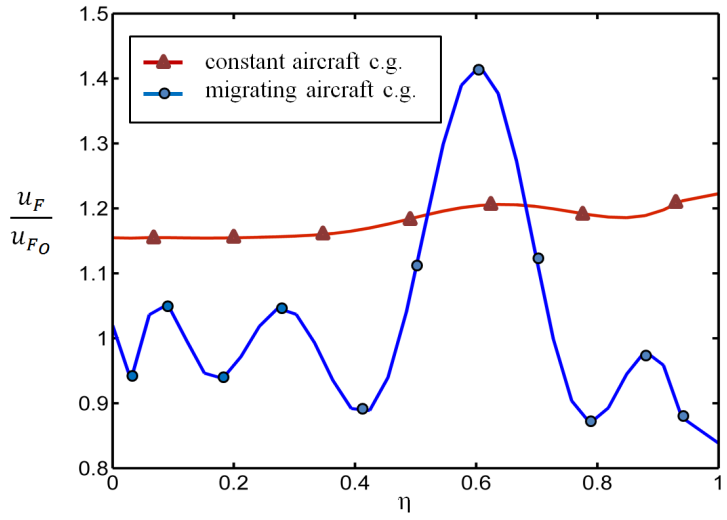

Figure 99: Effect of engine placement and aircraft center of gravity with zero offset from the elastic axis

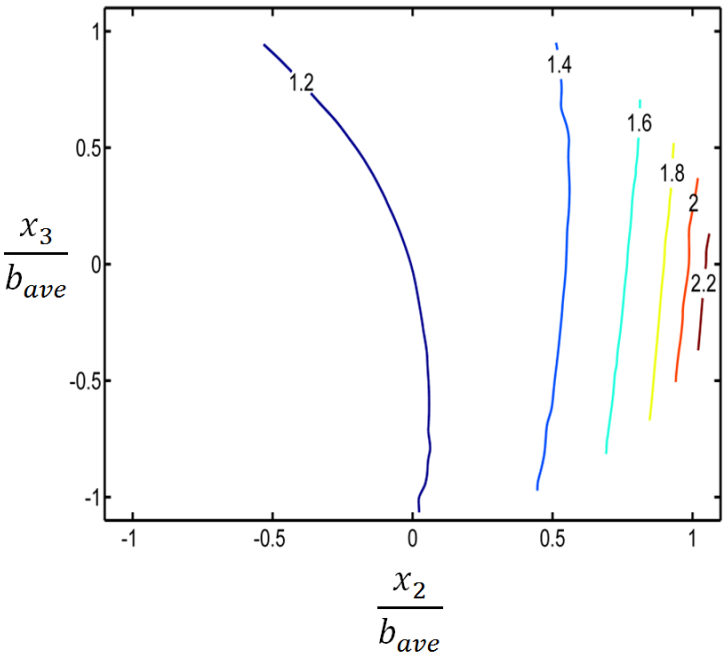

Figure 100: Contour of normalized flutter speed at $\eta = 0.65$, keeping aircraft c.g. constant

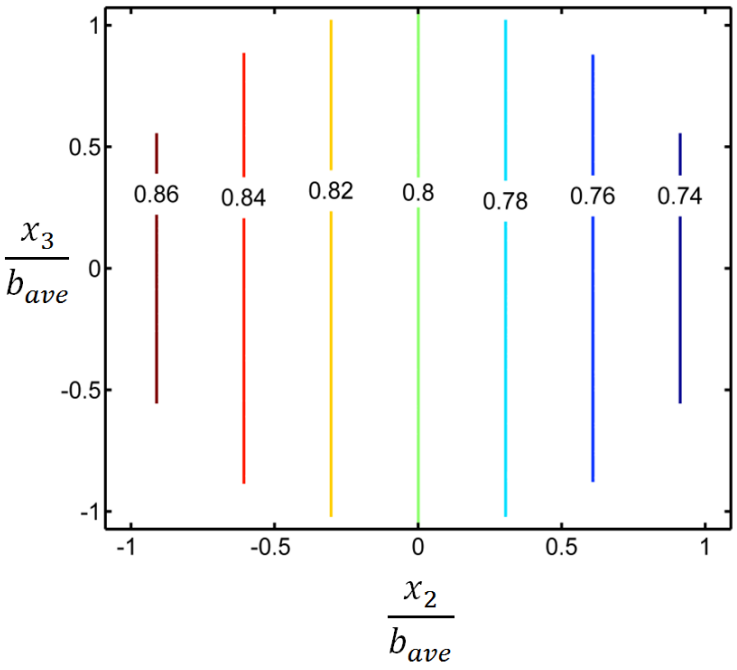

Figure 101: Contour of normalized flutter frequency at $\eta = 0.65$, keeping aircraft c.g. constant

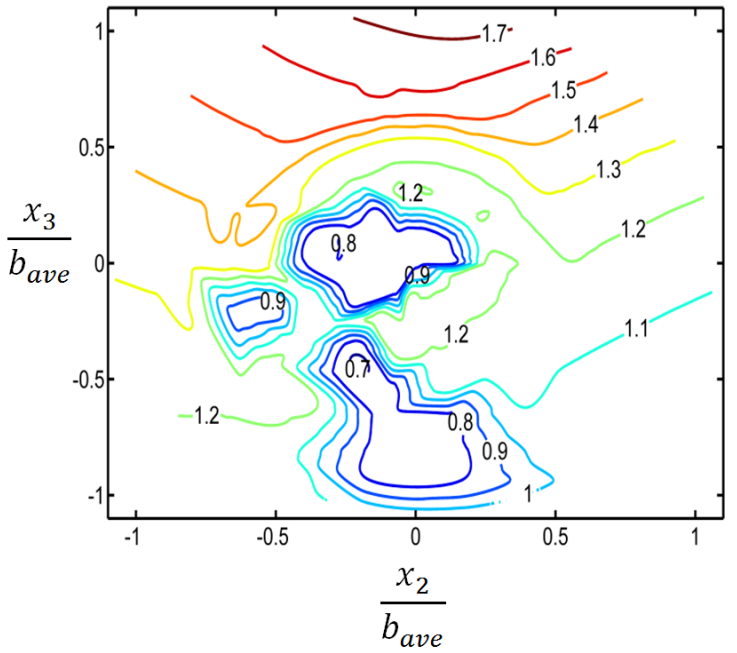

Figure 102: Contour of normalized flutter speed at $\eta = 1$, keeping aircraft c.g. constant

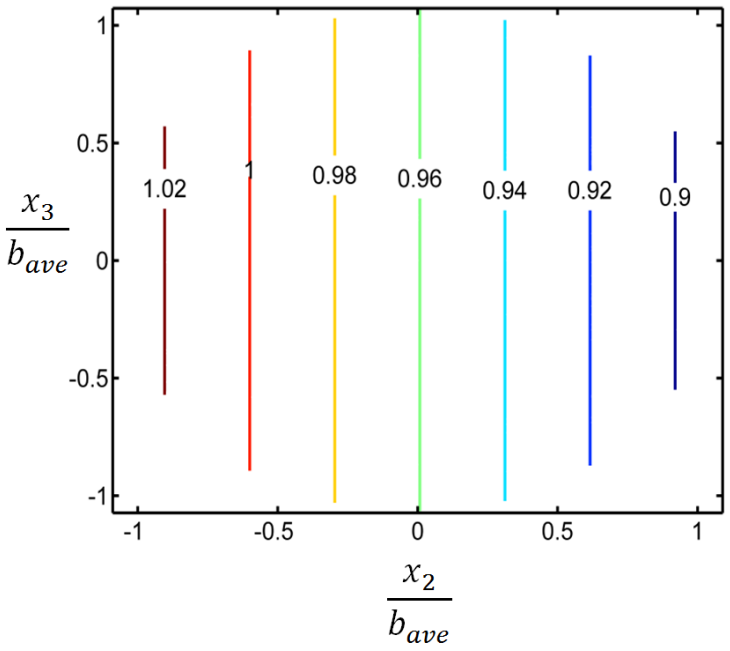

Figure 103: Contour of normalized flutter frequency at $\eta = 1$, keeping aircraft c.g. constant

6.7 Epilogue

Effects of engine placement and sweep on flutter characteristics of an aft-swept flying wing resembling the Horten IV are investigated using NATASHA. This aircraft exhibits a non-oscillatory yawing instability, expected in aircraft with neither a vertical tail nor yaw control. More important, however, is the presence of a low frequency "body-freedom flutter" mode. The aircraft center of gravity was held fixed during the study, which allowed aircraft controls to trim similarly for each engine location, and minimized flutter speed variations along the inboard span. Maximum flutter speed occurred for engine placement just outboard of 60% span with engine center of gravity forward of the elastic axis. The body-freedom flutter mode was largely unaffected by the engine placement except for cases in which the engine is placed at the wing tip and near the elastic axis. In the absence of engines, aerodynamics, and gravity, a region of minimum kinetic energy density for the first symmetric free-free bending mode is also near the 60% span. A possible relationship between the favorable flutter characteristics obtained by placing the engines at that point and the region of minimum kinetic energy is briefly explored.

Chapter VII

EFFECT OF MULTIPLE ENGINE PLACEMENT ON AEROELASTIC TRIM AND STABILITY OF FLYING WING AIRCRAFT

[1]

7.1 Case study: four-engine flying wing aircraft

The geometry of the flying wing studied in this section resembles the HORTEN IV as described by [38], [59], and [52]; see Fig. 104. This aircraft is modeled using 45 elements. Each wing is constructed with 19 elements; and the middle part of the aircraft, which accommodates a hypothetical pilot or cargo, is modeled using six elements and a lumped mass whose center lies in the aircraft plane of symmetry. Four engines with varying placement along the span and a set of flaps distributed on the wings comprise the main components of the aircraft flight control system. As shown in Figs. 104 and 118, η_1 and η_2 are the dimensionless distances along $\mathbf{b_1}$, along which the engines are located on the right wing; r_1 and r_2 are radial offsets of the engines from the elastic axis, normalized by the maximum radial offset from the elastic axis, $r_{\text{nominal}} = 0.3$ meters; ψ_1 and ψ_2 are the polar angles, with $\psi_n = 0$ ($n = 1,\ 2$) pointing upstream. As the engines were placed further outboard along the span, the aircraft c.g. migrated aft. In order to counteract this effect, the concentrated mass in the aircraft plane of symmetry was displaced such that the c.g. was held constant at (0, -1, -0.1) meters with respect to the reference point.

[1] The content of this chapter is based on a journal article accepted for publication with minor revision by *Journal of Fluids and Structures.*

The aerodynamic properties of the wing vary linearly from root to tip; see Table 9 in the Appendix. The model properties vary from root to tip of the wings using these relations:

$$\begin{aligned} \mu &= \mu_{\text{root}} \left(\frac{c}{c_{\text{root}}} \right) & \xi &= \xi_{\text{root}} \left(\frac{c}{c_{\text{root}}} \right) \\ [R] &= [R]_{\text{root}} \left(\frac{c}{c_{\text{root}}} \right) & [S] &= [S]_{\text{root}} \left(\frac{c}{c_{\text{root}}} \right)^2 \\ [I] &= [I]_{\text{root}} \left(\frac{c}{c_{\text{root}}} \right)^3 & [T] &= [T]_{\text{root}} \left(\frac{c}{c_{\text{root}}} \right)^3 \end{aligned} \tag{17}$$

These relationships are derived empirically from the Variational Asymptotic Beam Section (VABS) for sections with different chord lengths; see [18] and [85, 84]. The middle portion of the aircraft is treated as a rigid body with constant aerodynamic and inertia properties equal to those at the wing root. Detailed sectional properties of the wing can be found in Table 8; these properties were tuned such that the aircraft experiences body-freedom-flutter with the frequencies close to those of the body-freedom flutter frequency obtained from HORTEN IV pilots as described by [38], [59], and [52]. See Table 3.

7.2 Effects of engine placement on lift to drag ratio

Lift to drag ratio analysis is done by calculating the ratio of the equivalent forces, namely weight and total thrust. Weight of the aircraft is assumed to be constant, and at constant speed (50 m/s) while the aircraft c.g. was held constant, NATASHA calculated the total thrust for different engine placements along the span, including offsets from elastic axis. In this analysis, for example, the first engine on the right wing is fixed at η_1 with a particular offset from the elastic axis, and the second engine on the right wing is further out along the span but with the same offset from the elastic axis. It was observed that engine placement along the span does not significantly affect L/D of the aircraft; see Figs. 105 – 112. The small variation of L/D can be attributed to the small static deflections of the wings as the engines are moved along the span – not due to considerations of the engine aerodynamics. Figure 113 shows the contour of L/D for varying the offset of the engines from elastic axis while fixing their span wise location; i.e., $\eta_1 = 0.1$ and $\eta_2 = 0.3$. It is shown that the change in L/D is not large.

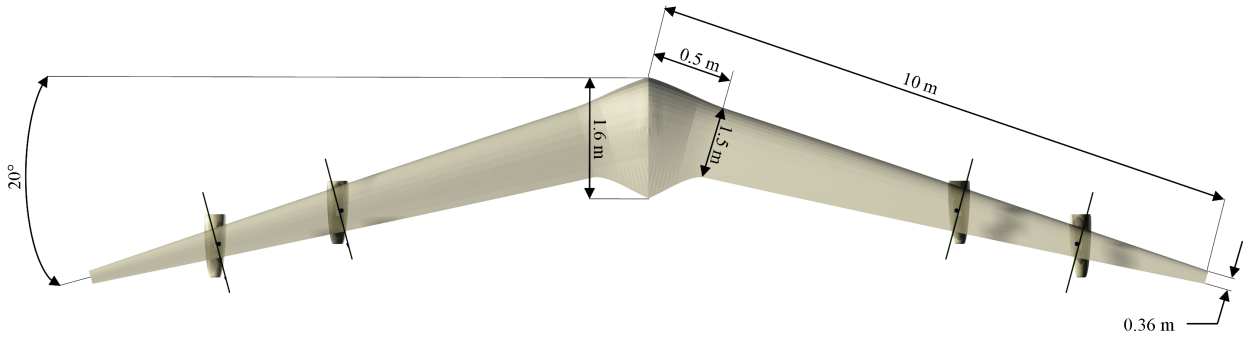

Figure 104: Top view of the flying wing

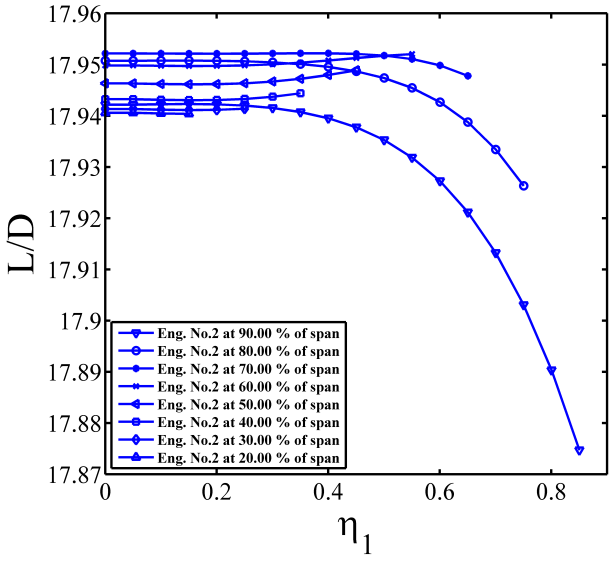

Figure 105: Lift to drag ratio for $r_1 = r_2 = 0.3$ and $\psi_1 = \psi_2 = 0°$

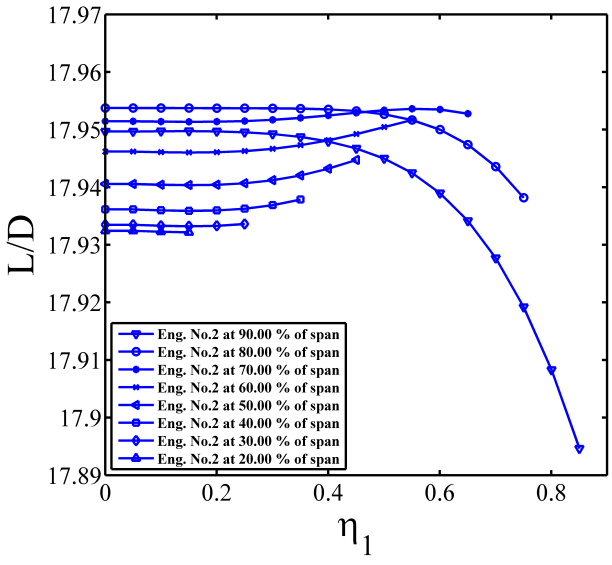

Figure 106: Lift to drag ratio for $r_1 = r_2 = 0.3$ and $\psi_1 = \psi_2 = 45°$

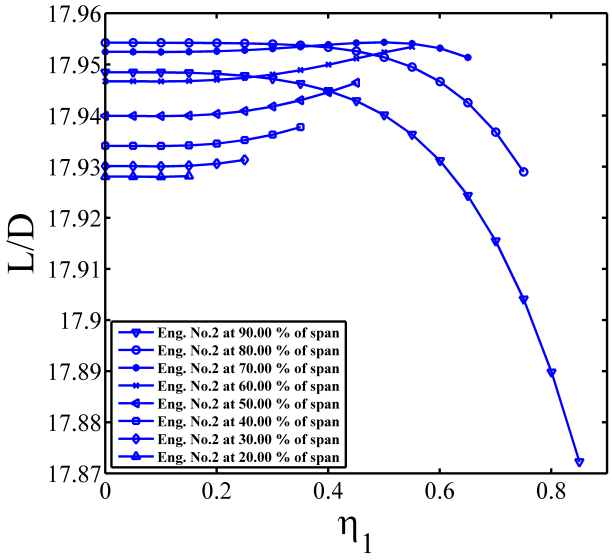

Figure 107: Lift to drag ratio for $r_1 = r_2 = 0.3$ and $\psi_1 = \psi_2 = 90°$

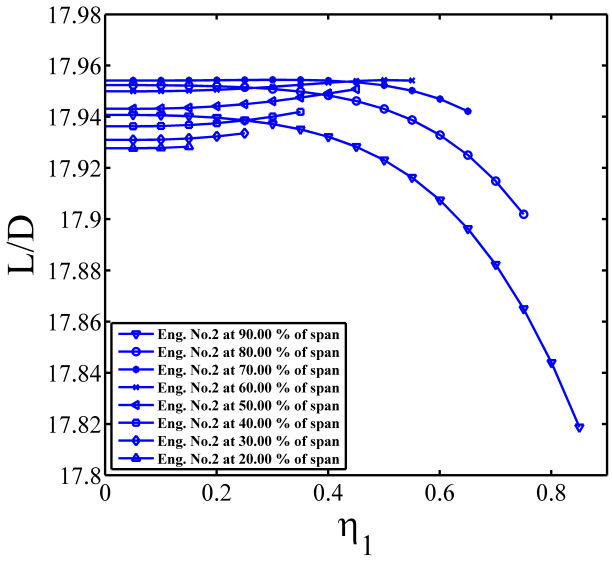

Figure 108: Lift to drag ratio for $r_1 = r_2 = 0.3$ and $\psi_1 = \psi_2 = 135°$

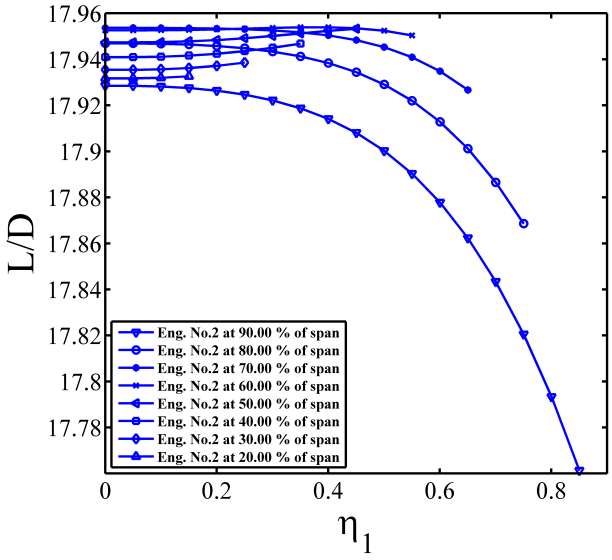

Figure 109: Lift to drag ratio for $r_1 = r_2 = 0.3$ and $\psi_1 = \psi_2 = 180°$

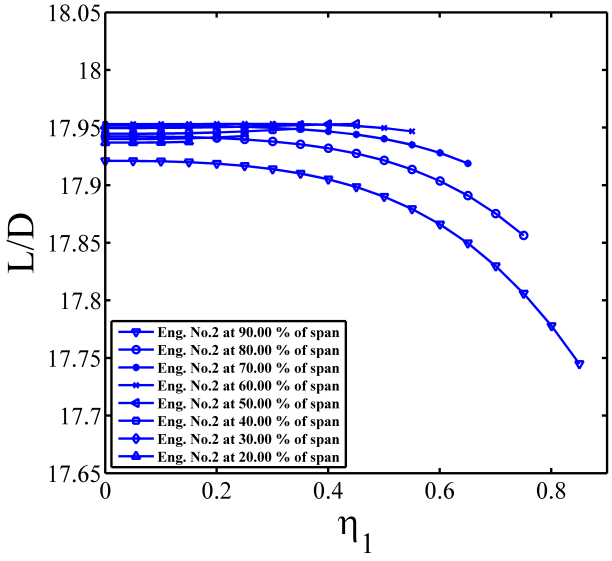

Figure 110: Lift to drag ratio for $r_1 = r_2 = 0.3$ and $\psi_1 = \psi_2 = 225°$

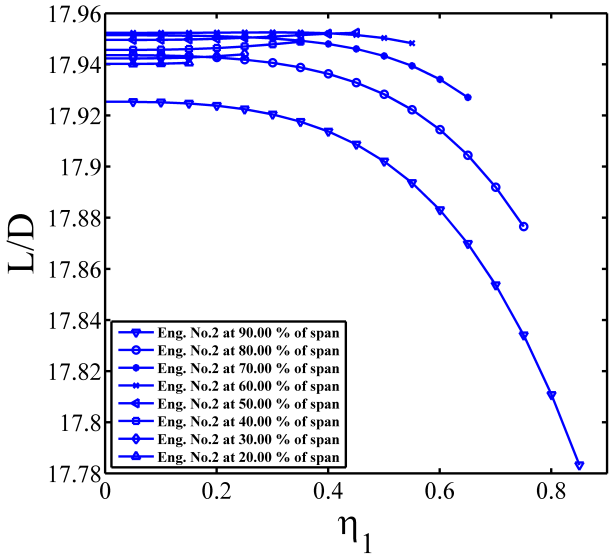

Figure 111: Lift to drag ratio for $r_1 = r_2 = 0.3$ and $\psi_1 = \psi_2 = 270°$

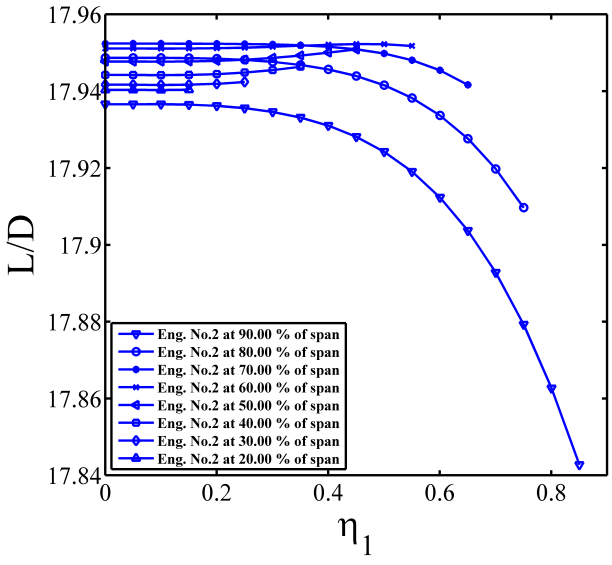

Figure 112: Lift to drag ratio for $r_1 = r_2$= 0.3 and $\psi_1 = \psi_2$= 315°

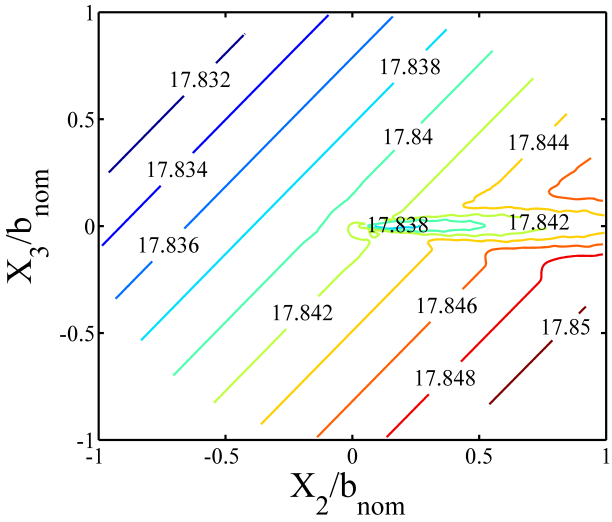

Figure 113: L/D contour for $\eta_1 = 0.1$ and η_2= 0.3

7.3 Body freedom flutter characteristics

The behavior of the sub- and supercritical eigenvalues was studied for two cases of engine placement, both with zero offset from the elastic axis: (a) $\eta_1 = 0$ and $\eta_2 = 0.5$, and (b) η_1=0.6 and η_2=0.9. For the first case, body-freedom flutter occurred at 40.8 m/s with a frequency of 9.560 rad/s while

the first symmetric bending mode of the wings couples with the aircraft short-period mode; see Fig. 115. In the supercritical regime, as the speed increases, the modal damping peaks and then returns to the stable region (a so-called hump mode) and another mode becomes unstable; see Fig. 114. The second case experienced flutter at 88 m/s with frequency 47.12 rad/s. The unstable mode is a mixed motion of in- and out-of-plane bending coupled with torsion and the aircraft short-period mode.

As the engines are placed further outboard, i.e., case (b), the low-frequency oscillatory mode presented in case (a) remains stable; see Fig. 116. Instability occurs at a higher speed (88 m/s). There was no apparent coalescence between the unstable mode of the aircraft and other modes at the point where instability occurred; see Fig. 117. In both cases, NATASHA captured other non-oscillatory unstable roots of flight dynamic origin with very small magnitude. The results at the onset of instability for case (a) are presented in Table 3 and are used for normalization of other results.

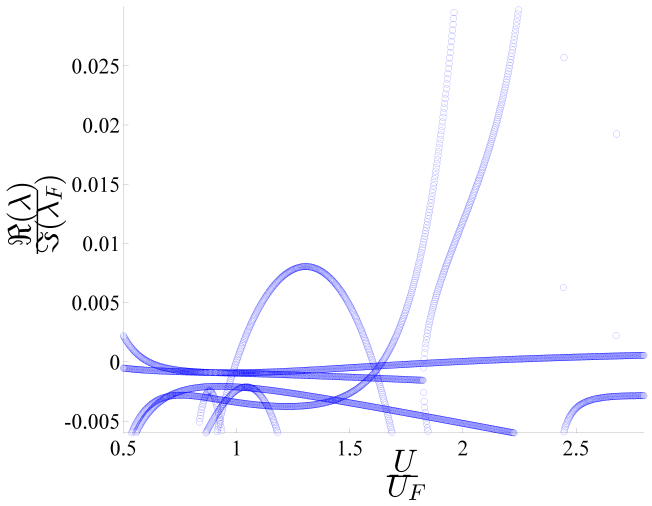

Figure 114: Real part of the eigenvalues for η_1=0 and η_2=0.5

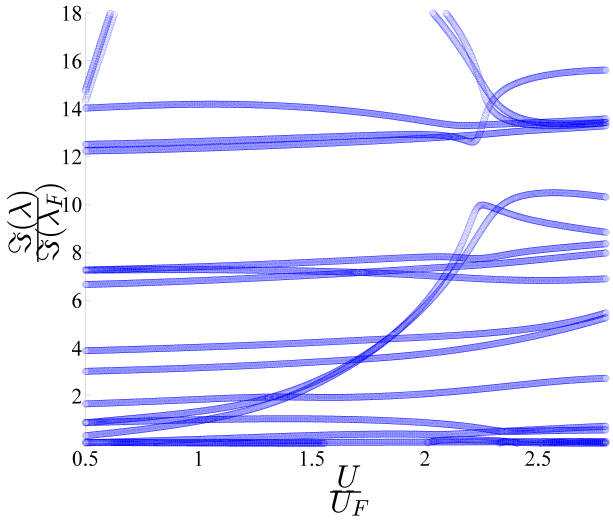

Figure 115: Imaginary part of the eigenvalues for η_1=0 and η_2=0.5

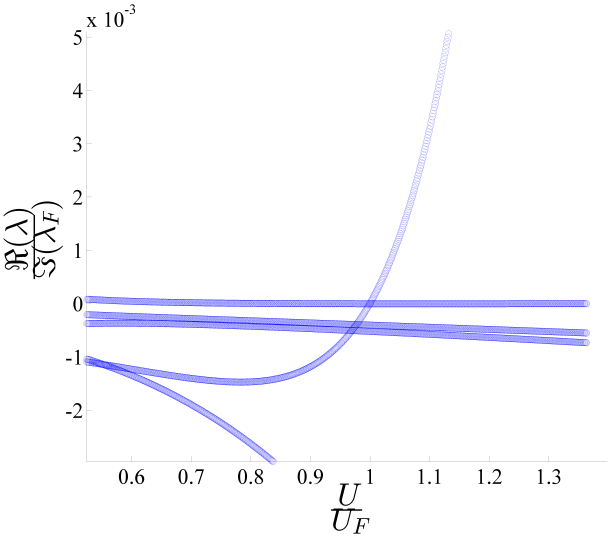

Figure 116: Real part of the eigenvalues for η_1=0.6 and η_2=0.9

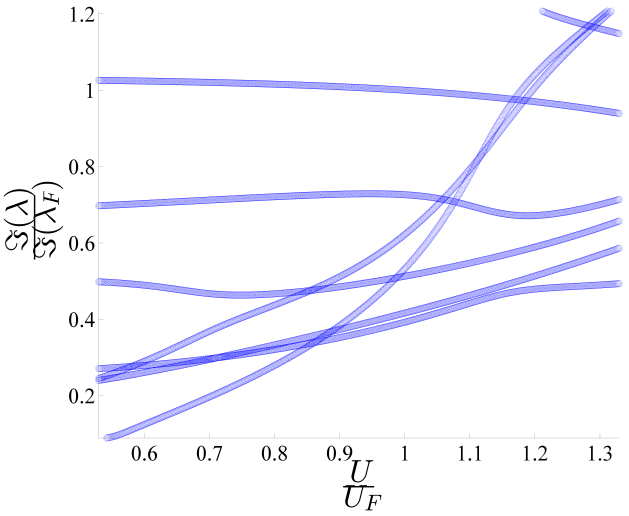

Figure 117: Imaginary part of the eigenvalues for η_1=0.6 and η_2=0.9

Table 3: Flutter characteristics of the base model

Engine locations	Speed (m/s)	Eigenvalues (rad/s)	Thrust (N)	Flap (deg.)
$r_1 = r_2 = \psi_1 = \psi_2 = 0$ η_1=0, η_2=0.5	40.8	0.022 0.0006 ± 9.560i	23.02	1.257

7.4 Effect of multiple engine placement on body freedom flutter

Four identical engines with known mass, moments of inertia, and angular momentum are symmetrically placed along the span (i.e., in the $\mathbf{b_1}$ direction), and the engine mounts are offset from the elastic axis in the plane of the wing cross section (i.e., along $\mathbf{b_2}$ and $\mathbf{b_3}$), while the engine orientations are maintained; see Fig. 118. The engine offsets from the elastic axis are presented in polar coordinates with (r_n, ψ_n) where n is the engine number. Figures 119 – 127 show the variation in flutter speed for different engine placements along the span with different offsets from the elastic axis while one of the engines was kept fixed in a particular location and the other one moves along the span. It is to be noted that the variability of flutter speed with engine location is primarily the result of thrust, angular momentum and inertial properties of the engines rather than aerodynamic effects due to their deformation of the wing.

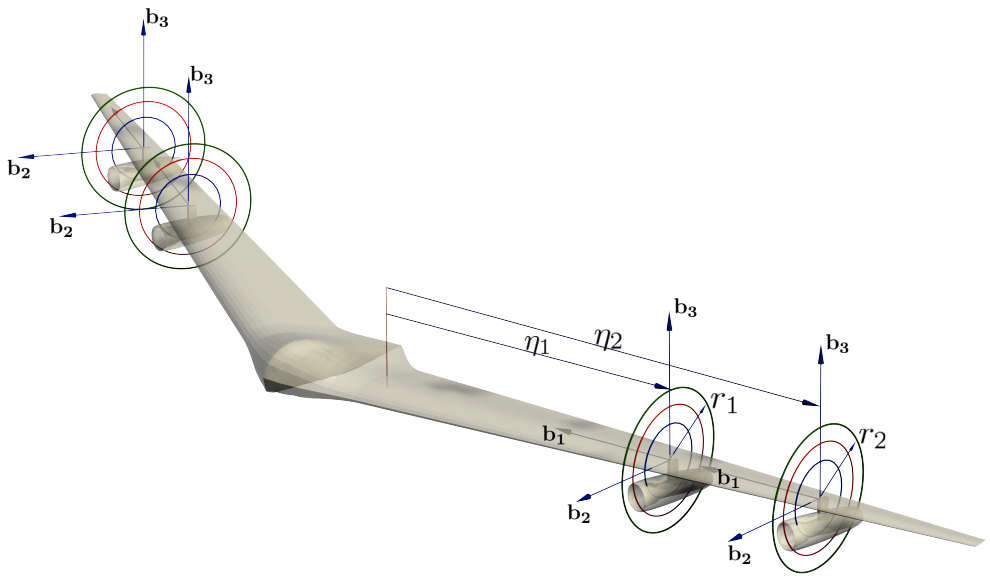

Figure 118: Schematic view of the flying wing

When engines are placed along the span with no offset from the elastic axis, a higher flutter speed is obtained when the second engine is placed at the outer portion of the wing and the first engine is at an area between 50% to 70% span; see Fig. 119. This region continues to exhibit high flutter speeds as engines are placed forward of the elastic axis (i.e. ψ is in the first and fourth quadrant). When the engines are placed behind the elastic axis (i.e. ψ is in the second and third quadrant) there is no significant peak in the flutter speed, and maximum flutter speed occurs mostly when both engines are closer to the root of the wing; see Figs. 120 – 127. It should be noted that normalized flutter speeds greater than 3 are beyond the incompressibility assumption in the aerodynamic model used in NATASHA. The results in this regime of flow cannot be trusted, but they could be used as an indication of how the trend of flutter speed might change.

For engine placement forward of the elastic axis, the unstable mode associated with the area with noticeable increase in flutter speed, i.e. 50% to 70% span, contains motion of a first bending-torsion coupled mode with second and third bending modes; see Figs. 119, 120, 121, 122, and 127.

On the other hand, for engine placement behind the elastic axis, although the trim solution is

symmetric, the unstable mode is antisymmetric – a first bending-torsion mode; see Figs. 123, 124 and 125. This is caused by excitations from an antisymmetric flight dynamic mode.

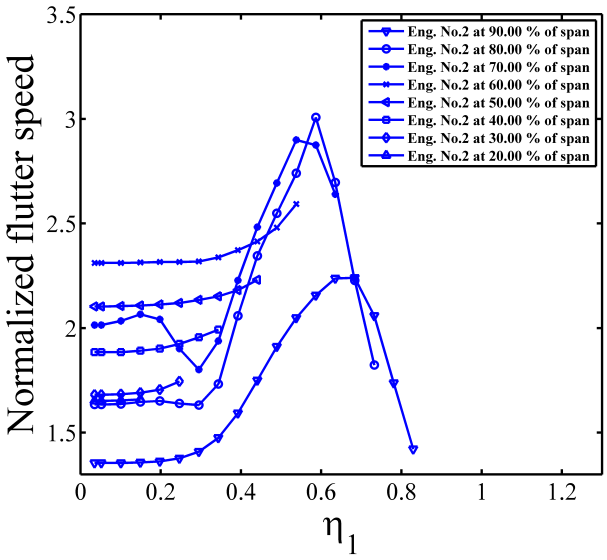

Figure 119: Normalized flutter speed for $r_1 = r_2 = 0$ and $\psi_1 = \psi_2 = 0°$

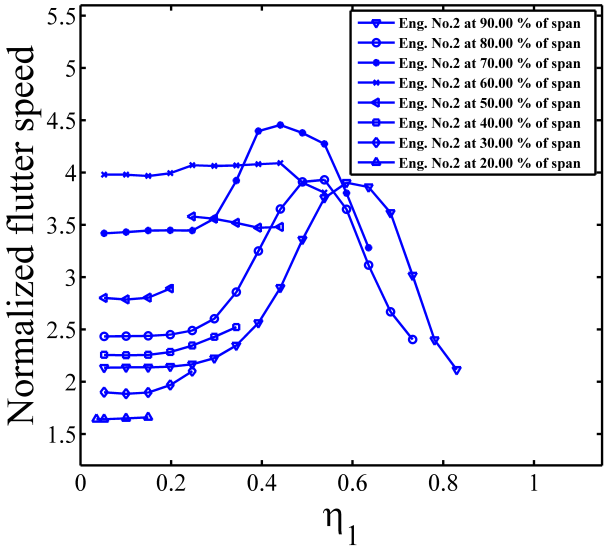

Figure 120: Normalized flutter speed for $r_1 = r_2 = 0.3$ and $\psi_1 = \psi_2 = 0°$

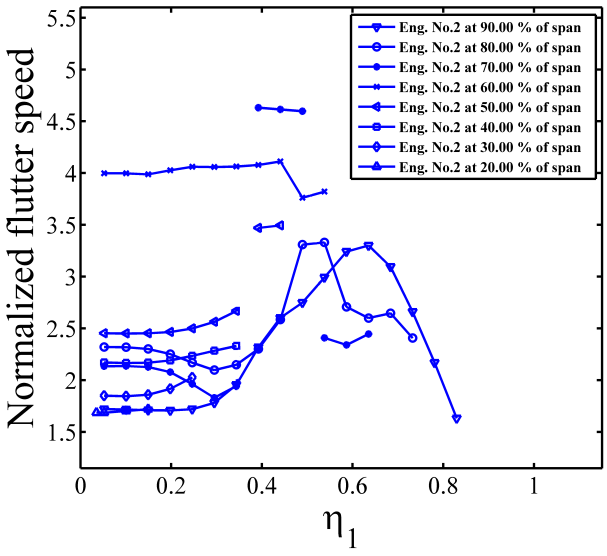

Figure 121: Normalized flutter speed for $r_1 = r_2 = 0.3$ and $\psi_1 = \psi_2 = 45°$

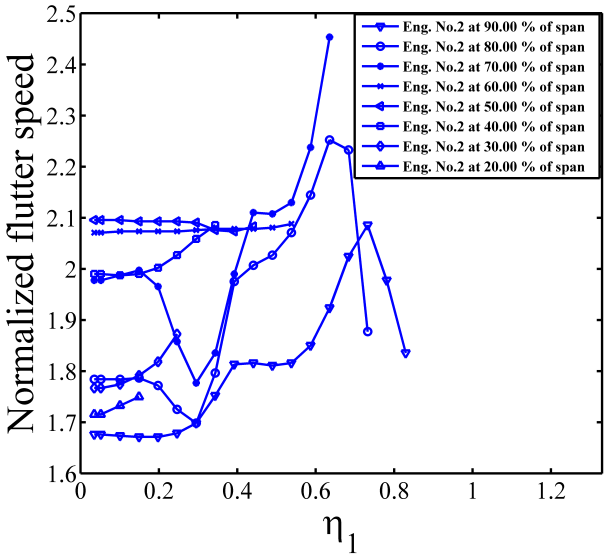

Figure 122: Normalized flutter speed for $r_1 = r_2 = 0.3$ and $\psi_1 = \psi_2 = 90°$

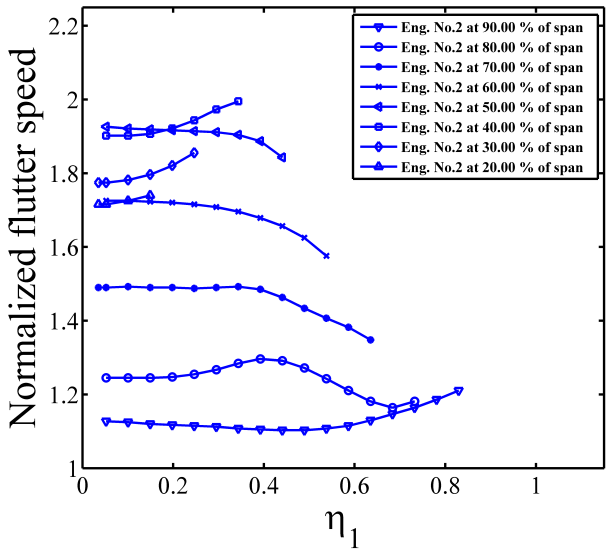

Figure 123: Normalized flutter speed for $r_1 = r_2 = 0.3$ and $\psi_1 = \psi_2 = 135°$

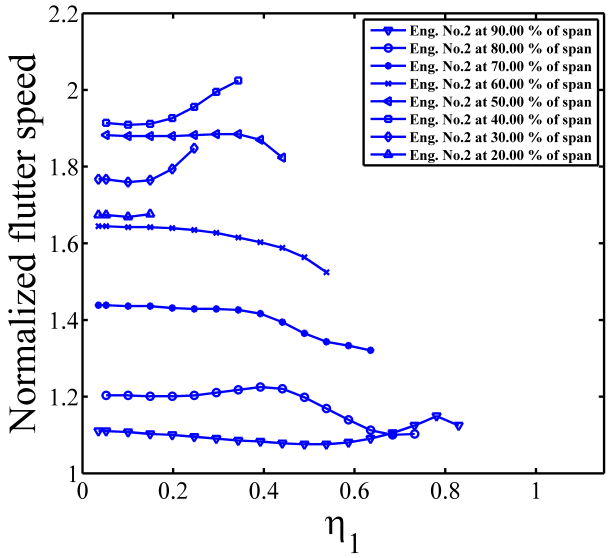

Figure 124: Normalized flutter speed for $r_1 = r_2 = 0.3$ and $\psi_1 = \psi_2 = 180°$

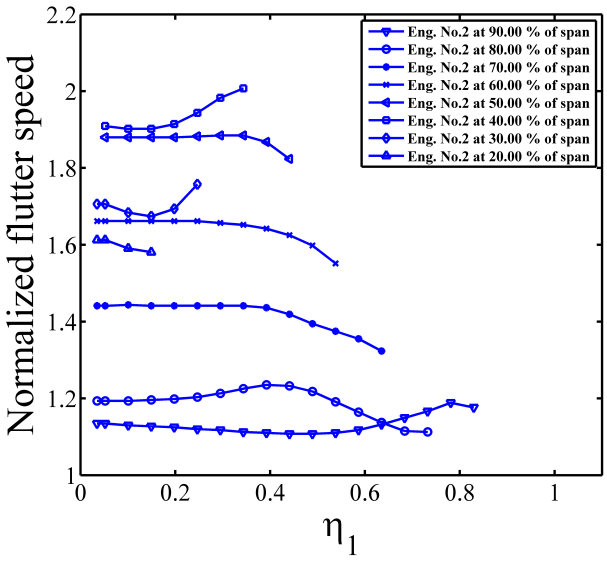

Figure 125: Normalized flutter speed for $r_1 = r_2 = 0.3$ and $\psi_1 = \psi_2 = 225°$

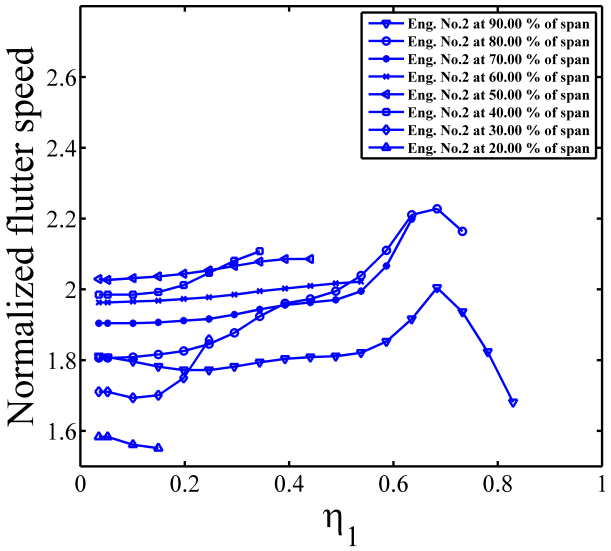

Figure 126: Normalized flutter speed for $r_1 = r_2 = 0.3$ and $\psi_1 = \psi_2 = 270°$

The maximum fluctuation of the flutter speed appears to be when the second engine is at 80% span and the first engine is between 50% to 70%. To further investigate this area, contour plots of the flutter speed and frequency are presented in Figs. 128 – 133, which show the contour of normalized flutter speed and frequency when the first engine is at 50% span and the second at 80% span. For

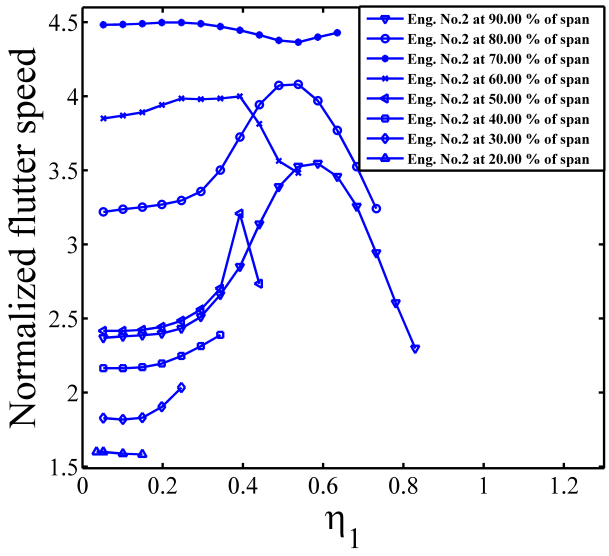

Figure 127: Normalized flutter speed for $r_1 = r_2 = 0.3$ and $\psi_1 = \psi_2 = 315°$

engine placement forward of the elastic axis, normalized flutter speed increases while there is little change in normalized flutter frequency. The same behavior was observed in flutter speed as the first engine is moved toward the outboard portion of the wing – closer to the second engine. However, there is a rapid increase in flutter frequency accompanied by a change in the unstable mode shape; see Figs. 130 – 133.

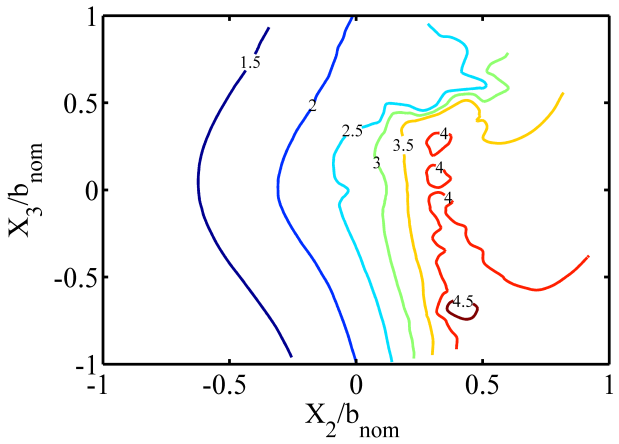

Figure 128: Normalized flutter speed contour for $\eta_1 = 0.5$ and $\eta_2 = 0.8$

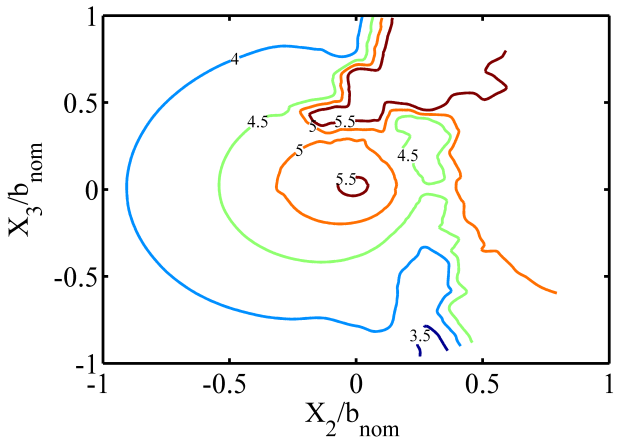

Figure 129: Normalized flutter frequency contour for $\eta_1 = 0.5$ and $\eta_2 = 0.8$

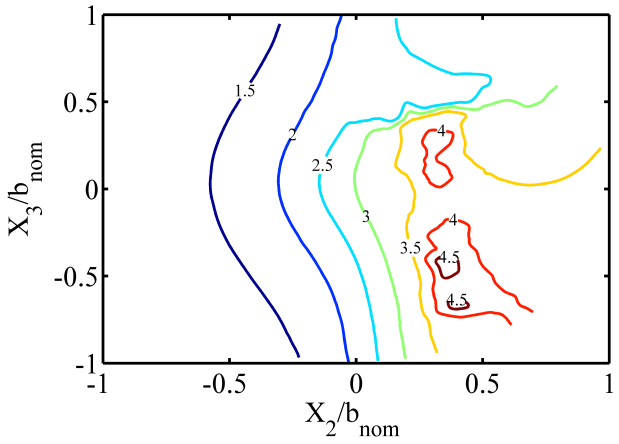

Figure 130: Normalized flutter speed contour for $\eta_1 = 0.6$ and $\eta_2 = 0.8$

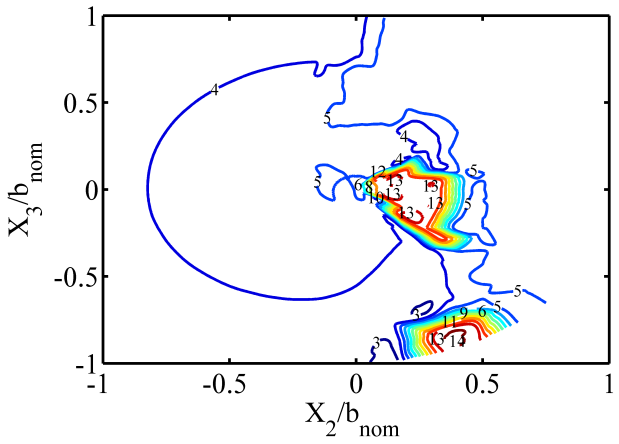

Figure 131: Normalized flutter frequency contour for $\eta_1 = 0.6$ and $\eta_2 = 0.8$

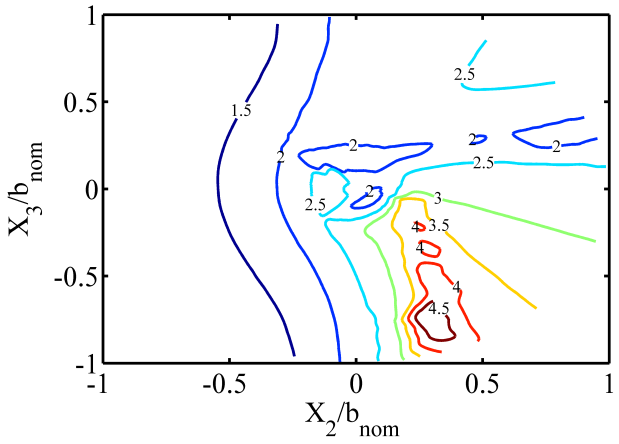

Figure 132: Normalized flutter speed contour for $\eta_1 = 0.7$ and $\eta_2 = 0.8$

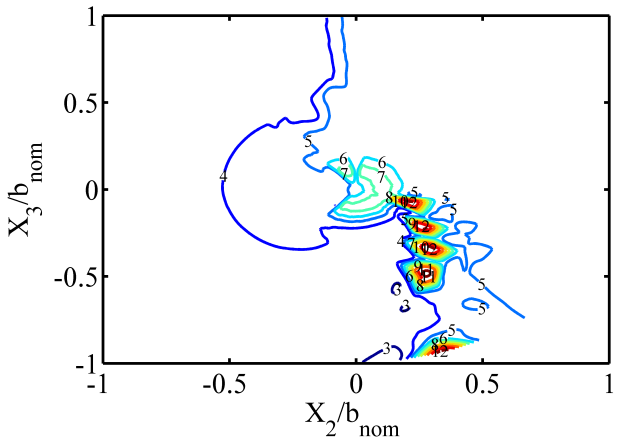

Figure 133: Normalized flutter frequency contour for $\eta_1 = 0.7$ and $\eta_2 = 0.8$

Another comparison is done for the case when the first engine is at 10% span while the second engine is moved outboard (i.e. 50% to 70% span). Contours of flutter speed and flutter frequency are presented in Figs. 134 – 139. When the second engine is placed at 50% span, as engines are moved forward of the elastic axis the flutter speed increases and flutter frequency changes slightly; see Figs. 134 and 135. Placement of the second engine at 60% span increases the flutter speed to a higher range, and flutter frequency experiences a rapid change as the unstable mode shape changes; see Figs. 136 and 137. When the second engine is placed farther outboard from the first (i.e. 70%), the flutter speed and frequency increase to higher values; see Figs. 138 and 139. In these cases, engine placement forward of the elastic axis increases the flutter speed.

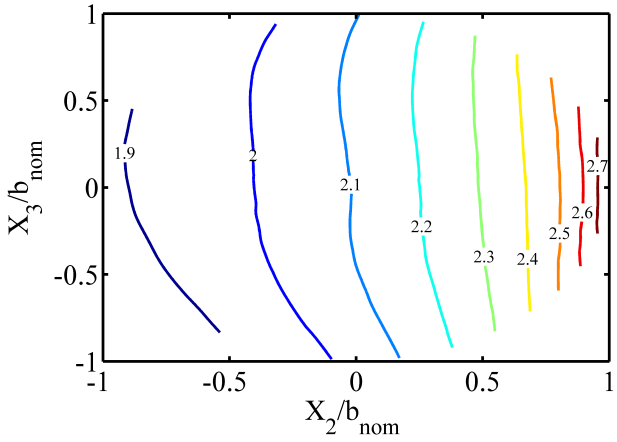

Figure 134: Normalized flutter speed contour for $\eta_1 = 0.1$ and $\eta_2 = 0.5$

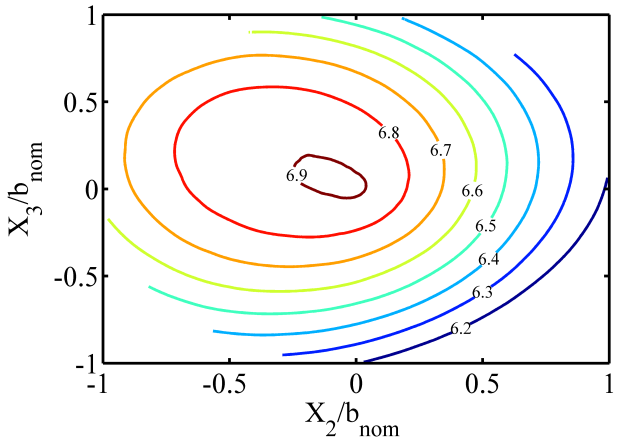

Figure 135: Normalized flutter frequency contour for $\eta_1 = 0.1$ and $\eta_2 = 0.5$

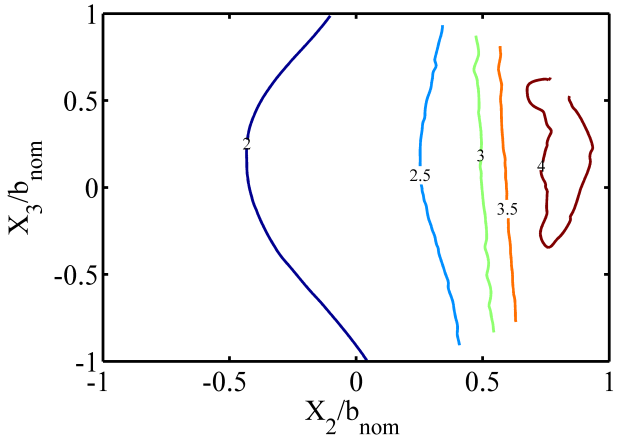

Figure 136: Normalized flutter speed contour for $\eta_1 = 0.1$ and $\eta_2 = 0.6$

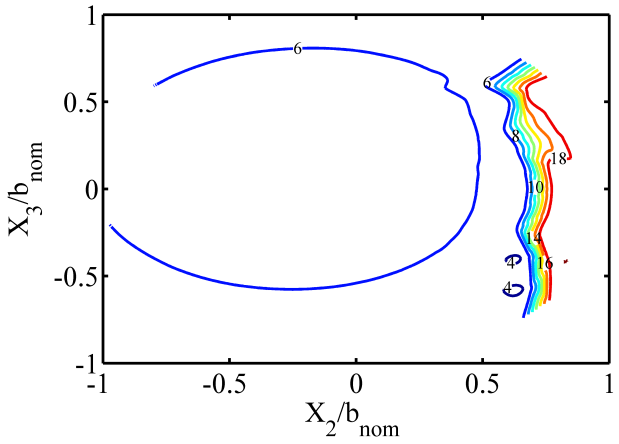

Figure 137: Normalized flutter frequency contour for $\eta_1 = 0.1$ and $\eta_2 = 0.6$

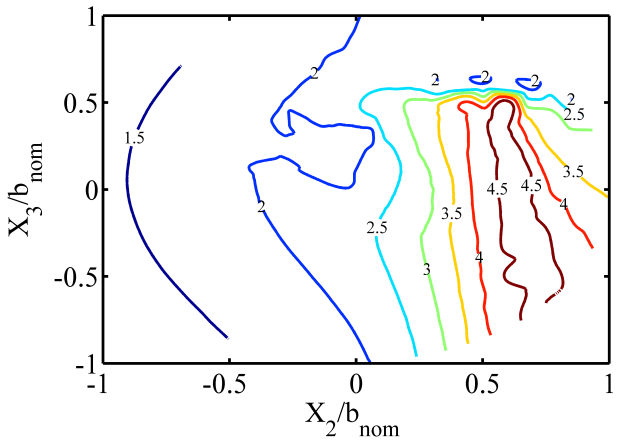

Figure 138: Normalized flutter speed contour for $\eta_1 = 0.1$ and $\eta_2 = 0.7$

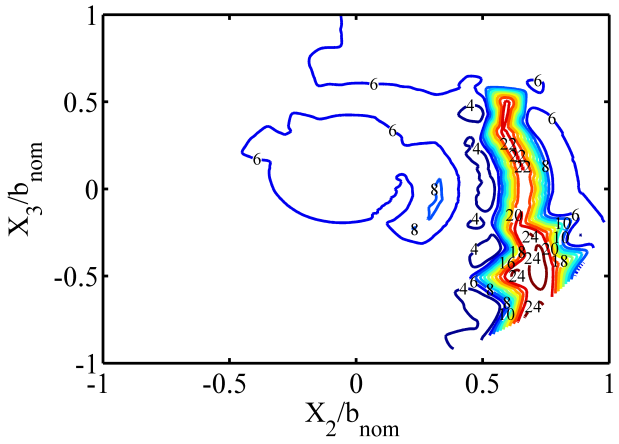

Figure 139: Normalized flutter frequency contour for $\eta_1 = 0.1$ and $\eta_2 = 0.7$

7.5 Area of minimum kinetic energy

In the absence of aerodynamics, gravitational force, and engines, NATASHA was used to calculate the kinetic energy of the modes of the aircraft; see Figs. 140 – 142. This analysis was done in order to find the region where the kinetic energy reaches its minimum for the first three lowest frequency elastic free-free bending modes. Thus, the area of minimum kinetic energy for the first and third bending modes is located around 60% span; see Figs. 140 and 142. For the second mode, this area has a local minima at 20% and 80% span; see Fig. 141.

For engine placement forward of the elastic axis, the unstable mode contains a combination of

first, second, and third bending modes; and when the engines are placed around 60% to 80% span, there is a noticeable increase in flutter speed. This area is close to the area of minimum kinetic energy of the first three bending modes; see Figs. 140 – 142.

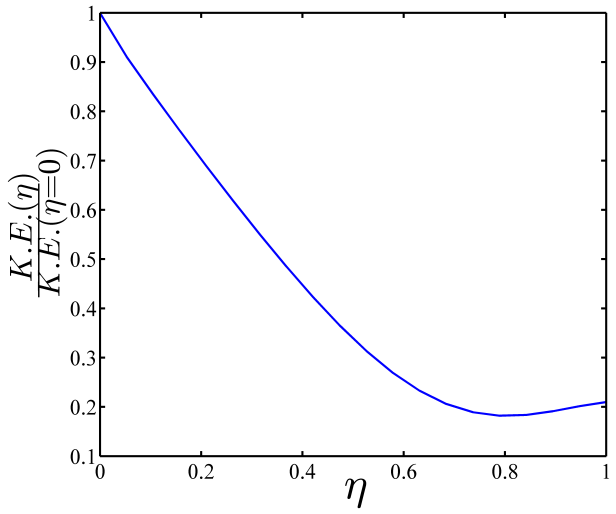

Figure 140: Normalized kinetic energy of the symmetric first free-free mode of the flying wing

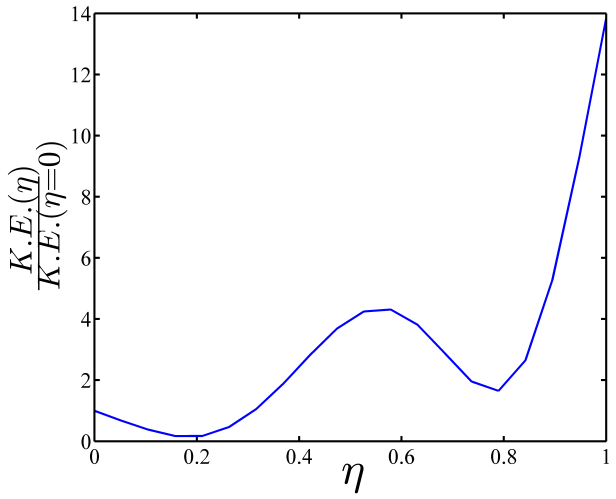

Figure 141: Normalized kinetic energy of the symmetric second free-free mode of the flying wing

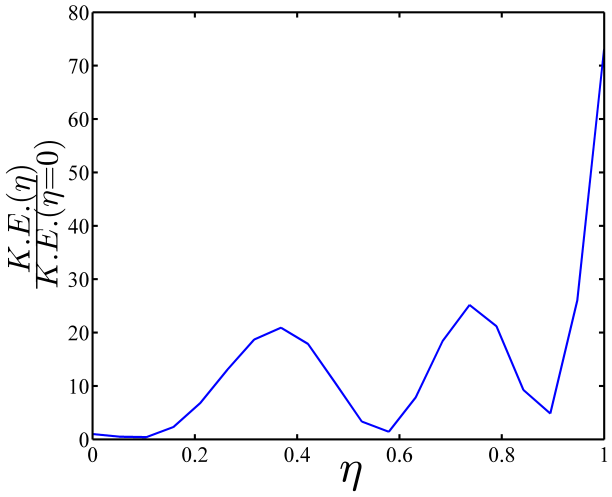

Figure 142: Normalized kinetic energy of the symmetric third free-free mode of the flying wing

7.6 Epilogue

Effects of multiple engine placement on flutter characteristics of a backswept flying wing resembling the HORTEN IV are investigated using the code NATASHA. Four identical engines with defined mass, inertia, and angular momentum are placed in different locations along the span with different offsets from the elastic axis while fixing the location of the aircraft c.g. The aircraft experiences body freedom flutter along with non-oscillatory instabilities that originate from flight dynamics. Multiple engine placement increases flutter speed particularly when the engines are placed in the outboard portion of the wing (60% to 70% span), forward of the elastic axis, while the lift to drag ratio is affected negligibly. The behavior of the sub- and supercritical eigenvalues is studied for two cases of engine placement. NATASHA captures a hump body-freedom flutter with low frequency for the clean wing case, which disappears as the engines are placed on the wings. In neither case is there any apparent coalescence between the unstable modes. NATASHA captures other non-oscillatory unstable roots with very small amplitude, apparently originating with flight dynamics. For the clean-wing case, in the absence of aerodynamic and gravitational forces, the regions of minimum kinetic energy density for the first and third bending modes are located around 60% span. For the second mode, this kinetic energy density has local minima around the 20% and 80% span. The

regions of minimum kinetic energy of these modes are in agreement with calculations that show a noticeable increase in flutter speed if engines are placed forward of the elastic axis at these regions.

Chapter VIII

PASSIVE MORPHING OF FLYING WING AIRCRAFT

[1]

8.1 Passive morphing of flying wing aircraft: Z configuration

In this study a solar powered High Altitude, Long Endurance (HALE) flying wing aircraft is considered to morph into a "Z" configuration to allow for sustained uninterrupted flight. Energy absorption of this aircraft is maximized if the sun exposure of the solar panels distributed on the wings is maximized.For this purpose a three-wing HALE flying wing follows the sun and morphs passively (without actuators at the hinges and only making use of aerodynamic force and thrust) into a Z shaped configuration, while the bending moments about hinge lines at the beam connections are zero. To capture these phenomena, NATASHA has been augmented with new equations to analyze aeroelastic trim, stability and time marching of such aircraft. Local bending moments are zeroed out at the beam connection points while the hinges are locked and are kept at zero while the aircraft morphs. The morphing motion is brought to a stop before the hinges are again locked. The emphasis of this study is to demonstrate the systematic processes required for passive morphing of a flying wing with Z configuration.

8.2 Theory behind passive morphing

NATASHA and *Nonlinear Composite Beam Theory* [40] were explained in sections 4.1 and 3.1, respectively. In this section, the theory behind NATASHA was extend to include the capability of aeroelastic analysis and simulation of passive morphing of flying wing aircraft.

[1] The content of this chapter is based on a journal article accepted for publication with minor revision by *Journal of Fluids and Structures.*

8.2.1 Trimming

The trim condition of the aircraft can be found by finding a steady-state solution of the aeroelastic equations from which with all time derivatives have been removed. NATASHA trims the aircraft for equality of lift to weight and thrust to drag by finding the controls of the aircraft (flap angles and individual engine thrusts) for a prescribed speed and climb angle. The symmetric trim equations at the aircraft reference node are [64]

$$\begin{aligned} \hat{g}_2\hat{V}_2 + \hat{g}_3\hat{V}_3 - \tan\phi(\hat{g}_3\hat{V}_2 + \hat{g}_2\hat{V}_3) = 0 \\ \hat{V}_2^2 + \hat{V}_3^2 - \hat{V}_\infty^2 = 0. \end{aligned} \tag{18}$$

As the aircraft morphs into an asymmetric configuration, a new set of trim equations at the reference node of the aircraft is required to trim the aircraft. These equations for zero flight path angle are:

$$\begin{aligned} \mathbf{V}^{ref} \cdot \mathbf{g}^{ref} &= 0 \\ \mathbf{\Omega}^{ref} &= 0 \\ {V_1}^{ref} &= 0 \\ |\mathbf{V}^{ref}| - V_\infty &= 0. \end{aligned} \tag{19}$$

In order to passively (i.e., avoiding actuators) morph the flying wing using aerodynamic forces and thrust, another set of equations in addition to the former trim equations is required to trim the aircraft. It is noted that these forces should fold the wings in a quasi-static morphing process so as to avoid inducing vibrations. It is also required that the moment about the folding hinge stays zero at each prescribed fold angle. For this purpose, a unit vector along the hinge line ($\mathbf{h}$) is introduced in the direction in which the hinges are designed to fold. The scalar product of the hinge vector and the total moment at the hinge location needs to be maintained zero, so that there is no resistance while folding occurs; thus,

$$\mathbf{M}_n \cdot \mathbf{h}_n = 0 \qquad n = 1, 2, \ldots. \tag{20}$$

Finally, for each hinge, a new equation is added to the system of aeroelastic equations along with a new set of flaps to the unknowns. A detailed explanation on the aeroelastic equations and variables for non-morphing configuration is available in the work done by [64]. The effects of hinge stiffness

and damping are neglected for the present study, but their addition is planned for a later work to enhance the realism of the model. The addition of hinge damping will allow energy dissipation to be taken into account, and it is expected that incorporation of a spring-restrained hinge may facilitate passive morphing. When the system of nonlinear aeroelastic equations is then linearized about the trim state, one obtains a generalized eigenvalue problem that NATASHA uses to assess stability. Because the velocity field is expressed in terms of the state variables of the problem in a geometrically exact manner, it means that the instantaneous velocity of the wing surface during morphing is taken into account in the stability (flight dynamic and aeroelastic) analyses.

8.2.2 Time marching

NATASHA is capable of time marching the aeroelastic system of equations using the scheduled control of the aircraft that comes from the trim solution [64]. When time marching the morphing process, four aircraft controls (a value for all engines and three flap settings) with prescribed location are scheduled to morph the aircraft over a suitable time period and time steps. The fold angles are the unknown variables in the state vector of the time marching, whereas in the trim solution they were prescribed. During the morph process, the morph speed (the time rate of the change of the fold angle) at each hinge is governed by

$$(\hat{\mathbf{\Omega}}_{l,n} - \hat{\mathbf{\Omega}}_{r,n}) \cdot \mathbf{h}_n = \dot{\theta}_n \qquad n = 1, 2, ... \tag{21}$$

where for the n^{th} hinge, $\hat{\mathbf{\Omega}}_{l,n}$ and $\hat{\mathbf{\Omega}}_{r,n}$ are the nodal left and right value for the angular velocity in the B basis and $\dot{\theta}$ is the time rate of change of the n^{th} fold angle.

8.3 Case study: solar powered flying wing

8.3.1 Flying wing configuration

In this study a very high aspect ratio flying wing is modeled with three beams connected to each other with two hinges about which folding takes place. Each beam has 12 elements and the length of each element on the middle beam is 15 ft, and on the side beams is 8 ft with a constant semi-chord value of 4 ft. The two terminal elements have a dihedral of 2°. The aspect ratio of the flying wing is 50.3 which makes it suitable to use the two-dimensional finite-state induced flow aerodynamic

Table 4: Flying wing cross-sectional properties

Elastic axis (reference line)	25% chord
Torsional stiffness	0.4×10^8 lb-ft^2
In-plane bending stiffness	2.5×10^8 lb-ft^2
Out-of-plane bending stiffness	30×10^8 lb-ft^2
Mass per unit length	3 slug/ft
Mass of each engine	0.3 slug
Angular momentum of engine	10 slug-ft^2/sec
Wing cross-sectional center of mass location	25% chord
Centroidal mass moments of inertia	
About the x_1 axis (torsional)	30 slug-ft
About the x_2 axis	5 slug-ft
About the x_3 axis	25 slug-ft
Sectional aerodynamic coefficients at 25% chord	
c_{l_α}	2π
c_{l_δ}	1
c_{d_0}	0.02
c_{m_0}	0.0005
c_{m_α}	0.01
c_{m_δ}	-0.25

model of [67]. There are four identical engines with prescribed mass, inertia and angular momentum placed at outer portion of the beams with zero offset from elastic axis; see Fig. 143. Three sets of flaps are distributed on the wings: one set (set 1) is on the side wings; the middle beam was divided into equal portions for the two other sets of flaps (sets 2 and 3); see Figs. 143 and 144. Table 4 describes the cross-sectional properties of the flying wing.

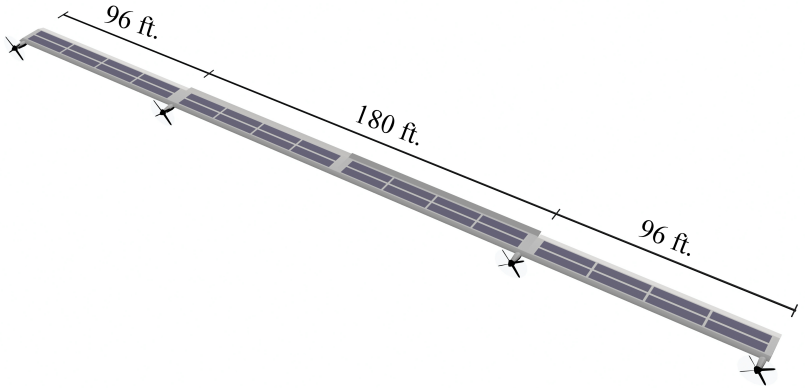

Figure 143: Geometry of the flying wing

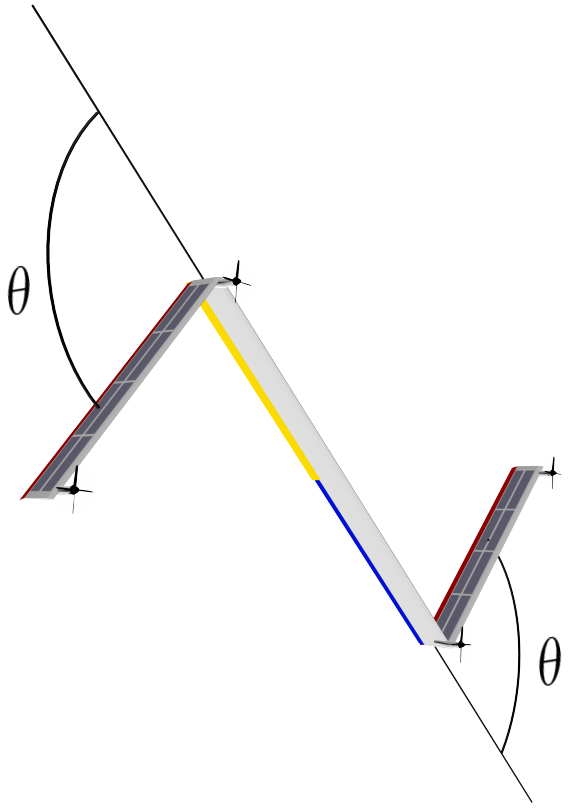

Figure 144: Schematic front view of the morphed configuration of the flying wing

8.3.2 Morphing process

The flying wing with distributed solar panels on the upper surface of the wings is scheduled to morph and change its geometry by folding the side wings from 0° to 45°. This change in geometry will lead to a Z-shaped configuration that maximizes the solar panel exposure to the sun (see Fig. 2) and consequently the solar energy absorbency, which provides power for sustained flight.

8.3.2.1 Aeroelastic trim and stability of passive morphing

The time independent schedule of the controls (thrusts and angle of flaps) of the flying wing, which morphs between two aeroelastically stable configuration with zero climb angle and unit load factor at 30 ft/sec, is obtained from the following trim conditions:

Trim condition 1 – ***Initial locked condition*** This is the initial trim condition where the aircraft is trimmed with zero fold angle, i.e. $\theta = 0°$, while the hinges are locked and completely loaded with connection moments and forces. The geometry of the aircraft still has a plane of symmetry

consequently the aircraft is trimmed using Eq. (18). Each thrust value is 15.9 lb., and all of the flaps equally deflect to the angle of 0.218°. Stability analysis shows that this configuration of the flying wing has directional instability with lead-lag motion with 0.027 rad/sec.

Trim condition 2 – ***Unloading and unlocking condition*** Before unlocking the hinges, one needs to remove the bending loads on the hinges so that it can be conveniently unlocked. For this purpose NATASHA is programmed to linearly decrease the moment about the fold direction from the value at the locked condition to zero, while the fold angle is maintained at zero ($\theta = 0°$). Theoretically, all steady state equilibrium equations are unchanged except Eq. (20). For these trim conditions the right hand side of the Eq. (20) is equal to the amount of the desired moment for each unloading condition of the hinges. In these conditions, the aircraft is trimmed with four trim variables (a set of thrust and three sets of flaps) while the geometry of the aircraft remains unchanged, and the aircraft still has a plane of symmetry. The thrusts remain unchanged, but the flap angles slightly change (from 0.218° to −0.5° for the middle beam, and to 0.8734° for side beams). Stability analysis shows that the unstable non-oscillatory flight dynamic mode is unaffected by this change.

Trim condition 3 – ***Morphing condition*** In the third condition the trim and stability of the aircraft are studied while it morphs from 0° to 45°. The new configuration is asymmetric and requires asymmetric trim equations; i.e., Eq. (19). In these trimmed conditions, thrust remains unchanged, and the three sets of flaps are found to follow another schedule: to trim the aircraft such that the moment about the hinge stays zero while the aircraft's angular velocity and sideslip velocity remain zero. Note that the load factor of the aircraft (the magnitude of $\hat{\mathbf{g}}$) remains unity. Although the new configuration is asymmetric, Eq. (19) dictates that the aircraft's angular and sideward velocity remain zero. Figure 145 shows the thrust requirement and Fig. 146 shows the flap requirement for this maneuver. As expected, the change in required thrust is insignificant because the primary source of drag for high-aspect ratio aircraft is the profile drag and skin-friction drag. This drag does not change as the aircraft morphs and the loss in lift is recovered by increase in the aircraft's angle of attack; see Fig. 147. Stability

analyses in these trim conditions capture the same unstable non-oscillatory flight dynamics mode the amplitude of which changes with no apparent regularity.

Trim condition 4 – ***Locking and loading condition*** In the fourth trim condition the fold angle reaches its final value (45°), and the geometry of the aircraft changes into Z-shaped configuration. When this configuration is attained, morphing stops and hinges could be locked and gradually loaded. It is necessary to load the hinges very gradually without any acceleration, so as to avoid impact and damage to the hinges. For gradual loading, the moment on the right hand side of Eq. (20) linearly increases to its final value obtained from the final locked condition. The angular velocity and sideslip velocity of the reference frame of the aircraft remain zero. Thrust remains unchanged, and the flaps change to 0.2°. NATASHA's stability analysis captures the same unstable flight dynamic mode the magnitude of which changes very slightly with no apparent regularity.

Trim condition 5 – ***Final locked condition*** In the final trim condition the aircraft is in the Z-shaped configuration with locked and loaded hinges. NATASHA trims the aircraft with its non-morphing aeroelastic equations [64] where the angle of the deflection of all flaps and the magnitude of all thrusts are the only two unknown trim variables of the problem. Stability analysis shows that the non-oscillatory unstable flight dynamics mode from the former trim conditions is accompanied with another non-oscillatory flight dynamic mode with eigenvalue 0.0310 rad/sec. The angular velocity and velocity of the aircraft reference frame have the same characteristics as in former trim conditions.

8.3.2.2 Aeroelastic stages of passive morphing

For maximum exposure of the solar cells to the sun, for instance from noon to evening twilight, the morphing maneuver needs to take place approximately within six hours; see Fig. 2. This requires the aircraft to morph gradually from 0° to 45°. This kind of morphing is referred to as "quasi-static" because changes in the structural configuration between time steps are very small, and the aircraft is always close to a trim solution. That is, the quasi-static process ensures that the system goes through

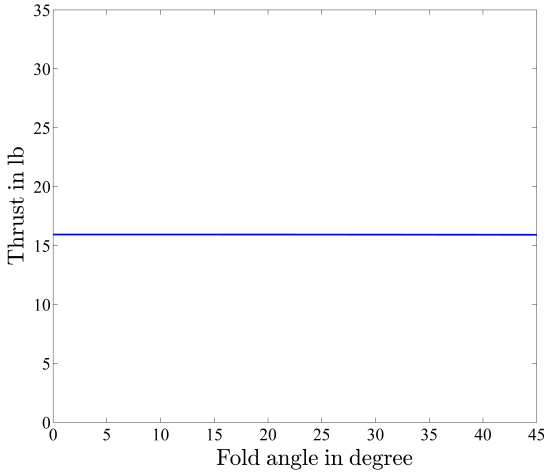

Figure 145: Each engine thrust vs. angle of morph

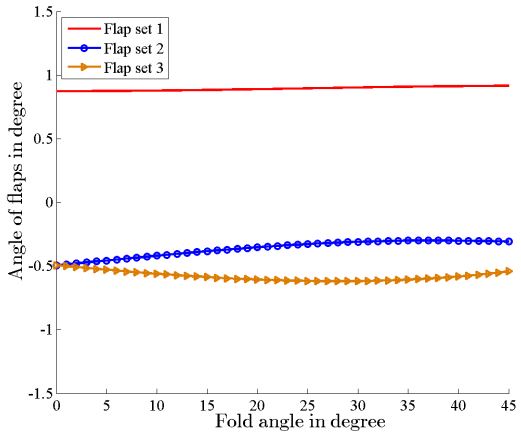

Figure 146: Deflection of flaps vs. angle of morph

a sequence of states that are infinitesimally close to trim solutions. Since this maneuver is assumed to be prolonged enough that meets the criteria for an ideal quasi-static maneuver, time dependent terms disappear from the equations. Without this assumption, it would have been necessary to time march and calculate the amount of required time to reach to a quasi-static process. NATASHA is capable of such time-marching to simulate this maneuver in the actual time period using second-order, central-difference, time-marching algorithm with high frequency dissipation [64]. This approach is, however, quite computationally expensive since a time step Δt of the order of 10^{-5} seconds is needed. For the purpose of saving time and cost in computations and considering the fact that the trim solutions are aeroelastically stable (i.e. small perturbations about the equilibrium states do not grow), one can

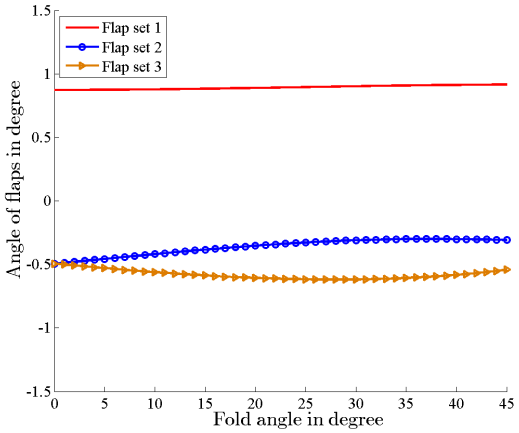

Figure 147: Angle of attack vs. angle of morph

introduce quasi-static simulation stages. One can then time march during each stage and simulate this maneuver with combinations of successive stages. In order to accomplish this, the flight controls are obtained from a sequence of trim conditions. These were curve-fitted to experience the following time-marching phases over the actual simulation time, and the state variables were evaluated at each converged time-marching solution for one time step during every stage of this maneuver. It was verified that increasing the number of stages does not affect the simulation since the equations are independent of time between the stages. One should take as many stages as necessary to accurately simulate this process. It should be noted that this scheme of simulation is different from an actual time marching scheme and, as such, can only be used for quasi-static maneuvers where the structure is always in the vicinity of equilibrium.

If it is required to morph the aircraft faster, then an active control system may be required to provide the aircraft flight-control schedule. For faster maneuvers, the design of this active control system can be achieved by noting the difference between the desired response and actual response for the pertinent time period. Once the actual response is known then the parameters of the active control system can be ascertained so as to bring the the actual solution in tune with the desired solution. However, for the current idealized problem, as mentioned previously, the quasi-static solution and its subsequent stages is sufficient since the morphing process takes place very gradually.

Phase 1 – ***Initial locked phase*** The first phase consists of 10 stages, while the flying wing is unfolded and hinges are locked and loaded. The schedule of the control of the aircraft is obtained from the sets of trim variables obtained from the first trim condition.

Phase 2 – ***Unloading phase*** As formerly mentioned, in order to avoid impact and shock to the structure which may lead to uncontrollable vibration it is required to remove the load in the direction in which the hinge is desired to fold and then unlock (removing a hypothetical pin from the hinge). The second phase is considered to gradually remove the bending moment about the folding hinge, and its associated trim condition is the second trim condition that schedules the thrust and the three sets of flaps such that the hinges are unloaded within 10 stages, while the fold angles are still zero. It was noticed while time marching the unloading phase, it is not required to set the right hand side of Eq. (20) to the amount of desired decreasing moment. In other words, the schedules of the control of the aircraft are set in a way that they enforce the loads on the hinge to decrease linearly in this phase.

Phase 3 – ***Unlocking phase*** Having the hinges unloaded, the aircraft reaches the state where the hinges could be unlocked. In this phase, the aircraft maintains its configuration such that the time rate of the change of the fold angles at 0° remains zero, i.e. $d\theta_n/dt = 0$ ($n = 1, 2$) for 10 stages. The schedules of the controls of the aircraft are the extension of the last trim condition obtained from unloading and unlocking trim condition over the corresponding stages.

Phase 4 – ***Morphing phase*** The main change in the geometry of the aircraft happens in morphing phase within a maneuver of 46 stages. During this phase, the aircraft morphs from a fold angle of 0° to 45° and changes its geometry into the Z-shaped configuration while the bending moment along the direction in which the hinges are folding is maintained zero.

Phase 5 – ***Locking phase*** In order to lock the hinge, it is necessary to keep $d\theta_n/dt = 0$ when $\theta_n = 45°$, ($n = 1, 2$). The schedule for this phase is the extension of the last trim condition over 10 stages.

Phase 6 – ***Loading phase*** When the hinge is locked at a fold angle of 45°, it will be loaded

gradually within 10 stages, using the schedule of the controls from the fourth trim condition, which was obtained by equating the right hand side of the Eq. (20) to the amount of the linearly increasing moment for each unloading condition. Like unloading phase, it is not required to change the right hand side of Eq. (20) over the pertinent stages.

Phase 7 – ***Final locked phase*** The final phase is comprised of 10 stages, while the hinges are locked and loaded. The aircraft is in Z-shaped configuration with a fold angle of 45°.

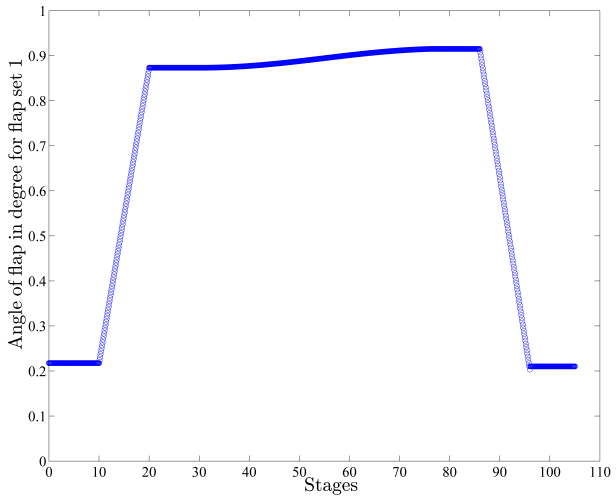

Figure 148: Schedule of angle of flap for set 1 vs. stages

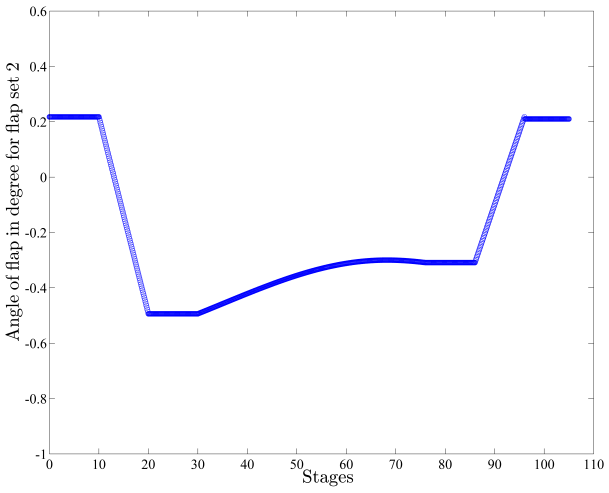

Figure 149: Schedule of angle of flap for set 2 vs. stages

Figure 152 depicts a schematic of the morphing process and Fig. 153 shows the change of the fold

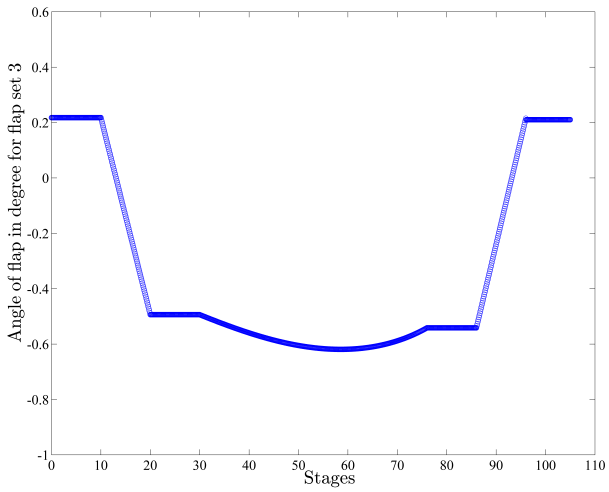

Figure 150: Schedule of angle of flap for set 3 vs. stages

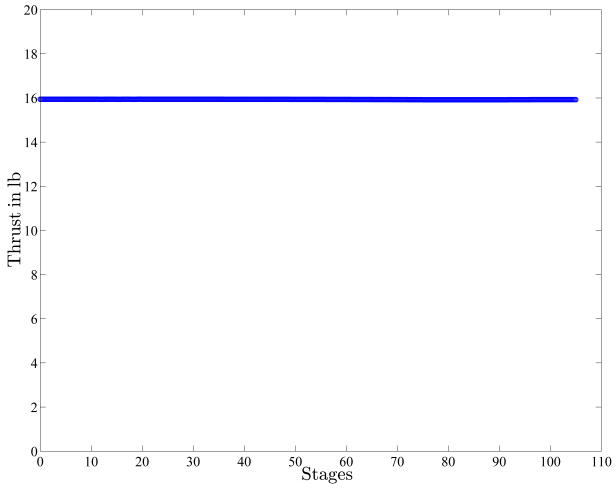

Figure 151: Schedule of thrust vs. stages

angle during all the time marching phases of the aircraft over 106 stages. Figures 154 – 156 show the beam connection moment at the second hinge for the entire morphing process in the B basis normalized with the amplitude of the beam connection moment at zero time. It is noteworthy that coming back to the original configuration (i.e., unfolded configuration) is straightforward, requiring one to time-march the aeroelastic equations by reversing the schedule of aircraft's controls obtained earlier from the trim solutions.

8.4 Epilogue

HALE aircraft can achieve sustained, uninterrupted flight time if they use solar power. Wing morphing of solar powered HALE aircraft can significantly increase solar energy absorbency. An example of the kind of morphing considered in this chapter requires the wings to fold so as to orient a solar panel to be hit more directly by the sun's rays at specific times of the day. In this study solar powered HALE flying wing aircraft are modeled with three beams with lockable hinge connections. Such aircraft are shown to be capable of morphing passively, following the sun by means of aerodynamic forces and engine thrusts. The analysis underlying NATASHA was extended to include the ability to simulate morphing of the aircraft into a "Z" configuration. Because of the "long endurance" feature of HALE aircraft, such morphing needs to be done without relying on actuators and at as near zero energy cost as possible. The emphasis of this study is to substantially demonstrate the processes required to passively morph a flying wing into a Z-shaped configuration and back again.

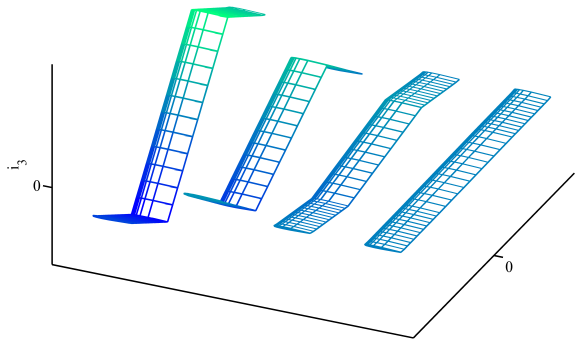

Figure 152: Passive flying wing morphing

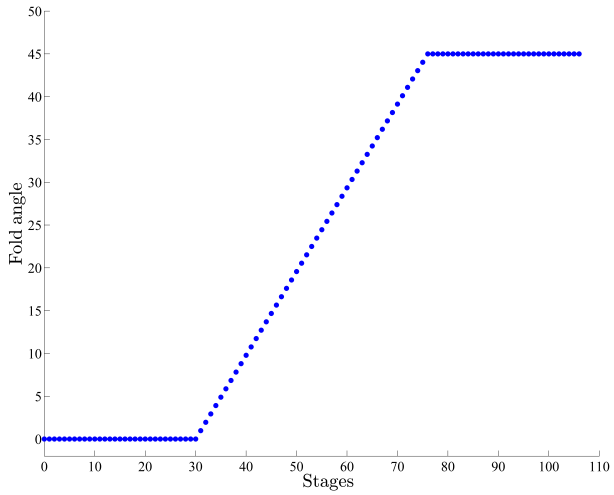

Figure 153: Fold angle vs. stages

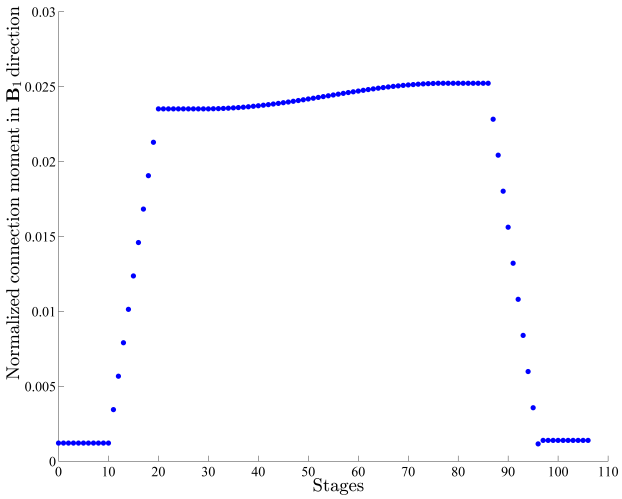

Figure 154: Connection moment in $\mathbf{B}_1$ direction vs. stages

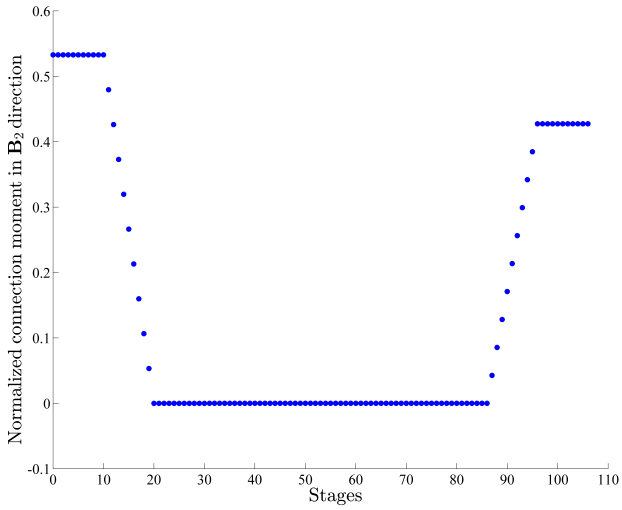

Figure 155: Connection moment in $\mathbf{B}_2$ direction vs. stages

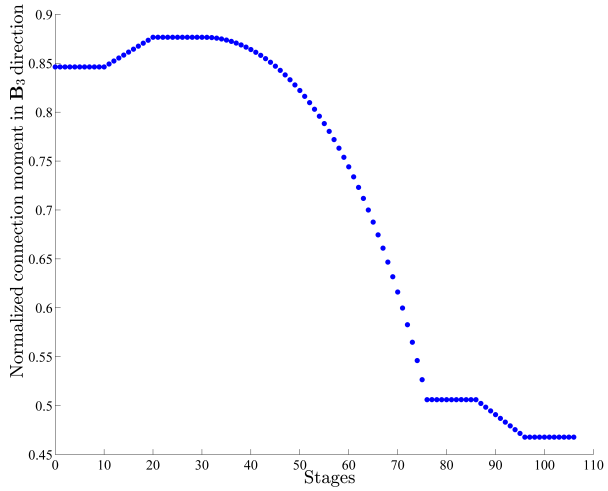

Figure 156: Connection moment in $\mathbf{B}_3$ direction vs. stages

Chapter IX

CONCLUSIONS AND FUTURE WORK

9.1 Conclusions

NATASHA's results for the pre- and post-instability behavior of the eigenvalues were validated and the results are in excellent agreement. For the case of sweep effects, NATASHA showed an excellent agreement both in divergence and flutter speed for the classical Goland wing.

In subsonic flow, a very flexible high-aspect-ratio wing which displays geometrically nonlinear behavior is analyzed using NATASHA. For the the case of clean wing, the behavior of the eigenvalues at pre- and post instability in two conditions, with and without gravity is studied. In the absence of gravity, the wing flutters at 32.1 m/s with an frequency of 22.534 rad/sec. The associated mode is a first bending-torsion mode and divergence occurs at 34.6 m/s. NATASHA's result is in good agreement with previously published work. When the effect of gravity is considered, the wing flutters at 22.4 m/s with a hump first bending-torsion mode with a frequency of 12.199 rad/sec which returns to the stability region at higher speeds. At 45 m/s the second bending-torsion with a frequency of 27.406 becomes unstable.

For stability analysis, a light weight small class thrust engine (JetCat SP5) operating at cruise condition is considered. Effect of engine placement along the span with offsets from elastic axis are studied for two cases, with and without gravity. Stability analysis without gravity shows that engine placement at 60% to 80% span forward of the elastic axis increase the flutter speed more than three times of the base model while engine placement between 70% to 95% span, offset in normal direction increases the flutter speed up to 75% of the base model. A plane of symmetry in the results was observed which was due to neglecting the effect of gravity. NATASHA's result for flutter characteristics with gravity captures significant increase in flutter speed, more than three times of the base model, for engine placement at 60% to 80% span forward of the elastic axis. In stability analysis with gravity, significant decrease in flutter speed is observed for engine placement

at 30% to 50% span backward elastic axis, i.e., in $\mathbf{b_2}$ direction, and upward the elastic axis, i.e., in $\mathbf{b_3}$ direction. These low flutter speed zones were not captured when gravity was neglected.

Effect of load factor on aeroelastic stability of the wing for engine placement along the span with offsets from elastic axis is studied by change in the magnitude of the gravity vector, i.e., $\mathbf{g}$. Three cases of load factor which occur while an aircraft undergoes bank angles of 30°, 45° and 60° are presented. While bank angle is 30° or 45°, i.e., load factor of 1.2 and 1.4, flutter characteristics still have the same behavior compared to straight level flight, i.e., zero bank angle. At 60° of bank angle, load factor increases to two, and the effects become significant in flutter speed and its sensitivity to engine placement. At this load factor, NATASHA's results show that flutter speed decreases, and higher flutter speed is attained for engine placement between 20% to 60% span, forward offset the elastic axis in chordwise direction. This zone has 30% decrease in flutter speed compared to the base model. Flutter speed increases on the inboard portion of the wing for engine placement in normal direction, the results at this load factor show that flutter characteristics are independent of the offsets from elastic axis at each span wise location.

For the clean wing without gravity and aerodynamic forces, the area of minimum kinetic energy density of the first two elastic bending and torsion modes are calculated. The second bending mode has a local maxima at 45% to 55% span and a local minima at 80% to 90% span and the second torsion mode has these extremums at 30% to 40% and 65% to 75% span. The stability analysis for engine placements (with and without gravity) show that engine placements forward of the elastic axis at the area of minimum kinetic energy of the second modes increase flutter speed and significant decrease in flutter speed is observed when effect of gravity is considered. In this case, flutter speed decreases for engine placement behind or upward the elastic axis at the area of maximum kinetic energy of the second modes.

Effects of engine placement with time-dependent engine thrust and dynamics on nonlinear aeroelastic response of the high-aspect-ratio wing are studied by the second-order, central-difference, time marching algorithm with high frequency damping in NATASHA. The appropriate time step is 0.05 seconds. The transient behavior of the engine, i.e., thrust and angular momentum of spools, for

rectangular pulse and ramp fuel profile, both from cruise to maximum level is simulated using Jet-Cat SP5 engine model. At air velocity of 20 m/s, the aeroelastic response of the wing excited by time-dependent thrust, for engine placements along the span (25%, 50%, 75% span and at the tip of the wing) with offset from elastic axis in the order of chord is studied for two types of excitations.

In the case of rectangular pulse, fuel input, thrust, and angular momentum resemble a realistic impulse excitation. For engine placement at 25% span, stability analysis with engine thrust and angular momentum at cruise level shows that engine placement with no offset and at $r = 1$ and $\psi =$ 90, 135° and 180° is supercritical and other locations are subcritical. The time march results show that excitation at this locations attenuate quickly. It can be gathered from the stability analysis that most of engine offsets at 50% span are aeroelastically stable in linearized analysis and the excitation dies out. On the other hand, for two cases where the engine placements are supercritical; engine placement at $r = 1$ and $\psi = 90°$, the excitation still dies out, and at $r = 1$ and $\psi = 135°$ where the excitation results in a stable LCO.

For engine placement at 75% span, linearized stability analysis show that engine placement at $r = 1$, $\psi = 90°$ and 180° is supercritical; in both cases the excitation dies out. Engine placement at $r = 1$, $\psi = 135°$ is supercritical and leads to a stable LCO. Other engine placements at this location are aeroelastically stable in linearized analysis and the excitations die out. For engine placement at the tip of the wing, i.e., 100% span, only at $r = 1$, $\psi = 180°$ is supercritical and excitation at this location leads to stable LCO. When engine is placed offset forward of the elastic axis, i.e., $r = 1$, $\psi = 0°, 45°, 90°, 270°$ and 315°, the excitation dies out and when engine is place at $r = 1$, $\psi = 135°$ excitation leads to a stable LCO and after 50 second it quickly dies out. When engine is offset at $r = 1$, $\psi = 225°$, excitation at subcritical leads to stable LCO. In case of the ramp excitation, the time march results for engine placement at 25% span show that engine placement at this location is stable and for engine placement at 50% span, at $r = 1$, $\psi = 90°$ and 135 ° stable limit cycle oscillation is observed and excitations for other engine placements at this location do not affect stability of the wing. For engine placement at 75% span, at $r = 1$ and $\psi = 45°$, at subcritical, excitation leads to oscillations with growing amplitude and at $\psi = 45°$ and 180°, at supercritical

leads to stable LCO. Engine placement at $r = 1$ and $\psi = 135°$, at supercritical, the excitation introduces a chaotic oscillation to the structure and all other engine placements are unaffected by this excitation; barring a change in the static deflection. The effect of this excitation for engine placement at the tip of the wing leads to a very large amplitude oscillation and for the case of $r = 1$, $\psi = 180°$ the large amplitude oscillations is a stable LCO.

An anisotropic flying wing was considered, with geometry similar to the Horten IV properties of which were linearly varying along its span with two identical engines with mass and angular momentum. This flying wing, for the clean wing case, fluttered at 85.5 MPH, with the unstable modes being the aeroelastic body-freedom mode with a frequency of 2.9 Hz, and a non-oscillatory yawing instability with a small real eigenvalue of 0.05 rad/s that caused the aircraft to rotate in the horizontal plane. NATASHA captured another symmetric bending mode on the stability boundary with a frequency of 0.08 Hz, appearing when the engines were at their farthest offsets from the elastic axis and at the tip of the wings but with no apparent regularity. The effect of aft sweep for this flying wing with three different engine locations along the span showed the increase of flutter speed, as expected. The effect of engine placement along the span with varying offsets up to the order of mean semi-chord from the elastic axis showed that the maximum flutter speed occurs when the engines are just outboard of 60% span. The minimum flutter speed occurs for engine placement at the wing tips. Both minima and maxima occurred when the c.g. of the engine was forward of the wing elastic axis. The effect of engine placement with constant aircraft c.g. not only kept the control response of the aircraft unchanged and in the linear range, but it increased the flutter speed significantly while also smoothing out its variation along the span.

In the absence of engines and aerodynamic and gravitational forces, NATASHA found that the minimum kinetic energy region is very near 60% span for the first symmetric elastic free-free bending mode. It is interesting that this location coincides with the region where the maximum flutter speed was observed. Whether or not knowledge of the minimum kinetic energy region has any potential to help the designer place the engines requires further investigation, but if a connection were established it could lead to significant savings in computational effort.

The aeroelastic trim and stability of a flying-wing aircraft with four engines was analyzed. The aircraft model had a geometry similar to that of the Horten IV with the addition of four identical engines of specified mass, moments of inertia, and angular momentum. The four engines are symmetrically moved along the span with offsets from the elastic axis while fixing the location of aircraft c.g. For the clean wing case, the aircraft experiences body freedom flutter at 40.8 m/s with a frequency of 9.560 rad/s. The behavior of sub- and supercritical eigenvalues was studied for two cases of engine placement, both with zero offset from the elastic axis but with different locations along the span. The clean-wing case experiences a hump-mode flutter, and as the engines are moved toward the outer portion of the wing the unstable mode contains a combination of the first, second, and third bending along with torsion and the aircraft short period mode. In this case, the hump-mode is not unstable. In both cases, there is no apparent coalescence between the unstable modes. NATASHA also captures other non-oscillatory unstable roots from flight dynamics origin.

This study shows that engine placement does not have any significant effect on the lift to drag ratio. However, a noticeable increase in flutter speed is observed when engines are placed forward of the elastic axis. For these cases, as one of the engines is placed at the outboard portion of the span, flutter speed increases. For engine placement behind the elastic axis, flutter speed increases when both engines are close to the root.

In the absence of aerodynamics, gravitational force, and engines, the area of minimum kinetic energy for the first and third bending modes is located at approximately 60% span. For the second mode, the kinetic energy has local minima around 20% and 80% span. The areas of minimum kinetic energy for these modes are in agreement with flutter calculations, which show a noticeable increase in flutter speed if engines are placed forward of the elastic axis at these regions.

The analysis underlying NATASHA was extended to include the ability to simulate morphing of the aircraft using a new set of trim and kinematical differential equations. An example of the kind of morphing considered in this study requires the wings to fold so as to orient a solar panel to be hit more directly by the sun's rays at specific times of the day. Because of the "long endurance" feature of HALE aircraft, such morphing needs to be done with as near zero energy cost as possible, i.e.,

without relying on actuators at the hinges, but instead making use of aerodynamic forces and engine thrust. The three-wing solar powered HALE aircraft morphs passively into a Z-shaped configuration while local bending moments are zeroed out at the beam connection points, but with the hinges locked and held at zero while the aircraft morphs. The morphing motion is brought to a stop before the hinges are again locked. Systematic processes for trim and time-marching for a passively morphing flying wing are presented. The schedule of the control of the aircraft for morphing was obtained from the trim conditions and was curve-fitted over 106 stages. The stability analysis of the trim conditions showed that this aircraft is aeroelastically stable and the instabilities are flight dynamics modes with very small non-oscillatory eigenvalues. The nonlinear algebraic aeroelastic time-marching solution was found by the Levenberg-Marquardt scheme, and the appropriate time step which met the criteria of the equilibrium condition of this configuration was 10^{-5} sec.

9.2 Future work

For the problem of passive wing morphing the effects of hinge stiffness and damping are neglected for the present study, but their addition is planned for a later work to enhance the realism of the model. The addition of hinge damping will allow energy dissipation to be taken into account, and it is expected that incorporation of a spring-restrained hinge may facilitate passive morphing and gust response of the aircraft during the morphing phases. Other recommendations for future studies include addition of the 3D Peters aerodynamic model to account for moderate aspect-ratio wings and axial flow. Such an aerodynamic model will extend the validity of analysis done by NATASHA to rotary wings.

In the present study the effect of engine aerodynamics has been considered. Explicit formulation of the same would require the use of 3D Computational Fluid Dynamic (CFD) model. At this present moment, to the best of the author's knowledge accurate simulation of the engine aerodynamics will retain the qualitative aspect of the current analysis but might lead to some quantitative improvements. Another aspect worthy of future investigation is to account for the flexibility of the engine nacelle and mount. It will be interesting to outline whether consideration of their flexibility and the resulting dynamics affects the aeroelastic behavior of the aircraft. In the present work the

inertial properties and flexibilities of control surfaces are not studied, including those in NATASHA facilitates the simulations.

Chapter X

APPENDIX

10.0.1 Case study: two-engine flying wing

Table 5: Air density and sectional aerodynamic properties of the wing

Air density (lb sec^2 in^{-4})	$\rho_{air} = 1.1463 \times 10^{-7}$								
	c_{l_0}	c_{l_α} (rad^{-1})	c_{l_δ} (rad^{-1})	c_{d_0}	$c_{d_{\alpha 2}}$ (rad^{-2})	$c_{d_{\delta 2}}$ (rad^{-2})	c_{m_0}	c_{m_α} (rad^{-1})	c_{m_δ} (rad^{-1})
Wing root	0.10695	6.9476	4.2891	0.00582	0.08638	- 0.111	0.01125	-0.113	-0.62243
Wing tip	0.00550	6.9981	4.3288	0.00674	0.27027	0.083	-0.00024	-0.083	-0.72767

Table 6: Properties of the engines and pilot

Mass of pilot (lb sec^2 in^{-1})	$\hat{\mu}_{pilot} = 0.9$
Pilot position, non-fixed c.g. (in)	$\hat{\xi}_{pilot} = (0, -10, -10)^T$
Mass of each engine (lb sec^2 in^{-1})	$\hat{\mu}_{engine} = 0.03$
Angular momentum of engine (lb sec in)	$\hat{H}_{engine} = (0, 51.169, 0)^T$
Engine mass moment of inertia: (lb sec^2 in)	$\hat{I}_{engine} = \begin{bmatrix} 2.6 & 0 & 0 \\ 0 & 2.6 & 0 \\ 0 & 0 & 2.6 \end{bmatrix}$

Table 7: Sectional properties of the wing

Wing mass per unit span (lb sec^2 in^{-2})†	$\mu_{root} = 0.003962$	$\mu_{tip} = 0.00040422$
Position of reference point with respect to mid-chord (in)	$(0, -0.15, 9.42)^T$	$(0, -0.21, -0.50)^T$
Position of elastic axis with respect to sectional c.g. (in)	$\xi_{root} = (0, 5.29, -0.594)^T$	$\xi_{root} = (0, -1.644, -0.563)^T$
Position of aerodynamic center with respect to sectional c.g. (in)	$y_{ac_{root}} = (0, 5.434, 0)^T$	$y_{ac_{tip}} = (0, 0.2102, 0)^T$
Wing initial twist per unit span (rad/in)	$k_{root} = (0.0001, 0, 0)^T$	$k_{tip} = (0.0001, 0, 0)^T$
Wing cross-sectional inertia per unit span (lb sec^2)	$I_{root} = \begin{bmatrix} 67 & 0 & 0 \\ 0 & 2.7 & 0 \\ 0 & 0 & 66.2 \end{bmatrix} \times 10^{-2}$	$I_{tip} = \begin{bmatrix} 0.2 & 0 & 0 \\ 0 & 0.014 & 0 \\ 0 & 0 & 0.18 \end{bmatrix} \times 10^{-2}$
Wing structural flexibility matrix (lb^{-1})	$R_{root} = \begin{bmatrix} 3.09 & 0 & 0 \\ 0 & 0 & 0 \\ 0 & 0 & 0 \end{bmatrix} \times 10^{-10}$	$R_{tip} = \begin{bmatrix} 7.59 & 0 & 0 \\ 0 & 0 & 0 \\ 0 & 0 & 0 \end{bmatrix} \times 10^{-8}$
Wing structural flexibility matrix (in^{-1} lb^{-1})	$S_{root} = \begin{bmatrix} 7.54 & 1.83 & 7.83 \\ 18.34 & 0 & 0 \\ 7.83 & 0 & 0 \end{bmatrix} \times 10^{-12}$	$S_{tip} = \begin{bmatrix} 2.24 & 5.23 & 0.03 \\ 5.23 & 0 & 0 \\ 0.03 & 0 & 0 \end{bmatrix} \times 10^{-8}$
Wing structural flexibility matrix (in^{-2} lb^{-1})	$T_{root} = \begin{bmatrix} 3.63 & 0 & -0.092 \\ 0 & 5.7 & 0.017 \\ -0.092 & 0.017 & 0.13 \end{bmatrix} \times 10^{-11}$	$T_{tip} = \begin{bmatrix} 105.46 & 56.26 & 8.81 \\ 56.26 & 20.10 & 1.68 \\ 8.81 & 1.68 & 10.36 \end{bmatrix} \times 10^{-9}$

† Note the system of measurement used in this study is inches, seconds and pounds for length, time, and force, respectively.

10.0.2 Case study: four-engine flying wing

Table 8: Sectional properties of the wing

Elastic axis (reference line)	25% chord
Axial stiffness	1.162×10^8 kg/s^2
Torsional stiffness	1.883×10^5 kg-m^2
In-plane bending stiffness	1.349×10^7 kg-m^2
Out-of-plane bending stiffness	1.660×10^5 kg-m^2
Mass per unit length	9.193 kg/m
Initial Curvature	1.70×10^{-3}/rad
Mass offset	-0.285 m
Wing inertias per unit span:	
About the b_1 axis	1.0132 kg-m
About the b_2 axis	0.0303 kg-m
About the b_3 axis	0.9829 kg-m

Table 9: Sectional aerodynamic properties of the wing

	root	tip
c_{l_0}	1.07×10^{-1}	5.5×10^{-3}
c_{l_α}	6.9476 rad^{-1}	6.9981 rad^{-1}
c_{l_δ}	4.2891 rad^{-2}	4.3288 rad^{-2}
c_{d_0}	5.82×10^{-3}	6.74×10^{-3}
c_{m_0}	1.13×10^{-2}	-2.4×10^{-4}
c_{m_α}	-1.13×10^{-2} rad^{-1}	-8.3×10^{-2} rad^{-1}
c_{m_δ}	-6.224×10^{-1} rad^{-1}	-7.276×10^{-1} rad^{-1}
Aerodynamic coefficient at 25% chord		

Table 10: Properties of the engines

Mass of each engine	10 kg
Angular momentum of engine	5.829 kg-m$^2/s$
Engine mass moment of inertia:	
About the b_1 axis	0.3 kg-m^2
About the b_2 axis	0.3 kg-m^2
About the b_3 axis	0.3 kg-m^2

REFERENCES

[1] "Jetcat spt5 turboshaft engine manual," tech. rep., 2009.

[2] "Jetcat spt5 turboshaft engine," Tech. Rep. `http://www.jetcatusa.com/spt5.html`, 2012.

[3] Andersen, G. R., Cowan, D. L., and Piatak, D. J., "Aeroelastic modeling, analysis and testing of a morphing wing structure," in *Proceedings of the 46th AIAA/ASME/ASCE/AHS/ASC Structures, Structural Dynamics and Materials Conference, Austin, Texas*, (Reston, Virginia), AIAA, April 18 – 21, 2007.

[4] Attar, P. J., Tang, D., and Dowell, E. H., "Nonlinear aeroelastic study for folding wing structures," *AIAA Journal*, vol. 48, October 2010.

[5] Balakrishnan, A., *Aeroelasticity: The Continuum Theory*. Dordrecht: Springer, 2012.

[6] Banerjee, J. R., "Flutter modes of high aspect ratio tailless aircraft," *Journal of Aircraft*, vol. 25, pp. 473 – 476, May 1988.

[7] Banerjee, J., "Flutter characteristics of high aspect ratio tailless aircraft," *Journal of Aircraft*, vol. 21, no. 9, pp. 733–736, 1984.

[8] Barmby, G., Cunningham, H., and Garrick, I., "Study of effects of sweep on the flutter of cantilever wings," Tech. Rep. Report 1014, NACA, 1950.

[9] Bauchau, O. A. and Kang, N. K., "A multibody formulation for helicopter structural dynamic analysis," *Journal of the American Helicopter Society*, vol. 38, pp. 3–14, April 1993.

[10] Bauchau, O., "Computational schemes for flexible, nonlinear multi-body systems," *Multibody System Dynamics*, vol. 2, pp. 169–225, 1998.

[11] Beck, M., "Die Knicklast des einseitig eingespannten, tangential gedrückten Stabes," *Journal of Applied Mathematics and Physics (ZAMP)*, vol. 3, no. 3, pp. 225 – 228, 1952.

[12] Bisplinghoff, R. L., Ashley, H., and Halfman, R. L., *Aeroelasticity*. Reading, Massachusetts: Addison-Wesley Publishing Co., 1955.

[13] Bolotin, V. V., "On vibrations and stability of bars under the action of non-conservative forces," in *Kolebaniia v turbomashinakh*, pp. 23 – 42, 1959.

[14] Bolotin, V. V., *Nonconservative Problems of the Theory of Elastic Stability*. New York: Pergamon Press, 1963.

[15] Bolotin, V. V., *Dynamic Stability of Elastic Systems*. San Francisco: Holden-Day, Inc, 1964.

[16] Bye, D. R. and McClure, P. D., "Design of a morphing vehicle," in *Proceedings of the 48th AIAA/ASME/ASCE/AHS/ASC Structures, Structural Dynamics and Materials Conference, Honolulu, Hawaii*, (Reston, Virginia), AIAA, April 23 – 26, 2007.

[17] Cadogan, D., Smith, T., Uhelsky, F., and MacKusick, M., "Morphing wing development for compact package unmanned aerial vehicles," in *Proceedings of the 45th AIAA/ASME/ASCE/AHS/ASC Structures, Structural Dynamics and Materials Conference, Palm Springs, California*, (Reston, Virginia), AIAA, April 19 – 23, 2004. AIAA Paper 2004-1807.

[18] Cesnik, C. E. S. and Hodges, D. H., "VABS: a new concept for composite rotor blade cross-sectional modeling," *Journal of the American Helicopter Society*, vol. 42, pp. 27 – 38, January 1997.

[19] Chang, C.-S., Hodges, D. H., and Patil, M. J., "Flight dynamics of highly flexible aircraft," *Journal of Aircraft*, vol. 45, pp. 538 – 545, Mar.-Apr. 2008.

[20] Chipman, R. R. F., Rimer, M., and Muniz, B., "Body-freedom flutter of a 1/2-scale forward swept-wing model, an experimental and analytical study," Tech. Rep. NAS1-17102, NASA Langley Research Center, 1984.

[21] Collar, A., "The first fifty years of aeroelasticity," *Aerospace*, vol. 5, pp. 12 – 20, February 1978.

[22] Como, M., "Lateral buckling of a cantilever subjected to a transverse follower force," *International Journal of Solids and Structures*, vol. 2, no. 3, pp. 515 – 523, 1966.

[23] Crane, D., *Dictionary of Aeronautical Terms*. Aviation Supplies and Academics, third edition ed., 1997.

[24] Dowell, E. H., Traybar, J., and Hodges, D. H., "An experimental-theoretical correlation study of non-linear bending and torsion deformations of a cantilever beam," *Journal of Sound and Vibration*, vol. 50, no. 4, pp. 533–544, 1977.

[25] Dowell, E., Edwards, J., and Strganac, T., "Nonlinear aeroelasticity," *Journal of Aircraft*, vol. 40, pp. 857–874, September-October 2003.

[26] Dunn, J., Horta, L., Ivanco, T., Piatak, D., Samareh, J., Scott, R., and Wieseman, C., "Nasa contributions to darpa mas program." Aerospace Flutter and Dynamics Council Meeting, NASA Langley Research Center, Hampton, VA, May 2004.

[27] Elishakoff, I. and Lottati, I., "Divergence and flutter of nonconservative systems with intermediate support," *Computer Methods in Applied Mechanics and Engineering*, vol. 66, pp. 241 – 250, 1988.

[28] Fazelzadeh, S., Mazidi, A., and Kalantari, H., "Bending-torsional flutter of wings with an attached mass subjected to a follower force," *Journal of Sound and Vibration*, vol. 323, no. 1-2, pp. 148 – 162, 2009.

[29] Feldt, W. T. and Herrmann, G., "Bending-torsional flutter of a cantilevered wing containing a tip mass and subjected to a transverse follower force," *Journal of the Franklin Institute*, vol. 297, no. 6, pp. 467 – 478, 1974.

[30] Flanagan, J. S., Strutzenberg, R. C., Myers, R. B., and Rodrian, J. E., "Development and flight testing of a morphing aircraft, the NextGen MFX-1," in *Proceedings of the 46th AIAA/ASME/ASCE/AHS/ASC Structures, Structural Dynamics and Materials Conference, Austin, Texas*, (Reston, Virginia), AIAA, April 18 – 21, 2007. AIAA Paper 2007-1707.

[31] Fung, Y. C., *An Introduction to the Theory of Aeroelasticity*. New York: Wiley, 1955.

[32] Fung, Y. C., *An Introduction to the Theory of Aeroelasticity*. New York, USA: Dover, 1st ed., 1993.

[33] Gamboa, P., Vale, J., Lau, F., and Suleman, A., "Optimization of a morphing wing based on coupled aerodynamic and structural constraints," *AIAA Journal*, vol. 47, September 2009.

[34] Gandhi, N., Jha, A., Monaco, J., Seigler, T. M., Ward, D., and Inman, D. J., "Intelligent control of a morphing aircraft," in *Proceedings of the 46th AIAA/ASME/ASCE/AHS/ASC Structures, Structural Dynamics and Materials Conference, Austin, Texas*, (Reston, Virginia), AIAA, April 18 – 21, 2007.

[35] Goland, M., "The flutter of a uniform cantilever wing," *Journal of Applied Mechanics*, vol. 12, pp. A197 – A208, December 1945.

[36] Goland, M. and Luke, Y. L., "The flutter of a uniform wing with tip weights," *Journal of Applied Mechanics*, vol. 15, no. 1, pp. 13–20, 1948.

[37] Gomez, J. C. and Garcia, E., "Morphing unmanned aerial vehicles," *Smart Materials and Structures*, vol. 20, September 2011.

[38] Gyorgy-Falvy, D., "Performance analysis of the "Horten IV" flying wing," in *Presented at the 8th O.S.T.I.V. Congress, Cologne, Germany*, June 1960.

[39] Hodges, D. H., "Geometrically-exact, intrinsic theory for dynamics of curved and twisted anisotropic beams," *AIAA Journal*, vol. 41, pp. 1131 – 1137, June 2003.

[40] Hodges, D. H., *Nonlinear Composite Beam Theory*. Reston, Virginia: AIAA, 2006.

[41] Hodges, D. H., Patil, M. J., and Chae, S., "Effect of thrust on bending-torsion flutter of wings," *Journal of Aircraft*, vol. 39, pp. 371 – 376, Mar.-Apr. 2002.

[42] Hodges, D. H. and Pierce, G. A., *Introduction to Structural Dynamics and Aeroelasticity*. Cambridge, U.K.: Cambridge University Press, 1st ed., 2002.

[43] Hodges, D. H. and Pierce, G. A., *Introduction to Structural Dynamics and Aeroelasticity*. Cambridge, U.K.: Cambridge University Press, 2nd ed., 2011.

[44] Ivanco, T. G., Scott, R. C., Love, M. H., and Zink, P. S., "Validation of the lockheed martin morphing concept with wind tunnel testing," in *Proceedings of the 48th AIAA/ASME/ASCE/AHS/ASC Structures, Structural Dynamics and Materials Conference, Honolulu, Hawaii*, (Reston, Virginia), AIAA, April 23 – 26, 2007.

[45] Karpouzian, G. and Librescu, L., "Exact flutter solution of advanced anisotropic composite cantilevered wing structure," in *Proceedings of the 34th Structures, Structural Dynamics, and Materials Conference, La Jolla, California*, pp. 1961 – 1966, April 19 – 22, 1993. AIAA-93-1535-CP.

[46] Karpouzian, G. and Librescu, L., "Nonclassical effects on divergence and flutter of anisotropic swept aircraft wings," *AIAA Journal*, vol. 34, no. 4, pp. 786 – 794, 1996.

[47] Lee, D. H. and Weisshaar, T. A., "Aeroelastic studies on a folding wing configuration," in *Proceedings of the 46th AIAA/ASME/ASCE/AHS/ASC Structures, Structural Dynamics and Materials Conference, Austin, Texas*, (Reston, Virginia), AIAA, April 18 – 21, 2005.

[48] Librescu, L., Na, S., Marzocca, P., Chung, C., and Kwak, M., "Active aeroelastic control of 2-d wing-flap systems operating in an incompressible flow-field and impacted by a blast pulse," *Journal of Sound and Vibration*, vol. 283, pp. 685 – 706, 2005.

[49] Librescu, L., Na, S., Qin, Z., and Lee, B., "Active aeroelastic control of aircraft composite wings impacted by explosive blasts," *Journal of Sound and Vibration*, vol. 318, pp. 74 – 92, 2008.

[50] Lottati, I., "Flutter and divergence aeroelastic characteristics for composite forward swept cantilevered wing," *Journal of Aircraft*, vol. 22, pp. 1001 – 1007, Nov. 1985.

[51] Love, M. H., Wieselmann, P., and Youngren, H., "Body freedom flutter of high aspect ratio flying wings," in *Proceedings of the 46th AIAA/ASME/ASCE/AHS/ASC Structures, Structural Dynamics and Materials Conference, Austin, Texas*, (Reston, Virginia), AIAA, April 18 – 21, 2005.

[52] Mardanpour, P., Hodges, D., Neuhart, R., and Graybeal, N., "Effect of engine placement on aeroelastic trim and stability of flying wing aircraft," *Journal of Aircraft*, 2013. doi: http://dx.doi.org/10.2514/1.C031955.

[53] Marzocca, P., Librescu, L., and Chiocchia, G., "Aeroelastic response of 2-d lifting surfaces to gust and arbitrary explosive loading signatures," *International Journal of Impact Engineering*, vol. 25, pp. 41 – 65, 2001.

[54] Marzocca, P., Librescu, L., and Chiocchia, G., "Aeroelastic response of a 2-d airfoil in a compressible flow field and exposed to blast loading," *Journal of Aerospace Science and Technology*, vol. 6, pp. 259 – 272, 2002.

[55] Molyneux, W. G., "The flutter of swept and unswept wings with fixed-root condition," Tech. Rep. R. & M. No. 2796, Aeronautical Research Council Reports and Memoranda, 1955.

[56] Molyneux, W. G. and Hall, H., "The aerodynamic effects of aspect ratio and sweepback on wing flutter," Tech. Rep. R. & M. No. 3011, Aeronautical Research Council Reports and Memoranda, 1957.

[57] Moore, M., "NASA puffin electric tailsitter VTOL concept," in *10th AIAA Aviation Technology, Integration, and Operations (ATIO) Conference*, September 2010.

[58] Moseley, William C., J. and Gainer, T. G., "Effect of wing thickness and sweep on the oscillating hinge-moment and flutter characteristics of a flap-type control at transonic speeds," Tech. Rep. NASA-TR-R-7, NASA, 1959.

[59] Myhra, D., *The Horten Brothers and Their All-Wing Aircraft*. Schiffer Military/Aviation History, Schiffer Publications, Pennsylvania, September 1998.

[60] Na, S. and Librescu, L., "Dynamic response of adaptive cantilevers carrying external stores and subjected to blast loading," *Journal of Sound and Vibration*, vol. 231, pp. 1039 – 1055, 2000.

[61] Na, S., Song, J., Choo, J., and Qin, Z., "Dynamic aeroelastic response and active control of composite thin-walled beam structures in compressible flow," *Journal of Sound and Vibration*, vol. 330, pp. 4998 – 5013, 2011.

[62] Nayfeh, A. H. and Mook, D. T., *Nonlinear Oscillations*. New York: John Wiley and Sons, 1979.

[63] Patil, M. J. and Hodges, D. H., "On the importance of aerodynamic and structural geometrical nonlinearities in aeroelastic behavior of high-aspect-ratio wings," *Journal of Fluids and Structures*, vol. 19, pp. 905 – 915, Aug. 2004.

[64] Patil, M. J. and Hodges, D. H., "Flight dynamics of highly flexible flying wings," *Journal of Aircraft*, vol. 43, no. 6, pp. 1790–1799, 2006.

[65] Patil, M. J., Hodges, D. H., and Cesnik, C. E. S., "Limit cycle oscillations in high-aspect-ratio wings," *Journal of Fluids and Structures*, vol. 15, pp. 107 – 132, Jan. 2001.

[66] Patil, M. J., Hodges, D. H., and Cesnik, C. E. S., "Nonlinear aeroelasticity and flight dynamics of high-altitude, long-endurance aircraft," *Journal of Aircraft*, vol. 38, pp. 88 – 94, Jan.-Feb. 2001.

[67] Peters, D. A., Karunamoorthy, S., and Cao, W.-M., "Finite state induced flow models; part I: two-dimensional thin airfoil," *Journal of Aircraft*, vol. 32, pp. 313 – 322, Mar.-Apr. 1995.

[68] Saberi, H. A., Khoshlahjeh, M., Ormiston, R. A., and Rutkowski, M. J., "RCAS overview and application to advanced rotorcraft problems," in *4th Decennial Specialists' Conference on Aeromechanics, San Francisco, California, January 21–23*, American Helicopter Society, 2004.

[69] Schweiger, J., Sensburg, O., and Berns, H., "Aeroelastic problems and structural design of a tailless CFC-sailplane," in *Proceedings of the 2nd International Forum on Aeroelasticity and Structural Dynamics, Aachen, West Germany*, 1985.

[70] Simitses, G. J. and Hodges, D. H., *Fundamentals of Structural Stability*. Boston: Elsevier, 2006.

[71] Simpson, A., Coulombe, N., Jacob, J., and Smith, S., "Morphing wing development for compact package unmanned aerial vehicles," in *Proceedings of the 46th AIAA/ASME/ASCE/AHS/ASC Structures, Structural Dynamics and Materials Conference, Austin, Texas*, (Reston, Virginia), AIAA, April 18 – 21, 2005.

[72] Snyder, M. P., Sanders, B., Estep, F. E., and Frank, G. J., "Vibration and flutter characteristics of a folding wing," in *Proceedings of the 46th AIAA/ASME/ASCE/AHS/ASC Structures, Structural Dynamics and Materials Conference, Austin, Texas*, (Reston, Virginia), AIAA, April 18 – 21, 2005.

[73] Sotoudeh, Z., Hodges, D. H., and Chang, C. S., "Validation studies for aeroelastic trim and stability analysis of highly flexible aircraft," *Journal of Aircraft*, vol. 47, no. 4, pp. 1240 – 1247, 2010.

[74] Stenfelt, G. and Ringertz, U., "Lateral stability and control of a tailless aircraft configuration," *Journal of Aircraft*, vol. 46, pp. 2161 – 2164, November-December 2009.

[75] Stubbs, M. T., "Morphing wing development for compact package unmanned aerial vehicles," Master's thesis, Virginia Polytechnic Institute and State University, December 2003.

[76] Thomas, F. and Milgram, J., *Fundamentals of Sailplane Design*. College Park Press, 1999.

[77] Timoshenko, S. P. and Gere, J. M., *Theory of Elastic Stability*. New York: McGraw-Hill Book Company, 2nd ed., 1961.

[78] Weisshaar, T., "Morphing aircraft technology – new shapes for aircraft design," in *Meeting Proceedings RTO-MP-AVT-141*, (Neuilly-sur-Seine, France), RTO, April 18 – 21, 2006.

[79] Wilson, J., "Morphing UAVs change the shape of warfare," *Aerospace America*, vol. 42, pp. 28 – 29, February 2004.

[80] Wlezien, R., Horner, G., McGowan, A., Padula, S., Scott, M., Silcox, R., and Simpson, J., "The aircraft morphing program," in *44th AIAA/ASME/ASCE/AHS/ASC Structures, Structural Dynamics and Materials Conference, Norfolk, Virginia*, (Reston, Virginia), AIAA, April 19 – 22, 1998.

[81] Wohlhart, K., "Dynamische Kippstabilität eines Plattenstreifens unter Folgelast," *Zeitschrift für Flugwissenschaften*, vol. 19, no. 7, pp. 291 – 298, 1971.

[82] Wooldridge, E., "Early flying wings," Tech. Rep. `http://www.century-of-flight.net`, 2012.

[83] Young, T. and Juan, C., "Dynamic stability and response of fluttered beams subjected to random follower forces," *International Journal of Nonlinear Mechanics*, vol. 38, pp. 889 – 901, 2003.

[84] Yu, W., Hodges, D. H., and Ho, J. C., "Variational asymptotic beam sectional analysis – an updated version," *International Journal of Engineering Science*, vol. 59, pp. 40 – 64, October 2012.

[85] Yu, W., Hodges, D. H., Volovoi, V. V., and Cesnik, C. E. S., "On Timoshenko-like modeling of initially curved and twisted composite beams," *International Journal of Solids and Structures*, vol. 39, no. 19, pp. 5101 – 5121, 2002.

VITA

Pezhman Mardanpour received his M.Sc. in Aerodynamics from School of Aerospace Engineering at Sharif University of Technology, Tehran, Iran in 2006. He joined the German Aerospace Center (DLR - Göttingen), Institute of Aeroelasticity and performed experimental aeroelastic research. He received another MS from Guggenheim School of Aerospace Engineering at Georgia Institute of Technology in the field of Aeroelasticity and Structural Dynamics in 2012. In August of 2013, he received his Doctorate of Philosophy in Aerospace Engineering from Guggenheim School of Aerospace Engineering at Georgia Institute of Technology.